Quantum Interference Through Plasmonic Nanostructures

By

Alexander Büse

A thesis submitted to Macquarie University
for the degree of Doctor of Philosophy
Department of Physics and Astronomy
December 2016

Typeset in LaTeX 2ε.

Except where acknowledged in the customary manner, the material presented in this thesis is, to the best of my knowledge, original and has not been submitted in whole or part for a degree in any university.

Alexander Büse

Acknowledgments

First and foremost I would like to thank my supervisor Gabriel Molina-Terriza for his continuous support. His deep knowledge, excellent intuition and unwavering enthusiasm made working in his group a great pleasure that I will always remember. I am very grateful that he always encouraged me to follow my own ideas. I would also like to thank my co-supervisor Mathieu Juan for his help throughout the last years. Whenever I needed his advice, he was more than happy to help. Furthermore, I would like to thank Nora Tischler for the good time we had building the source and the excellent collaboration afterwards. Although I mention the project only on a side note in this thesis, I am very grateful to Ivan Fernandez-Corbaton for giving me the opportunity to contribute to his interesting work on gravitational waves. I am thankful for the valuable hint from Thomas Volz about the re-emission of photons from avalanche photo diodes. This cleared up a substantial headache. Though they were not directly involved in my project, I would like to thank my friends Hossein Dinani, Andrea Tabacchini, Xavier Zambrana-Puyalto and Xavier Vidal. It was a great pleasure and a lot of fun sharing lab and office with them. Additionally, I would like to thank Alexei Gilchrist for providing a solid LaTeX template, Lisa Pesavento and Lisa Chanell for always warmly welcoming me into their office and supporting me in administrative problems and finally Mauro Cirio for entrusting me with his legacy, the coffee selling business. I am afraid that under my responsibility the business declined steadily and hope that a true coffee lover can revive it.

I would like to thank my whole family Rolf, Bettina, Andreas and Iris for their support, their commitment to not let distance threaten our bond and their willingness to travel afar to visit us down-under. My dad deserves a special mention in that he read the whole thesis with a very watchful eye and repeatedly asked excellent questions. Last but certainly not least, I am deeply grateful for the loving support of my fiancé Anja, her patience and understanding for unusual working hours and our shared excitement over the adventure of discovering Australia.

List of Publications

[AB15] A. Büse, N. Tischler, M. L. Juan and G. Molina-Terriza (2015): Where are photons created in parametric down-conversion? On the control of the spatio-temporal properties of biphoton states. *Journal of Optics* **17** (6), p. 065201

[IFC15] I. Fernandez-Corbaton, M. Cirio, A. Büse, L. Lamata, E. Solano and G. Molina-Terriza (2015): Quantum Emulation of Gravitational Waves. *Scientific Reports* **5**, pp. 11538

[NT15] N. Tischler, A. Büse, L. G. Helt, M. L. Juan, N. Piro, J. Ghosh, M. J. Steel and G. Molina-Terriza (2015): Measurement and Shaping of Biphoton Spectral Wave Functions. *Phys. Rev. Lett.* **115** (19), p. 193602

[AB16] A. Büse, M. L. Juan, N. Tischler, F. Sciarrino, L. Marrucci and G. Molina-Terriza (2016): Quantum control of photonic entanglement with a single sub-wavelength structure *in preparation*

Contributions

Advances in research are often the result of a team effort and this has been no different for the results presented in this thesis. In the following, I will detail the contributions to the three central chapters.

Chapter 3
The results presented in chapter 3 have mostly been published in [AB15]. I discovered the effect of the delay due to the crystal displacement. I designed and performed the experiment and analysed the data. In addition to the measurement based on the Hong-Ou-Mandel interference, I developed the idea to measure the time delay directly and I subsequently implemented it. Nora Tischler helped me setting up the SPDC source. She also developed the analytical calculations and performed the numerical calculations to compare to the experimental results. The whole project was guided by Dr. Mathieu Juan and Prof. Gabriel Molina-Terriza.

Chapter 4
The results presented in chapter 4 have mostly been published in [NT15]. I experimentally implemented the reconstruction scheme and conducted the measurements. Additionally, I designed and implemented the stabilisation and normalisation measures to achieve the necessary data quality. The idea for the reconstruction scheme was devised by Nora Tischler and theoretically implemented by her, Dr. Luke Helt and Prof. Gabriel Molina-Terriza. Nora Tischler also wrote and conducted simulations of the SPDC wavefunction to compare against the experimental results. The q-plate for the measurements with a Laguerre-Gaussian detection mode has been supplied by our collaborators Prof. Lorenzo Marrucci and Prof. Fabio Sciarrino. The whole project was guided by Dr. Mathieu Juan and Prof. Gabriel Molina-Terriza.

Chapter 5
A manuscript reporting the work presented in chapter 5 is currently in preparation [AB16]. Prof. Gabriel Molina-Terriza had the vision to combine nano-photonics and quantum optics and make two photons interfere through a plasmonic nanoaperture. I further developed the idea and found the exact form of the quantum interference. In regular discussion with Prof. Gabriel Molina-Terriza, I then designed the experiment and implemented it. I performed the measurements and the subsequent data analysis. I also developed a scheme to accurately measure coincidences from four channels, using only two time-to-amplitude converter modules (see appendix A). The sample containing the plasmonic nanoapertures was fabricated by Nora Tischler and Michael Larkins. The q-plates necessary for the measurements have been

supplied by our collaborators Prof. Lorenzo Marrucci and Prof. Fabio Sciarrino. Again, the whole project was guided by Dr. Mathieu Juan and Prof. Gabriel Molina-Terriza.

In addition to the work presented in the main three chapters, I was tangentially involved in work by Dr. Ivan Fernandez-Corbaton on the quantum emulation of gravitational waves [IFC15]. I contributed to the proposed experimental realisation of the specific two-photon state. I briefly touch on this in section 2.4.

Abstract

Quantum technologies like quantum computing, quantum communication or quantum metrology promise astonishing advantages over their classical counterparts. However, they all require excellent control and protection of the involved quantum states. In this respect, photons are ideal carriers of quantum information due to their robustness against decoherence and the ease with which they can be transferred over long distances. At the same time they suffer from weak interactions with matter and the large structures necessary, as given by the wavelength of light. Combining quantum optics with plasmonic structures could open an avenue to address these drawbacks while still benefiting from the advantages of photons.

We present for the first time the transmission of an entangled two-photon state through a plasmonic aperture that is smaller than the wavelength of the light. Entanglement is the key resource for many quantum information schemes and its protection of great interest. Strong interactions with the nanoaperture usually destroy the entanglement of an arbitrary state. We tailor a special state for the interaction – taking into account the specific properties of the aperture – that leads to quantum interference and eventually protects the entanglement from degradation. We experimentally demonstrate creation of this state, transmission through the nanoaperture and successful protection of the entanglement.

On our way to this achievement, we improve our control over the spontaneous parametric down-conversion source of photon pairs. We report a surprising dependence of the time delay distribution between the photons of the pair on the position of the non-linear crystal. We experimentally confirm the effect via quantum interference experiments and challenging direct measurements of the arrival time. Furthermore, a novel reconstruction scheme for the complex spectral biphoton wave function allows us to study the temporal correlations in more detail and to shape the wave function. We experimentally demonstrate the reconstruction in different situations and find an unexpected temporal distribution with a detection mode carrying orbital angular momentum.

Contents

The "paradox" is only a conflict between reality and your feeling of what reality "ought to be".

Richard Feynman [1]

1 General Introduction

This first chapter introduces the goal of the thesis and some of its fundamental concepts in terms understandable by any interested reader in order to give a general context. A more technical and detailed introduction follows in the next chapter 2.

We start in section 1.1 with the question of what quantum physics is and how it is different from classical physics. We answer very selectively with a few examples that will matter for this work, especially light sources and entanglement. In section 1.2 we see how the unique behaviour of quantum objects can be used in exciting applications that might transform every day life. We conclude the chapter with section 1.3 by giving an overview over our work and by exploring how it could help advance quantum technologies.

1.1 Quantum physics

Quantum physics was developed at the beginning of the 20th century as the result of searching for new explanations and descriptions of phenomena that could not be explained satisfactorily by theories at that time. A central role was played by electromagnetic radiation and its understanding. During the 19th century the idea that electromagnetic radiation – including visible light, ultraviolet, infrared – was a wave had solidified. Among other milestones the double slit experiment of Young (1803), where light interferes like typical waves and Maxwell's equations (1861) describing electromagnetic radiation as waves were responsible for this [1]. One unexplained problem was the emission spectrum of a so called black body (a body that absorbs all incident light), for which classical theory predicts an ever increasing energy emission towards higher frequencies. This results in a physically impossible infinite energy. In 1900, Planck published a new formula for the black body radiation that avoided the infinite energy. It was based on the idea that electromagnetic radiation is quantised in energy steps of

$$E = h\nu \quad , \tag{1.1}$$

where ν is the frequency of the radiation and h is a constant, now known as Planck's constant. This discovery, that light appears in quantised energy packets challenged the prevailing picture of light as a wave. The explanation of the photoelectric effect by Einstein in 1905 further threatened the wave concept. This effect, where electrons are ejected from a metal by incoming light, could also be elegantly explained by assuming that light exists in quanta. All this would eventually lead to the so called wave-particle duality, one of the fundamental features of quantum physics. Einstein and Infeld wrote in 1938 [2]:

> But what is light really? Is it a wave or a shower of photons? [...] There seems no likelihood of forming a consistent description of the phenomena of light by a choice of only one of the two possible languages. It seems as though we must use sometimes the one theory and sometimes the other, while at times we may use either. We are faced with a new kind of difficulty. We have two contradictory pictures of reality; separately neither of them fully explains the phenomena of light, but together they do!

This coexistence of the two views of light and their selective use for different phenomena, can be understood by considering a fundamental entity of quantum physics – the wave function. The wave function represents the complete knowledge about a particle or system. A particle – for example an electron or a photon – usually has several degrees of freedom, but we will consider only space for the moment (disregarding relativistic problems for simplicity). The wave function can then be thought of as assigning every point in space a probability amplitude that the particle can be found at that point. Contrary to classical physics, the position is then no longer a precise quantity, but inherently statistical in nature. The particle's wave function describes where it is likely to be found and where it is less likely, but there is no specific point in space where it definitely can be found at a certain point in time. The wave function evolves with time and behaves – as the name suggests – like a wave. This is the underlying reason that particles in quantum mechanics behave as waves, in particular they can be thought of as the wave of the probability amplitude. The particle behaviour manifests itself, once the particle is detected. For example when measured in space, the uncertainty in the location vanishes and the particle is found at exactly that location. The way wave functions behave and evolve was formalised by Schrödinger in 1925.

One other striking feature of quantum mechanics was first discussed by Einstein, Podolsky and Rosen in an attempt to show that quantum mechanics is incomplete [3]. What they considered an argument against the completeness of the theory was later acknowledged as one of the defining features of quantum mechanics. The ability for two or more particles to form a connected system – with one collective wave function – that behaves in a way which can not be explained by treating the particles individually.

1.1.1 Light sources - classical and quantum

We now want to discuss different types of light sources, since a special source of quantum light is used for the experiments described in this thesis. For the purpose of our comparison of different light sources, the characterising features are coherence and counting statistics. Coherence describes whether different parts (either in space or time) of a wave can interfere with each other. If the phase relation between these parts is constant, interference is possible and the wave is said to be coherent. The counting statistics provide information about the expected distribution of detection events when measuring the arrival of single photons. Assuming that a detector is placed somewhere in the vicinity of the light source and the detector is capable of registering the arrival of single photons, the question arises, what is the signal going to look like? We discuss these two important characteristics of light sources for three different types.

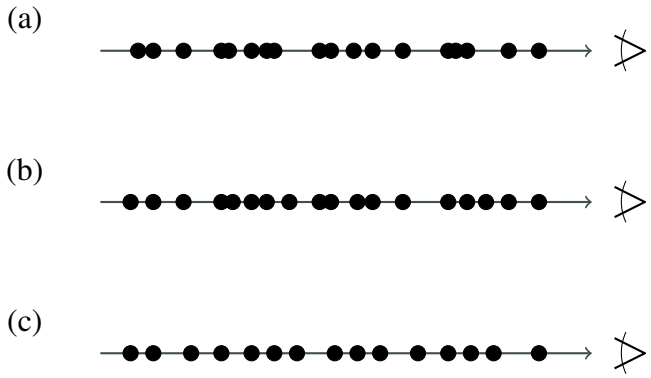

Figure 1.1: Schematic comparison between the three regimes of photon statistics. A stream of photons is measured at a detector on the right and the spacing between photons can be very different for the three regimes: (a) Super-Poissonian statistics, where random changes in intensity lead to stronger fluctuations than those found in (b) Poissonian statistics, where the arrival of a single photon is independent from the arrival of any other photon. (c) Sub-Poissonian statistics, where photons are well separated and fluctuations are even smaller.

The first source of light is truly ubiquitous. It is thermal radiation, such as from an incandescent light bulb or any other "warm" body. The motion of charged particles inside any material causes electromagnetic radiation to be emitted and the higher the temperature, the higher the speed of the particles and with that the higher the energy of the emitted radiation. At room temperature most of the light is emitted as infrared, which is why we do not see our surroundings glow in the visible spectrum. Independent waves with different frequencies are emitted from different parts of the body, making the emission highly incoherent. Waves emitted independently of each other have arbitrary and changing phase relationships, making it impossible to observe interference. Regarding the counting statistics, thermal light tends to

bunch together, due to fluctuations of the emission. This regime is called Super-Poissonian statistics. Figure 1.1 (a) shows schematically such a stream of photons.

Another important source of light is the laser. Within an active medium, photons are bounced back and forth, leading to stimulated emission of further photons with the same properties. In contrast to thermal radiation, the atoms emit in phase, "knowing" of each other, because of the common reference due to the light field itself. This gives rise to high coherence. The photon statistics are Poissonian, meaning that the probability for the arrival of a photon is independent of any other. Figure 1.1 (b) visualises such a stream of photons. There is less bunching compared to the super-Poissonian case of (a).

A source that shows true quantum features is depicted in figure 1.1 (c). Here, photons never arrive close to one another, they are perfectly anti-bunched. An experimental realisation of such a source is a single photon emitter and has approximately been demonstrated in a variety of systems. A true single photon source would be an invaluable tool for many quantum technologies (see section 1.2) and is hence an area of intense research. The coherence of a single photon source depends strongly on its specific implementation.

The photon source we use throughout this thesis is special in the sense that it produces well separated pairs instead of single photons. A stream of many high energy photons is sent through a non-linear crystal, where a small chance exists that a single high energy photon is transformed into two lower energy photons. Due to the low probability of this happening, pairs are well separated from each other and it is unlikely to get more than one pair at a time. These photon pairs are used for a variety of applications. We discuss these so called spontaneous parametric down-conversion (SPDC) sources in section 2.2 of the next chapter in more detail.

1.1.2 Entanglement

We now want to focus on one quintessential feature of quantum mechanics: entanglement. Entanglement plays a central role throughout this thesis and is an important resource for many quantum technologies. In 1935 Schrödinger put it this way [4]:

> I would not call that *one* but rather *the* characteristic trait of quantum mechanics, the one that enforces its entire departure from classical lines of thought.

Two or more particles can become entangled when interacting with each other and through this interaction they can not be described independently any longer, but must be treated as one system. Even if the particles were to be separated by large distances, they would still form this unit and strangely influence each other. What is meant by influence in this context? Following the argumentation of Gisin [5] we first take a look at classical correlation and then argue that entanglement gives rise to a completely new type of correlation.

A correlation is a synchronised behaviour of two quantities or events A and B. This could for example be the flow rate of municipal fresh water that suddenly jumps up when there is a break in a major sports event. Science very often deals with such situations, where a correlation is observed and a causal relation is wanted to explain the observation. The correlation between the fresh water consumption and the course of the sports event is most likely explained by an increased bathroom usage throughout the city, when the exciting game is paused. In this case we say that the game influences and causes the behaviour of the water consumption. So A causing B or B causing A is a first type of causal relation. Another one is the so called common cause: A and B could be caused by C.

It is important to note here that A causes B makes sense only if A even had the chance to cause B. That means if, for example, B lies in the past of A, A causes B is not a valid explanation for an observed correlation between A and B. To be more precise, we have to take space into account as well. If A is too far away to reach B in time, A can not cause B. "Too far away" is accurately defined by the speed of light. No information can be transmitted faster than the speed of light. So, in order for A to cause B, they have to be separated in space-time by at most the distance of a light signal connecting A with B. In this sense, we speak of local correlations if they can be explained by causal relations, where the effect was transported with at most the speed of light.

Quantum mechanics, as first discussed by Einstein, Podolsky and Rosen [3] allows for non-local correlations. Non-local [6] means that there is no local causal relation possible. Einstein, Podolsky and Rosen used this discovery as an argument against the completeness of quantum mechanics in the sense that they expected a more fundamental explanation of quantum mechanics could be found to resolve this non-locality. For these non-local correlations to manifest, entanglement is necessary. A very simple example of an entangled system would be two photons which have had a specific interaction at some point in time, forming their special bond. After that, it does not matter how far they are separated, as long as they are undisturbed, the entanglement will persist. Measuring one of the two, forcing it to decide on a measurement result (collapsing the wave function), instantaneously [7] determines the outcome of a measurement of the second photon. If those measurements were always of the same type, such a behaviour could be explained with a classical correlation. The classically inexplicable happens when the photons are measured in different basis, leading to a type of correlation stronger than any classical correlation. Einstein called this "spooky actions at a distance" (page 158 in [8]). Interestingly, those correlations were used by Bell in 1964 [9] to formulate inequalities that rule out the possibility of a more fundamental explanation of quantum mechanics. One that both reproduces the results of quantum mechanics and restores locality, as envisioned by Einstein. These inequalities have since been tested countless times with different systems and improving accuracies and always found that quantum mechanics and entanglement can not be explained by a local hidden variable theory [10–14].

1.2 Quantum technologies

Quantum mechanics is the ultimate description of nature. In particular, microscopic objects (atoms, ions, electrons) can only be described with quantum mechanics. Since all matter is made of atoms, it is difficult to draw a line between conventional technologies and quantum technologies. However, one can roughly distinguish between two phases of technological advances based on concepts from quantum mechanics.

The first phase built upon the ideas of quantised energies and the wave function and generated such now ubiquitous technologies as the laser (1960) or semiconductor transistors (1947). The transistor makes explicit use of the fact that electrons can tunnel through a forbidden region, because their wave function extends past this region. The laser on the other hand would not be possible without the quantised energy of light and the stimulated emission. Only many years later did the second phase take off, starting with ideas around information and entanglement.

A very prominent example of quantum information research is directed towards quantum computation. Some tasks that are hard to perform on a classical computer, like for example factoring a large number, can be done with a much more favourable scaling on a quantum

computer [15]. Significant efforts are undertaken to research and prepare the building blocks of a quantum computer and many different approaches in a variety of different systems are explored. The main hindrance towards a working quantum computer are negative influences of the environment on the delicate carriers of information. Nowadays a few of these so called qubits can be controlled, but for a useful universal quantum computer thousands to millions of qubits would be needed [16, 17]. As an intermediate goal quantum simulations emerge as an exciting testbed for early quantum computers. Quantum simulations could efficiently solve important problems in chemistry, since many of these problems depend on the quantum mechanical behaviour of electrons.

A somewhat related topic is that of quantum cryptography [18, 19]. If a reasonably powerful quantum computer would exist, current state of the art cryptography relying predominantly on public key encryption schemes, would be worthless due to the ability of a quantum computer to factor large numbers efficiently. Luckily, quantum cryptography provides a way to make communications inherently secure by using entanglement.

Quantum metrology [20, 21] as a last example of a novel technology made possible by quantum mechanical effects, is also very promising. Measurements are fundamental to science and making them as precise as possible is an ongoing effort in every area. Due to inherent and unavoidable noise, there is a fundamental limit to the precision of classical measurements. It can be overcome by using special quantum states [22]. A prominent example where this may be of importance is the detection of gravitational waves by kilometre long interferometers. The recent first ever direct measurement of gravitational waves by the two LIGO interferometers [23] was performed without quantum effects. However, further increases in sensitivity could be driven by quantum metrology. A first interferometer, GEO 600, already makes use of this [24].

1.2.1 Nanophotonics and quantum optics

Our work is situated at the interface of nanophotonics and quantum optics. Before we introduce the aim of our work in the next section, we briefly discuss what the two fields can offer to one another.

Nanophotonics studies the behaviour of classical light at the nano-scale and its interactions with matter at this scale. Because the wavelength of light is large (visible light: 400 nm to 800 nm) compared to objects a few nanometer in size, it is difficult to create strong interactions between the two. This is overcome by using metallic structures, that are capable of concentrating the electromagnetic field to very small volumes. Free electrons inside the metal resonate with the external field, like in an antenna.

Quantum optics on the other hand studies the quantum features of light and how well controlled quantum states of light interact with matter. A special emphasis lies on quantum information encoded in these states. Photons are ideal carriers of quantum information due to their robustness against influences of the environment. However, controlling and modifying the quantum information can be difficult because of these weak interactions with matter.

This is where quantum optics and nanophotonics can benefit from one another. Nanophotonics could provide the tools to process quantum information at the nano-scale. The ability to fabricate dedicated structures, optimised for specific tasks may open new possibilities. In the other direction, challenges in nano-photonics, like the sensing of single molecules could profit from the introduction of controlled quantum states of light.

1.3 Our work

The main goal of this thesis is to demonstrate the protection of an entangled quantum state of light from degradation due to the interaction with a metallic structure smaller than the wavelength of the light. We successfully engineer the state of a photon pair, considering the specific behaviour of the nano-structure and show that it is quantum interference between the two photons that protects the state. Both photons are created in a spontaneous parametric down-conversion source, which we briefly mentioned in section 1.1.1. Subsequently, we control their quantum state to ensure that they are entangled and let them interact with the structure. Interference only happens under very specific conditions in this system and we need very good control over the entangled state to achieve these conditions. We show that only the entanglement of the one specific state is protected and all other photon pairs lose their entanglement. The protection of entanglement is especially interesting for all experiments dealing with quantum information, as entanglement is an important resource. We describe the experiment and the theoretical foundations in chapter 5.

To reach the necessary control over the photon pair, we looked into effects on the time delay between both photons. This work is presented in chapter 3. The photons are created simultaneously from a decaying higher energy photon, but they propagate with different velocities through the medium, where the down-conversion takes place. Interestingly, the acquired time delay is incorporated in the wave function of the pair, leading to a true quantum uncertainty about the delay.

The other important step towards our goal is described in chapter 4, where we discuss and demonstrate a reconstruction scheme for the spectral wave function of the photon pair. The spectral wave function encompasses complete information about the energies and the relative time delay of the photon pair. The reconstruction protocol is based on careful measurements of interference between the two photons under varying relative temporal and spectral shifts with respect to each other.

We believe that this work constitutes a valuable contribution to current efforts understanding and exploiting quantum effects at the nano-scale. Many quantum technologies rely on entanglement as a basic resource and protecting it from interactions with the environment is crucial.

2

Technical Introduction

In this chapter we introduce general concepts that are relevant for the following chapters. We start in section 2.1 with a brief overview of the description of quantum states with wave functions and density matrices. In section 2.2 we introduce the photonic quantum state produced by spontaneous parametric down-conversion and the specific details of the source used for all our experiments. This is followed by section 2.3, where we introduce the famous Hong-Ou-Mandel interference. We continue in section 2.4 with a discussion of different photonic degrees of freedom with an emphasise on the angular momentum of light. We show how to control the orbital angular momentum with q-plates. We finally describe the action of a plasmonic nanoaperture on a beam of light in the section 2.6, where the angular momentum of light plays again an important role.

2.1 Quantum states

Measurements in quantum mechanics are inherently probabilistic in nature. The transmission of a horizontally polarised photon through a polariser that is neither horizontally nor vertically aligned can not be predicted with certainty. This uncertainty is not a mistake of the experimentalist, nor is it a lack of knowledge about the system. It reflects the nature of the wavefunction of the photon. With respect to the measurement basis, given by the polariser, the photon is in a superposition between the parallel and the orthogonal state and it is only due to the measurement that the wave function collapses onto one of the two possibilities. Knowing the photon is linearly polarised in a certain direction, we know everything there is to know about the photon with respect to its polarisation degree of freedom. Such a state, for which we have full knowledge is associated with a vector in Hilbert space and is called a pure state. For a specific choice of basis $\{|\psi_n\rangle\}$ it can be represented as a wave function

$$|\Psi\rangle = \sum_n c_n |\psi_n\rangle \quad , \tag{2.1}$$

where the coefficients c_n fulfill $\sum |c_n|^2 = 1$. The wave function attaches a probability amplitude to every possible measurement outcome of the degree of freedom under consideration. Any state that can be written as a coherent superposition of pure states, is itself a pure state.

In contrast to this intrinsic probability, there may also be a lack of knowledge, for example an uncertainty in the preparation of the state. This uncertainty can be incorporated into a density matrix, which name is reminiscent of phase space in classical statistical mechanics [25]. Such a system, where a classical probability is associated with more than one pure state, is called a mixed state. The density operator can describe any quantum state, mixed or pure and can abstractly be defined as:

$$\hat{\rho} = \sum_j p_j |\psi_j\rangle \langle\psi_j| \quad , \tag{2.2}$$

where p_j are the classical probabilities to find the pure states $|\psi_j\rangle$. These pure states are added incoherently in this case. Here, incoherently means that to calculate the probability of a certain measurement outcome, first the probability for every pure state is computed and then a weighted average is taken over all pure state results. If a specific orthonormal basis is chosen $\{|\phi_m\rangle\}$, the associated specific density matrix elements are obtained as:

$$\rho_{mn} = \langle\phi_m| \hat{\rho} |\phi_n\rangle \quad . \tag{2.3}$$

The dimension of the matrix is given by the number of basis vectors. With this density matrix it is straightforward to calculate the expectation value of an arbitrary operator $\hat{O}$

$$\left\langle \hat{O} \right\rangle = \mathrm{tr}(\rho \hat{O}) \quad . \tag{2.4}$$

Both mixed and pure states can conveniently be represented by density matrices. By choice of a suitable basis, the density matrix can always be diagonalised. If and only if the state is pure, there is exactly one eigenstate (and eigenvector) and thus only one element equal to 1 on the diagonal and all other matrix entries are zero. This relates back to the fact that any pure state can be described by exactly one Hilbert space vector. The condition for purity

of the state represented by a density matrix can concisely be written as

$$\mathrm{tr}(\rho^2) = 1 \quad . \tag{2.5}$$

For any mixed state $\mathrm{tr}(\rho^2) < 1$ holds. Apart from this, the density matrix has a few more important properties. In order for every ensemble average under the action of a hermitian operator to be real, the density matrix must be hermitian as well:

$$\rho_{mn} = \rho^*_{nm} \quad . \tag{2.6}$$

In simple words this means that the diagonal must be real and the off-diagonal elements are complex conjugates of each other. Since the probabilities of the incoherent mixture must add up to unity, it follows that

$$\mathrm{tr}(\rho) = 1 \quad . \tag{2.7}$$

Also, the density matrix is positive semidefinite, which requires all diagonal elements to be positive.

A system of more than one particle is entangled if it can not be described as a product state of its subsystems. For two particles with states in Hilbert spaces A and B,

$$|\psi\rangle_A \otimes |\phi\rangle_B \tag{2.8}$$

is a product state. If the two particles are entangled, their state can not be written in this way. A single entangled system as a whole may be a pure state, if however, the sub-systems are considered individually, they behave as completely mixed states [26]. Deciding whether a given system is entangled, is generally not trivial [27], but for the case of two particles with two dimensional Hilbert spaces, a number of entanglement measures exist [28].

We use the concurrence as a measure related to the entanglement of formation. It is defined for two qubits as [29, 30]

$$C(\rho) = \max\{0, \sqrt{\lambda_1} - \sqrt{\lambda_2} - \sqrt{\lambda_3} - \sqrt{\lambda_4}\} \quad , \tag{2.9}$$

where the λ_i are the ordered eigenvalues of the matrix $\rho(\sigma_y \otimes \sigma_y)\rho^*(\sigma_y \otimes \sigma_y)$, which is the product of the original and the single spin flipped density matrix. Here σ_y is a Pauli matrix. Additionally, we use the negativity as another entanglement monotone. In contrast to the concurrence it is related to the entanglement that could be harvested from a given state and defined as [30]

$$N(\rho) = \max\{0, -2\lambda_{\min}\} \quad , \tag{2.10}$$

where $\lambda_{\min}$ is the smallest eigenvalue of the partially transposed density matrix. Both concurrence and negativity take on values between 0 and 1, where 1 indicates a maximally entangled state and 0 indicates a not entangled state.

2.2 Photonic quantum states

We now introduce one of the most common sources of entangled photons, spontaneous parametric down-conversion (SPDC). In the presence of a quadratic non-linear medium, a high energy pump photon can spontaneously decay into two photons of lower energy. This is one of many processes observed in non-linear optics. Non-linear in this context means that the dielectric polarisation $P(t)$ of the medium in which the electromagnetic waves propagate,

responds non-linearly to the electric field. This can be expressed as a Taylor expansion in the electric field strength $E(t)$ [31]

$$P(t) \approx \chi^{(1)}E(t) + \chi^{(2)}E^2(t) + \chi^{(3)}E^3(t) + \ldots \quad , \tag{2.11}$$

where $\chi^{(n)}$ denotes the n-th susceptibility. For simplicity, we have written the equation in its scalar form. In general we would need to write polarisation and electric field as vectors and the susceptibilities as tensors. In many media, only $\chi^{(1)}$ is significant and the response is linear in the electric field strength. Even terms of the expansion occur only in media without inversion symmetry. Under inversion $E(t) \rightarrow -E(t)$ and $P(t) \rightarrow -P(t)$, which requires all even terms to be zero, if inverted and non-inverted equation 2.11 are to be equal. For SPDC, the second order non-linearity is important, which imposes restrictions on the type of material due to the required asymmetry under inversion. This excludes any disordered material from the start and even many crystals.

We will now give a brief motivation for the emergence of frequency related non-linear optical effects and eventually SPDC. We start from the wave equation

$$\nabla^2\mathbf{E} - \frac{n^2}{c^2}\frac{\partial^2\mathbf{E}}{\partial t^2} = \frac{4\pi}{c^2}\frac{\partial\mathbf{P}_{nonlin}}{\partial t^2} \quad , \tag{2.12}$$

where n is the index of refraction and c the speed of light in vacuum. P_{nonlin} is the part of the polarisation due to higher order terms. This means that in vacuum or a purely linear medium, the right side of this equation is zero. Assuming we have an incident field with two frequency components ω_1 and ω_2:

$$E(t) = E_1 e^{-i\omega_1 t} + E_2 e^{-i\omega_2 t} + \text{c.c.} \quad , \tag{2.13}$$

the second order polarisation in the medium is given by

$$\begin{aligned} P^{(2)}(t) = \chi^{(2)}E^2(t) = \chi^{(2)}\Big[&2E_1E_1^* + 2E_2E_2^* \\ &+E_1^2e^{-2i\omega_1 t} + E_2^2e^{-2i\omega_2 t} \\ &+2E_1E_2e^{-i(\omega_1+\omega_2)t} + \text{c.c.} \\ &+2E_1E_2^*e^{-2(\omega_1-\omega_2)t} + \text{c.c.}\Big] \quad . \end{aligned} \tag{2.14}$$

Several effects of non-linear optics are readily visible in this equation. The two terms of the first line correspond to a static electric field inside the crystal, since their second derivative (cf. equation 2.12) vanishes. The next line corresponds to second harmonic generation, where an incident wave is frequency doubled. This happens independently for both input waves. The third line corresponds to sum frequency generation, where a new photon of combined energy is generated by consuming two incident photons. The last line describes difference frequency generation, which is the process we are interested in, because it becomes SPDC in the limit of vanishing intensity of one of the two input beams. Usually, there is at most one of these four different effects observable. This is due to conservation of energy and momentum, which can not usually be fulfilled for all of these processes at the same time.

In difference frequency generation, the higher energetic photon of the two incident photons is destroyed, a new lower energy photon is created alongside a new photon at the difference frequency. The existence of the lower energy input photon stimulates this process. Even if this photon is not present in the input field, the process can still occur *spontaneously*: SPDC

[32, 33]. The decay of the high energy photon into two low energy photons – hence the *down-conversion* part of the name – is then induced by vacuum fluctuations. All of the non-linear processes named above are *parametric*, meaning that they leave the crystal unchanged. This requires that energy between input and output photons is conserved. The crystal only serves as a catalyst.

In SPDC, the high energy photon is typically called *pump* and the other two photons are called *signal* and *idler*. The names can be understood from the historical context, where down-conversion was often performed with non-degenerate photons where only one of them was in the visible range and easily detected, the signal, and the other one in the infrared and thus not easily detected, the idler [34].

The decay into two new photons happens only under specific conditions, called phase matching. Both energy and momentum have to be conserved in the process

$$\begin{aligned} \omega_p &= \omega_s + \omega_i \\ \mathbf{k}_p &= \mathbf{k}_s + \mathbf{k}_i \quad . \end{aligned} \tag{2.15}$$

Here the energy of each photons appears as the frequency ω and momentum as the vector $\mathbf{k}$. Each photon (pump, signal and idler) is identified by the index to each quantity. The conservation leads to correlations between frequency, momentum and polarisation of signal and idler photons. For example in the production of heralded single photons [35] this is often seen as a liability. If one of the two photons is detected, the other one is projected into a mixed state, which is often unfavourable for quantum information experiments, where pure states are required. As a countermeasure, the SPDC output has to be filtered strongly. On the other hand, these correlations are also exploited in various directions. We will discuss some examples in the section 2.4.

In a quantum mechanical framework, the state of the photon pair, the biphoton, after its creation can be calculated under the reasonable assumption of a classical pump field [36] and the final form is:

$$|\Psi\rangle = \int \mathrm{d}\mathbf{k}_s \, \mathrm{d}\mathbf{k}_i \, \mathrm{d}\sigma_s \, \mathrm{d}\sigma_i \;\; \Phi(\mathbf{k}_s, \mathbf{k}_i, \sigma_s, \sigma_i) \, a^\dagger(\mathbf{k}_s, \sigma_s) a^\dagger(\mathbf{k}_i, \sigma_i) \, |0\rangle \, |0\rangle \quad . \tag{2.16}$$

Here, $a^\dagger(\mathbf{k}_s, \sigma_s)$ and $a^\dagger(\mathbf{k}_i, \sigma_i)$ are the creation operators of signal and idler respectively. $\mathbf{k}$ is the momentum vector and σ the polarisation. The characteristics of the photon pair are hidden in the mode function $\Phi(\mathbf{k}_s, \mathbf{k}_i, \sigma_s, \sigma_i)$. It contains the correlations between signal and idler and is governed by the phase matching.

Experimentally, several different types of SPDC sources exist. The main classification characteristics are the relative polarisations of pump, signal and idler, the emission direction of signal and idler, and the type of non-linear crystal used. The relative linear polarisation gives rise to three categories: in type 0 down-conversion all three photons carry the same polarisation. If the pump photon is orthogonally polarised relative to the two down-converted photons, the source is of type I and the case of signal and idler photons being orthogonally polarised is assigned type II. All of these cases can be achieved with either different emission directions of the down-converted photons or with collinear emission. We use collinear type II down-conversion in the following experiments. Signal and idler being orthogonally polarised gives us a straightforward way of separating them with a polarising beam splitter. The advantage of using collinear production in the first place, lies in the ability to use rather long non-linear crystals, which increases the number of photon pairs produced. This is a somewhat recent development starting 2001 that only became possible with the introduction of

periodically poled crystals [37]. Historically, so called critical phase matching was achieved by tilting the optical axis of the crystal with respect to the pump beam. Introducing an additional periodicity into the crystal, by alternating the optical axis, allows for the so called quasi-phase matching [37–39]. With this technique the crystal can be fabricated to create phase matching for a specific type of down-conversion and specific wavelengths. Fine tuning of the phase matching is usually achieved by controlling the temperature of the crystal.

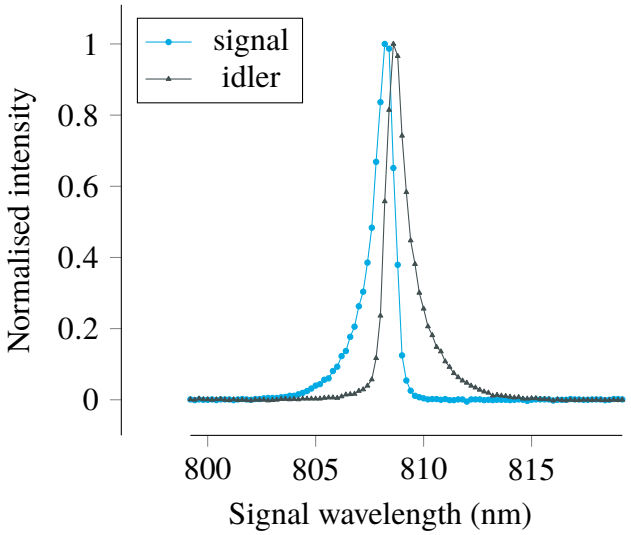

Figure 2.1: Normalised spectra of signal and idler coupled into single mode fibres.

We use a 15 mm long, periodically poled potassium titanyl phosphate (ppKTP) [40] crystal, with a poling period of 9.89 µm, which allows us to achieve type II, degenerate, collinear down-conversion with a pump wavelength of 404.25 nm at a crystal temperature of about 60 °C. Both signal and idler thus have a wavelength of 808.5 nm, when their wave-vector is parallel to the pump and slightly larger/smaller wavelengths at small angles. Figure 2.1 compares the measured spectra of signal and idler photons. The width of the down-converted spectra depends also on the pump bandwidth. In our case the pump is very narrow with a width of only 5 MHz.

Our source produces approximately 8×10^5 signal photons per second and mW of pump power inside the crystal, counted after coupling to single mode fibre. Although, SPDC relies on the non-linearity of the medium, it is linear in the pump intensity [32]. That means the number of photons produced scales linearly with the pump power and for our source the maximum power is 24 mW. This number of signal photons per second can not be translated directly to the number of pairs per second, because many of the pairs vanish due to losses of one photon of the pair at optical elements, especially at fibre couplings and inefficient photon counters. A typical ratio of intact pairs to single photons, lies at about 10 %. The decay probability for a single pump photon lies on the order of 10^{-12}.

2.3 Hong-Ou-Mandel interference

Interference is well known in classical physics, when two waves overlap. The classical picture can even be applied to single particle interference. The interference of two or more particles, however, is a purely quantum mechanical phenomenon and was first observed in the case of photons by Hong, Ou and Mandel [41] and reported in their seminal paper in 1987. It is now

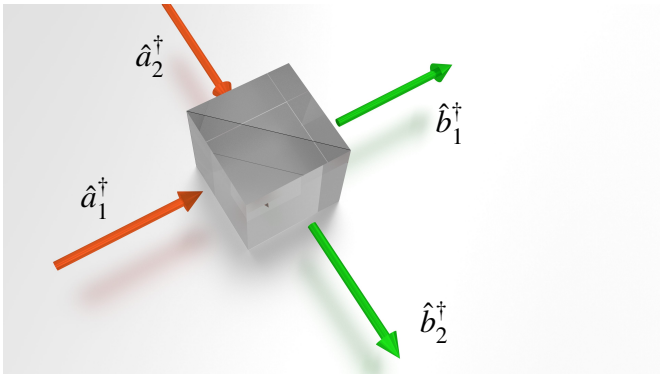

Figure 2.2: Schematic of the input and output ports of a non-polarising beam splitter, used for Hong-Ou-Mandel interference.

used for a wide variety of experiments and techniques in quantum information science. For example to entangle photons [42, 43], to teleport them [44] or in optical quantum gates [45].

A schematic of the Hong-Ou-Mandel interference is shown in figure 2.2. Sending a single photon into one of the two input ports of a non-polarising beam-splitter,

$$\hat{a}_1^\dagger \longrightarrow \frac{1}{\sqrt{2}}\left(\hat{b}_1^\dagger + \hat{b}_2^\dagger\right) \tag{2.17}$$

$$\hat{a}_2^\dagger \longrightarrow \frac{1}{\sqrt{2}}\left(\hat{b}_1^\dagger - \hat{b}_2^\dagger\right) \quad , \tag{2.18}$$

results in a superposition of the two output modes. Here, $\hat{a}^\dagger$ denotes a creation operator in an input port and $\hat{b}^\dagger$ the creation operator for a photon in the output mode. Having one photon in each of the two inputs together leads to behaviour that can not be explained classically

$$\hat{a}_1^\dagger \hat{a}_2^\dagger \longrightarrow \frac{1}{2}\left(\hat{b}_1^\dagger + \hat{b}_2^\dagger\right)\left(\hat{b}_1^\dagger - \hat{b}_2^\dagger\right) = \frac{1}{2}\left(\hat{b}_1^{\dagger 2} - \hat{b}_2^{\dagger 2}\right) \quad . \tag{2.19}$$

Namely, the two photons always leave the beam-splitter together. The cancellation of the mixed term is of course only possible, if the two photons are indistinguishable in all their remaining degrees of freedom, apart from the spatial mode they are in. Indistinguishability here means that it is impossible to identify the photons based on a measurement. In type II SPDC for example, signal and idler photon acquire different time delays while traveling through the non-linear crystal and they still interfere with each other, if the delay distribution is symmetric and the average delay is zero. The important point here is that the joint probability distribution of both photons in each degree of freedom must be symmetric. Distinguishable input photons would require the creation operators in the output to be different, preventing any interference.

Experimentally, Hong-Ou-Mandel interference is observed by counting coincidences between the two output ports, while changing the distinguishability of the two input photons. If they are indistinguishable the rate of coincidences will drop, ideally to zero, since all photons will leave the beam splitter in pairs. We show one example of such a resulting dip in figure 2.3. In this measurement, we have used photon pairs from our spontaneous parametric down-conversion source (cf. section 2.2), split them, changed their relative time delay via a path length difference and then overlapped them on the beam splitter. Figure

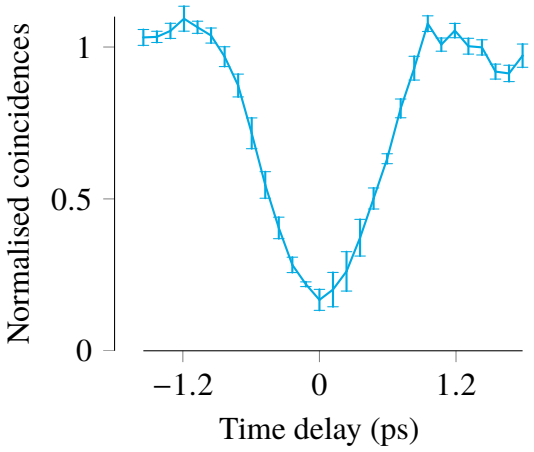

Figure 2.3: Example of a Hong-Ou-Mandel dip in the coincidences count rate as a function of the relative time delay between signal and idler photon. With perfectly indistinguishable photons the dip should extend to zero coincidences at zero time delay. In this measurement, however, the photons are slightly distinguishable, especially in frequency.

2.4 schematically depicts this measurement. A figure of merit for Hong-Ou-Mandel dips is the visibility of the interference defined as $V = (C(\infty) - C(0))/C(\infty)$, where $C(0)$ is the coincidence count rate at the minimum of the dip and $C(\infty)$ the count rate far away from the minimum, where there is no fluctuation anymore.

Apart from the dip visibility being a measure for the indistinguishability of the two photons, the interference dip also reveals information about the spectrum. For a specific spatial mode, the shape of the Hong-Ou-Mandel dip is given by the Fourier transform of the spectra of the photons.

Due to the importance for practical schemes and its fundamental significance, the Hong-Ou-Mandel interference has been demonstrated in a wide variety of different systems. In principle the interference can be observed for any pair of bosons, since equations 2.18 and 2.19 are generic. One of the difficulties of translating the interference to other systems is the implementation of the beam splitter. This has been overcome for example for atoms [46] with Bragg scattering or for plasmons [47] with waveguide evanescent couplers. Another remarkable experiment interferes phonons in trapped ions [48]. Coming back to photons, there is also a lot of interest to show the interference of photons from independent sources [49, 50], as this signifies their indistinguishability and thus demonstrates good control over the individual sources. Interestingly, a similar effect has recently been observed for electrons [51], where due to the Pauli exclusion principle, the electrons always leave the beam splitter separately.

We can use the Hong-Ou-Mandel interference to study the behaviour of our source. See figure 2.5 for an example comparing two different pump beam waists. As discussed in section 2.4, the pump beam waist controls the degree of spatial entanglement, but it also influences the spectral width of the down-converted photons. In figure 2.5 (a) we see that the spectral width is much smaller for a large pump beam waist than for a small waist. The temperature of the non-linear crystal shifts the spectra of signal and idler with respect to each other and thus allows us to measure the overlap between the two. Comparing to figure 2.5 (b) it becomes apparent, that the temporal width is inversely connected to the spectral width [52].

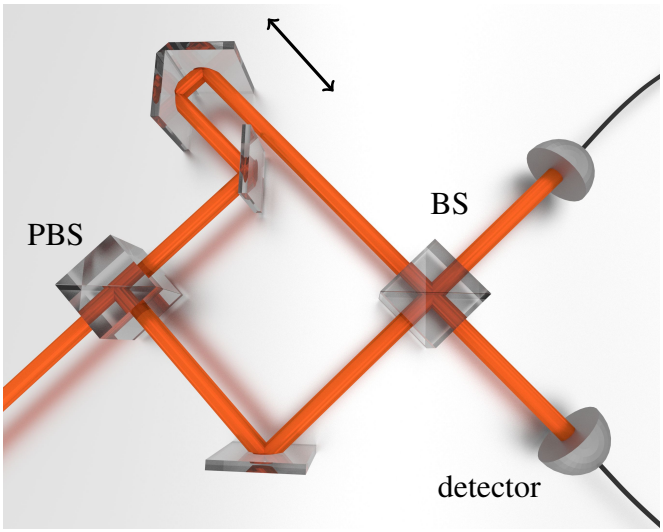

Figure 2.4: Schematic of a spatial delay line to create a Hong-Ou-Mandel interference dip as shown in figure 2.3. Photon pairs arrive on the polarising beam splitter (PBS) from the left and are split. One of photons takes a path with a variable length before both photons overlap on a 50:50 beam splitter (BS), where the quantum interference takes place. The signature of a reduced coincidence rate is measured with single photon counters, if the path-lengths of both photons are equal.

2.4 Photonic degrees of freedom

A single photon can in principle be created in arbitrary electromagnetic modes and thus inherit the properties of these modes [53, 54], energy, wave-vector, helicity, total angular momentum, etc. The situation becomes more complex, when considering correlated photon pairs. In the following we discuss pairs generated by spontaneous parametric down-conversion and their degrees of freedom.

The most fundamental correlation between signal and idler photons from SPDC, is their temporal connection. Usually, since the down-conversion is parametric, they are born at the same time and are thus strongly correlated in time [34]. This fact is used to identify two photons as a pair and for the generation of single photons, where the detection of an idler photon heralds the existence of a signal photon. Correlation in time automatically entails anti-correlation in frequency, via Fourier duality. The opposite case of correlated frequencies and anti-correlated timing has been shown with pulsed pump beams in long crystals [55–57]. In our source, we are using continuous wave pumping and thus observe frequency anti-correlation. Control over the separation of signal and idler mean wavelengths is possible via temperature tuning the non-linear crystal or by changing the pump wavelength for a specific non-linear crystal.

The reason for all correlations can be found in the phase matching conditions (cf. equation 2.15). Similar to time and energy, also space and momentum correlations can be found in SPDC pairs [58–62]. By moving between real and Fourier space in the far field of the source, these correlations can be interchanged [63], from correlation to anti-correlation in space (or vice versa in momentum). A convenient basis to analyse spatial correlation of the down-converted photons are the Laguerre-Gaussian modes, which are eigenstates of the orbital angular momentum of light (see next section 2.5). Since they form a complete set of

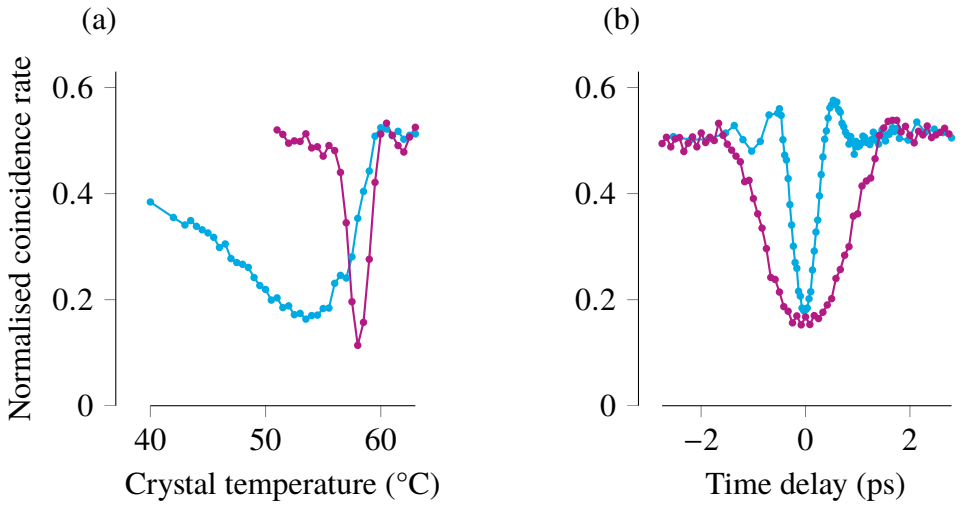

Figure 2.5: Direct comparison of the Hong-Ou-Mandel dips with two different pump beam waists. The blue data points correspond to a beam waist of 5.4 µm and the purple measurement to a beam waist of 32.4 µm. Coincidence rates are normalised such, that the coincidence rate for fully distinguishable photons is 0.5. (a) Hong-Ou-Mandel dip as a function of the crystal temperature and (b) as a function of the relative time delay. Dip width in crystal temperature and relative time delay are inversely related.

solutions for the paraxial Maxwell equations, every mode function (cf. equation 2.16) can be expanded in Laguerre-Gaussian states [64–66], carrying orbital angular momentum. The degree of spatial correlations between signal and idler photons can be controlled by choosing the beam waist of the focused Gaussian pump beam inside the non-linear crystal [59]. The dependence is a convex function of the beam waist and on either side of the minimum, the down-converted photon pairs are entangled in orbital angular momentum [67, 68].

All of these correlations are unwanted for the generation of heralded single photons from SPDC. Here, great efforts are being undertaken to remove and minimise the correlations [35]. Otherwise, the purity of the heralded photon is degraded, since properties of the detected photon would in principle allow to obtain information about the heralded photon.

2.5 Angular momentum of light

The total angular momentum of a beam of light is often described as a combination of the well known spin orbital angular momentum, which is connected to the polarisation and the orbital angular momentum [65, 69], which is connected to the phase front of the beam. With highly focused fields the separation between spin angular momentum and orbital angular momentum disappears and a better description is given in terms of total angular momentum J_z and helicity Λ [70]. However, in the paraxial limit, spin and orbital angular momenta can describe the fields well [71] and for this section, we will keep to this separation, since it is widely used in the literature.

In a beam of well defined spin angular momentum, the spin can take one of two values: $S_z = \pm\hbar$, corresponding to left and right circular polarisation. For the orbital angular momentum an infinite number of values are possible: $L_z = l\hbar$ with integer l. Solutions to Maxwell's equations that have a well defined orbital angular momentum are the Laguerre-

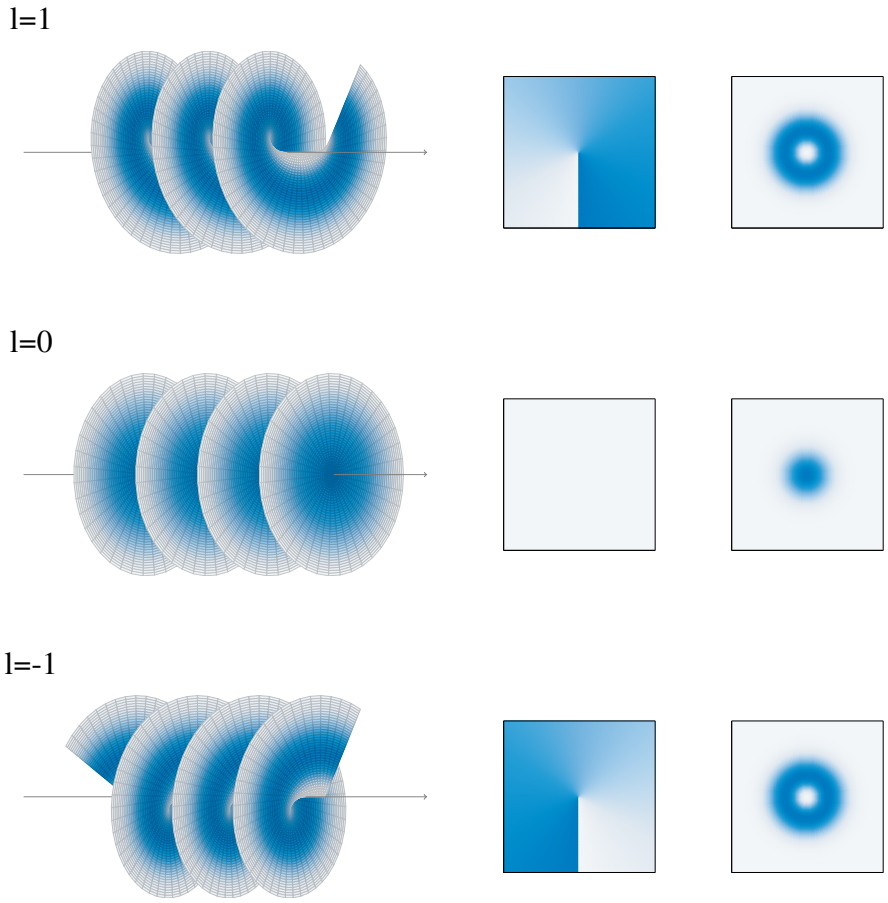

Figure 2.6: Overview over wavefront (left column), phase (centre column) and intensity (right column) of three Laguerre-Gaussian beams. The upper row shows a beam with one quantum of of orbital angular momentum per photon, which corresponds to an azimuthal index of $l = 1$. The middle row shows $l = 0$, which is identical to a Gaussian beam and the last row shows a beam with $l = -1$. In all cases the radial index is zero.

Gaussian modes. Figure 2.6 compares three of those beams. A Laguerre-Gaussian beam is defined, among other quantities, by its azimuthal index l, which is equivalent to the number of quanta of orbital angular momenta carried per photon. Mathematically, this manifests as a phase factor $e^{il\phi}$ in the electric and magnetic field strengths, where ϕ is the angle around the propagation axis. The upper row of the figure shows a first order Laguerre-Gaussian beam with $l = 1$, which carries one quantum of orbital angular momentum per photon. Characteristically, the phase front wraps around the axis of propagation as seen in the first column, where a surface of constant phase is shown. The phase in a plane perpendicular to the propagation axis is depicted in the second column with the vortex of undefined phase in the centre. In the intensity pattern shown on the right, this vortex results in a vanishing intensity in the centre and the typical doughnut shape. In the case of $l = 0$ a Gaussian beam is retrieved, as shown in the second row. The phase fronts are flat and separated and the intensity profile is the well known Gaussian bell curve. A beam with $l = -1$ again carries one quantum of orbital angular momentum per photon, but this time with inverted orientation of the rotation.

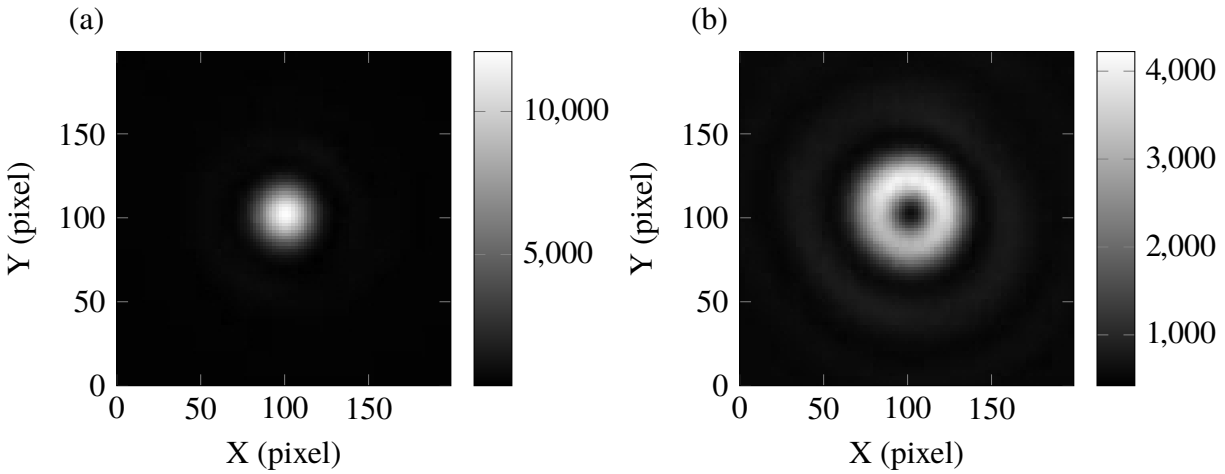

Figure 2.7: Camera images of the beam profile of an initially Gaussian beam after having passed through a q-plate that is electrically switched off (a) or on (b). Both images employ the same colormap, showing intensity with arbitrary units.

Electromagnetic beams carrying orbital angular momentum have found applications in a number of different areas. Combining a Gaussian beam to facilitate fluorescence in microscopy samples and a Laguerre-Gaussian beam to inhibit it again in a ring around the excitation, has allowed surpassing the diffraction limit with stimulated emission depletion microscopy [72] as one example. The theoretically unlimited range of orbital angular momenta available makes it interesting for information multiplexing [73] in optical communications. In the field of optical trapping, orbital angular momentum provides a tool for manipulation and sensing of small particles [74, 75]. In Astronomy, analysis of orbital angular momentum might add additional information about a source [76] such as the surrounding of a black hole [77].

The applications mentioned so far are concerned with angular momentum of classical beams. But also for quantum information technologies, orbital angular momentum is of great interest [67]. For example Hong-Ou-Mandel interference has been demonstrated between single photons of variable orbital angular momentum [78]. And recently, a quantum memory was realised for states carrying orbital angular momentum [79].

For all these applications of orbital angular momentum, controlled creation and detection of specific modes is important. Detection of orbital angular momentum [80, 81] is intimately connected to its creation. Early schemes to modify the orbital angular momentum content of a beam relied on polarisation independent methods like cylindrical lenses [69], spiral phase plates [82] or holograms [83], directly imposing the helical phase that is characteristic of orbital angular momentum beams.

More recently, Prof. Lorenzo Marrucci and coworkers [84, 85] have developed a method that couples spin with orbital angular momentum using anisotropic inhomogeneous media. In a slab of liquid crystal, the optical birefringent axis is changed locally, creating a pattern with a topological charge in the centre. This charge determines the amount of orbital angular momentum being transferred. The orientation of the optical axis wraps around the centre q times, where q must be integer or half integer, since the optical axis does not have a polarity. Figure 2.8 shows the orientation of the optical axis schematically for two different q-plates. The change of the optical axis creates a topological defect at the centre of the plate with charge q. The change of the orbital angular momentum is then $\Delta l = \pm 2q$, where

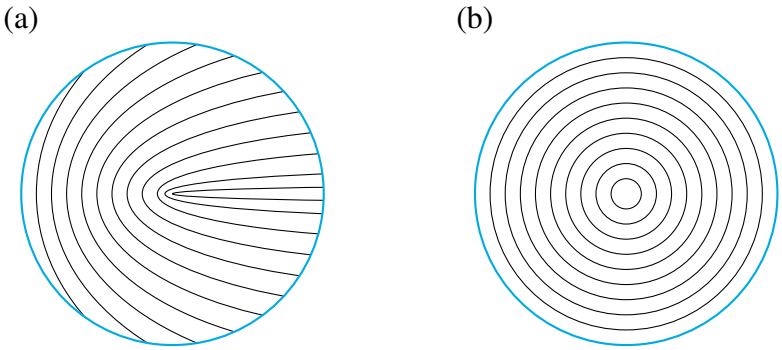

Figure 2.8: Schematic of the orientation of the local optical axis within the liquid crystal of a q-plate, indicated in each point by the tangent to the curves shown. (a) q-plate with $q = 0.5$ and (b) with $q = 1$. Figure adapted from [84].

the sign is determined by the circular input polarisation. This polarisation is flipped in the transformation. That means for $q = 1$ the transfer happens purely from spin angular momentum to orbital angular momentum without any momentum exchange with the q-plate. The theoretical efficiency can be very high, approaching 100 % [86]. For the experiments described later in this thesis it is very convenient that the q-plate can be electrically tuned and switched from in-active to active [87, 88], as shown in figure 2.7 for a beam of SPDC photons in a Gaussian state.

2.6 Plasmonic nanoapertures

The study of light scattering off sub-wavelength apertures has been an active area of research for many decades now, starting with the seminal theoretical investigation by Bethe [89] in 1944. Since then, the discovery that the transmission through apertures in metallic films can be much stronger than predicted by Bethe [90], created a lot of interest. The effect is now known as "extraordinary transmission" and is attributed to the excitation of localised plasmons at the interface of metal and dielectric [91].

The key behaviour of isolated circular nanoapertures for the experiment reported in this thesis, is their influence on the helicity of transmitted light [92]. Since the light must be focused strongly, the separation into spin and orbital angular momentum is not adequate. Instead, total angular momentum and helicity – the projection of the total angular momentum on the linear momentum – provide a valid description both in the paraxial limit as well as for arbitrarily focused beams [70]. For all experimental purposes, however, one can think of the two helicity states just as left and right circularly polarised. This is possible, because both in preparation and detection the beam is virtually paraxial and due to the fact that an aplanatic lens [93] does not alter the helicity state [94].

An incident photon of well defined helicity Λ and total angular momentum m undergoes a transformation into a superposition of an output photon with the same helicity and one of opposite helicity:

$$\hat{a}^{\dagger}_{m,\Lambda} \longrightarrow \alpha \hat{b}^{\dagger}_{m,\Lambda} + \beta \hat{b}^{\dagger}_{m,-\Lambda} \quad . \tag{2.20}$$

The creation operator for input photons is denoted here as $\hat{a}^{\dagger}$ and the creation operator for photons after the interaction with the nanoaperture as $\hat{b}^{\dagger}$. The relative strength of changed and unchanged helicity fields is governed by the two coefficients α and β. The total angular

momentum is conserved due to the cylindrical symmetry of the system. The helicity on the contrary is not conserved in this interaction, because of the broken duality symmetry [70]. The relative strength of the output fields with changed and unchanged helicity naturally depends on the specifics of the nanoaperture and the incident field. Generally, however, for smaller apertures they become more and more comparable, due to the stronger coupling to large transverse momenta [92]. The probability of a helicity flip, given by the parameters α and β can only be determined experimentally [92, 95] or via simulation [96].

If the input for example is a right circularly polarised Gaussian beam

$$\hat{a}^{\dagger}_{1,+} \longrightarrow \alpha \hat{b}^{\dagger}_{1,+} + \beta \hat{b}^{\dagger}_{1,-} \quad , \tag{2.21}$$

the collimated output after the transmission through the aperture consists of an identically polarised Gaussian beam and a left circularly polarised Laguerre-Gaussian beam carrying two quanta of orbital angular momentum $l = \Lambda - m$ per photon.

3

Controlling the SPDC Wave Function

Photon pairs from spontaneous parametric down-conversion are a widely used resource for photonic quantum technologies. Because all of their degrees of freedom can be tailored for specific applications, these photon pairs are very versatile. Control over all degrees of freedom is essential for our project in order to understand the coupling to nanostructures. In this chapter, we report a novel way of influencing the temporal wave function. This is especially important for experiments relying on the interference of the two photons and their indistinguishability.

We have found, studied and explained the surprising behaviour of temporal correlations of the pair with respect to the position of the non-linear crystal for type II, continuously pumped SPDC. We attribute this behaviour to the interplay between spatio-temporal correlations of the wave function and selective detection. To measure the influence of the crystal position, we have developed a method to directly measure arrival time differences with a resolution of a few 0.1 ps even with single photon detectors which time resolutions are limited to several 10 ps.

Starting in section 3.1, we recount the circumstances that lead to the finding and present a first measurement based on Hong-Ou-Mandel interference. In section 3.2 we discuss why this is a surprising behaviour and in that course examine where SPDC photons are created in a finite length non-linear crystal. We subsequently present the theoretical reason behind the effect in section 3.3. Afterwards in section 3.4, we start with a discussion of the technique used for the first measurement and also introduce the direct time delay measurement method, which allows us to extend the measurement to other detection modes. In the following section 3.5 we present the measurement results based on the new method, demonstrating the robustness of the effect against spatial and spectral filtering. We conclude the chapter with a discussion of the findings and their impact in section 3.6.

3.1 Motivation

During the course of this project we developed and built the SPDC source described in section 2.2 with the objective in mind to interact with plasmonic nanostructures. As part of

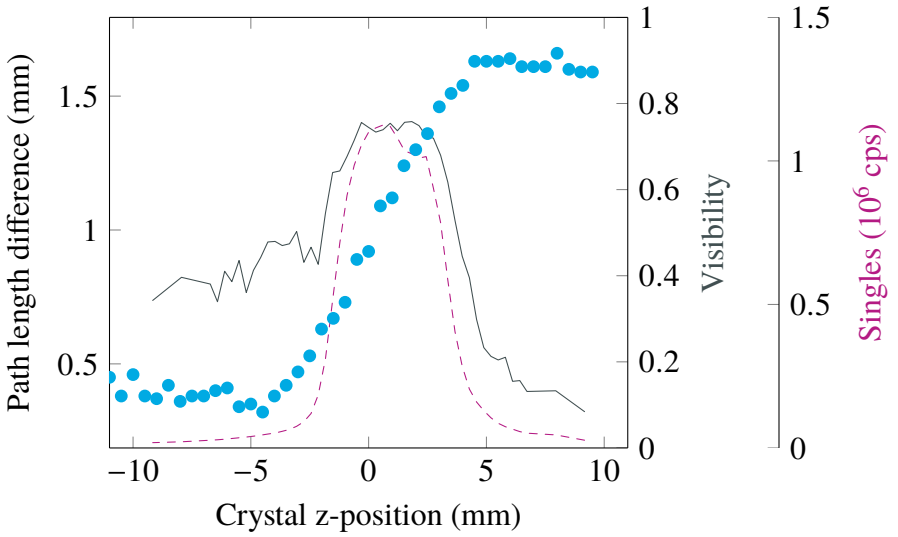

Figure 3.1: Shift of the Hong-Ou-Mandel dip position as a function of the down-conversion crystal position (blue dots) shown together with the visibility (solid grey line) and the singles count rate (dashed purple line). The Hong-Ou-Mandel dip position for each data point is extracted from a full Hong-Ou-Mandel dip scan.

the characterisation process, we set up a Hong-Ou-Mandel interference experiment to test the indistinguishability of the down-converted photons. Surprisingly, we found that after determining the dip position once and then measuring the dip visibility only at this position, the visibility changed strongly between measurements. It was only after some tests, that we found the longitudinal position of the non-linear crystal with respect to the pump beam waist to influence the location of the Hong-Ou-Mandel dip. We then performed a systematic measurement, changing the crystal position along the beam axis and recording the location of the resulting interference dip. We show in figure 3.1 (blue dots) the path length difference necessary for optimal interference as a function of the non-linear crystal position. Alongside, we also show the visibility of the underlying Hong-Ou-Mandel dip (solid grey curve) and the singles count rate (dashed purple curve). Zero crystal displacement corresponds to a centred pump beam focus and positive values indicate a shift in the direction of pump propagation. The crystal has a total length of 15 mm. Due to diffraction of the pump beam and its interplay with the crystal movement, the pump focus lies within the crystal from −5 mm to 5 mm. We see that the dip position changes nearly linearly within this interval over a total path length difference of 1.2 mm, which is equivalent to a time difference of 4 ps. Both singles count rate and visibility drop off as soon as the pump focus leaves the crystal.

We did not expect such a behaviour, that could naively be attributed to a localised creation of photon pairs inside the crystal. In the following, we will discuss where SPDC photons are created and how this puzzling effect can be explained.

3.2 Where are SPDC photons created?

Why does it matter where photon pairs are born in a non-linear crystal? For type II SPDC (cf. section 2.2), the two photons are orthogonally polarised and the non-linear crystal is birefringent. This means, both photons experience different group velocities inside the crystal. This difference will lead to a time delay between signal and idler photon and its

magnitude depends on the distance they travel through the crystal. A pair created close to the end facet of the non-linear crystal, leaves the crystal with only a small time delay and a pair created in the front, will acquire a large delay. Having a delay between the two photons affects their distinguishability and this is important for all experiments based on quantum interference of two photons.

In brief, the answer to the question of birthplace is that there is no specific place of creation, as long as the pair is not measured. SPDC is a coherent process [34] and each pair has the same probability distribution of time delays. A specific delay only manifests itself, when the pair is measured. Probabilities from the front to the end of the crystal coherently add up to the final temporal wave function of the pair.

In the following, however, we describe measurements and present results that show a dependence of the measured time delays on the position of the down-conversion crystal with respect to the pump beam focus. This would seem at odds with the coherent production. One could now argue, that even if the creation is coherent, there may be places in the crystal that are more likely to produce a photon pair than others, like for example at the pump focus. This effect would indeed alter the temporal wave function when moving the crystal. However, such a region does not exist. Even though SPDC is a non-linear process, the production of pairs is linear in the pump intensity [32], because in our case pump depletion is negligible, due to the very small total efficiency of the process. This means the number of pairs created is independent of the pump intensity distribution and only depends on the total power [97, 98]. As long as the pump beam is fully contained within the transverse extent of the crystal, a locally varying production efficiency can thus not explain our observations.

We show in the following section that the reason for our observation lies in the combination of spatio-temporal correlations [99] of the SPDC wave function, a spatially dependent phase imprinted by the collection lens and the fact that not all photons are detected. Such correlations between different degrees of freedom of SPDC pairs are often unwanted. For example in heralded single photon generation [35, 100], where correlations between the heralding and the heralded photon negatively impact the purity of the heralded photon. One common way of overcoming these correlations is by filtering in the relevant degrees of freedom [101]. In other situations, these correlations can however also be used and are a subject of focused research efforts [102–105].

We know of only one work that looked into the influence of the non-linear crystal position on the biphoton state. Di Lorenzo Pires and coworkers [97] analysed intensity patterns at the exit facet of the non-linear crystal in dependence of its position for type I SPDC.

Coming back to the question of where SPDC photons are created, the answer of coherently created photons over the whole length of the crystal is still valid. But, we have found a way to influence the temporal correlations in a non-trivial way, by using the spatio-temporal correlations of the wave function.

3.3 Theoretical explanation of the time delay shift

We want to briefly show the general line of argument for explaining the time delay shift in this section. A detailed account is available in reference [106] and Nora Tischler's PhD thesis [107].

Any effect on the temporal correlations must be connected to the two-photon wave

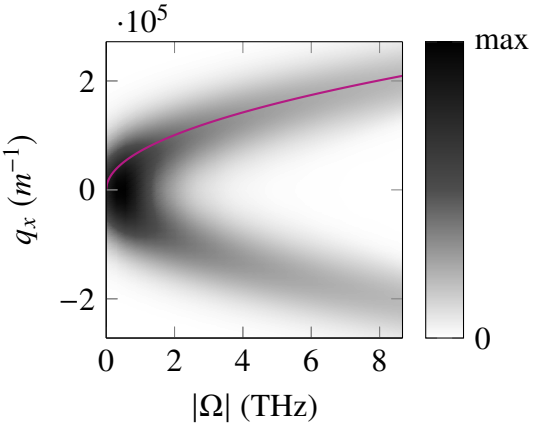

Figure 3.2: Illustration of the spatio-temporal correlations of the SPDC wavefunction. We depict here the probability to observe a photon with specific combination of q_x and Ω and $q_y = 0$, while not considering the other photon. The solid line emphasises the quadratic dependence between Ω and $|\mathbf{q}|^2$. The probabilities are based on simulations of the SPDC wavefunction for experimentally relevant parameters by Nora Tischler.

function:

$$|\Psi\rangle = \int \mathrm{d}\mathbf{q}_s \, \mathrm{d}\mathbf{q}_i \, \mathrm{d}\omega_s \;\; \Phi(\mathbf{q}_s, \mathbf{q}_i, \omega_s, \omega_i) \, \hat{a}^\dagger(\mathbf{q}_s, \omega_s, \sigma_s) \, \hat{a}^\dagger(\mathbf{q}_i, \omega_i, \sigma_i) \, |0\rangle \quad , \tag{3.1}$$

where $\mathbf{q}$ is the transverse wave-vector, ω the angular frequency, and σ the polarisation. The subindices indicate signal s or idler i photons. The photon creation operators $\hat{a}^\dagger(\mathbf{q}, \omega, \sigma)$ are characterised by transverse wavenumber, frequency, and polarisation. The mode function $\Phi(\mathbf{q}_s, \mathbf{q}_i, \omega_s, \omega_i)$ contains all correlations and specificities of the creation process. We integrate over only one angular frequency here, because we can safely approximate our narrow band pump laser as a monochromatic field, which fixes the idler frequency: $\omega_i = \omega_p - \omega_s$ and we can write the frequencies in terms of the deviation from half the pump frequency $\omega_{i/s} = \omega_p/2 \pm \Omega$.

To understand the origin of the time delay shift, we then calculate the second order correlation function between signal and idler photons with a variable delay between them:

$$G^{(2)}(\tau) = \left| \langle 0 | \, \hat{E}_i^{(+)}(t - \tau/2) \hat{E}_s^{(+)}(t + \tau/2) \, |\Psi\rangle \right|^2 \quad . \tag{3.2}$$

Experimentally, this second order correlation function can be measured through the number of coincidences as a function of the time delay. By inserting our specific two-photon wave function, it should reveal the origin of the dependence on the crystal displacement. We find:

$$\begin{aligned} R_{coinc}(\tau) \propto \Bigg| \int \mathrm{d}\mathbf{q}_s \, \mathrm{d}\mathbf{q}_i \, \mathrm{d}\Omega \;\; & \exp\left(i(k_{sz}(-\Omega, \mathbf{q}_s) + k_{iz}(\Omega, \mathbf{q}_i)) \, L/2\right) \\ & \times \exp\left(id \left(\frac{|\mathbf{q}_s|^2}{2k_{air}(-\Omega)} + \frac{|\mathbf{q}_i|^2}{2k_{air}(\Omega)} \right) \right) \\ & \times \operatorname{sinc}\left(\Delta k_z \frac{L}{2} \right) g(\mathbf{q}_s, \mathbf{q}_i, z_c) \;\; \exp(i\Omega\tau) \Bigg|^2 \quad , \end{aligned} \tag{3.3}$$

where L is the length of the crystal, k_z are longitudinal wave-vectors and $g(\mathbf{q}_s, \mathbf{q}_i, z_c)$ depends on the spatial collection modes. The first exponential term is due to the propagation of the photons through the crystal. The cardinal sine term originates from the phase matching, where $\Delta k_z = k_{pz} - k_{sz} - k_{iz}$ is the longitudinal wave-vector mismatch. The second exponential term captures the effect of the collection lens and is especially interesting with respect to explaining the time delay. It connects the distance between non-linear crystal and collection lens d with the transverse momenta $\mathbf{q}_s$ and $\mathbf{q}_i$ for signal and idler. This is the first ingredient to the explanation of the time delay shift. The second ingredient is the non-linear relationship between transverse momenta and the frequency of signal and idler. Indeed, it has been shown [103, 107], that Ω and $|\mathbf{q}|^2$ are linearly related, when the photons propagate along one of the crystal axes, as in our case. We show this relationship for a simulated wave function in figure 3.2. Numerical calculations show that without spatio temporal correlations of this form, no such time delay can be observed.

Combining both ingredients leads to a time delay, because the exponential from the collection lens effect now connects distance d with the frequency difference of signal and idler. After the integration over Ω the exponential depends on the time delay τ relative to the distance between crystal and collection lens d. In a simplified model, equation 3.3 reduces to

$$R_{coinc}(\tau) \propto \frac{2\pi}{DL}\mathrm{rect}\left(\frac{1}{DL}\left(\tau - D\frac{L}{2}\right)\right)\left|\int \mathrm{d}\mathbf{q}\exp\left(\frac{-i|\mathbf{q}|^2}{nDk_{air}(0)}(\tau-\tau_0)\right)g(\mathbf{q})\right|^2 \quad , \qquad (3.4)$$

where $D = \left(\frac{\partial k_s}{\partial \Omega} - \frac{\partial k_i}{\partial \Omega}\right)$ and $g(\mathbf{q})$ is collection of terms depending only on the transverse momentum. We see that the important exponential depends on τ_0, which in turn depends on the distance between crystal and collection lens and is thus responsible for the time delay. The average time delay increases, when d is reduced. A detailed derivation is given in reference [106, 107].

3.4 Measuring small time delays

A modern silicon avalanche diode has a timing resolution of a few tens of picoseconds to a few nanoseconds, depending on quality, as well as desired wavelength and quantum efficiency. This resolution is large compared to the maximum delay a pair can acquire over the length of a typical SPDC crystal of a few mm. In our case, the ppKTP crystal has a length of 15 mm, which corresponds to a maximum delay of 5.3 ps. To measure any shift of the average time delay within this interval, a resolution below 1 ps is necessary.

Hong, Ou and Mandel demonstrated in their seminal paper [41], how to use the two photon interference to translate a time measurement into a length measurement, by varying the path length of one of the two photons before overlapping them. We have used this approach in section 3.1, showing that the necessary path length difference changes with the positioning of the SPDC crystal, which in turn signals a change in the time delay. In addition, we also show that it is indeed possible to measure the time delay directly, using modern avalanche photo diodes. This enables us to test the effect under different experimental conditions. Figure 3.3 shows the basic structure of our experiment for both types of measurements. The pump beam of 404 nm wavelength is focused into the ppKTP crystal. The crystal can be displaced along the pump beam axis by a computer controlled stage. The down-converted photon pairs are collected by another lens and then separated from the pump beam by a longpass filter. A

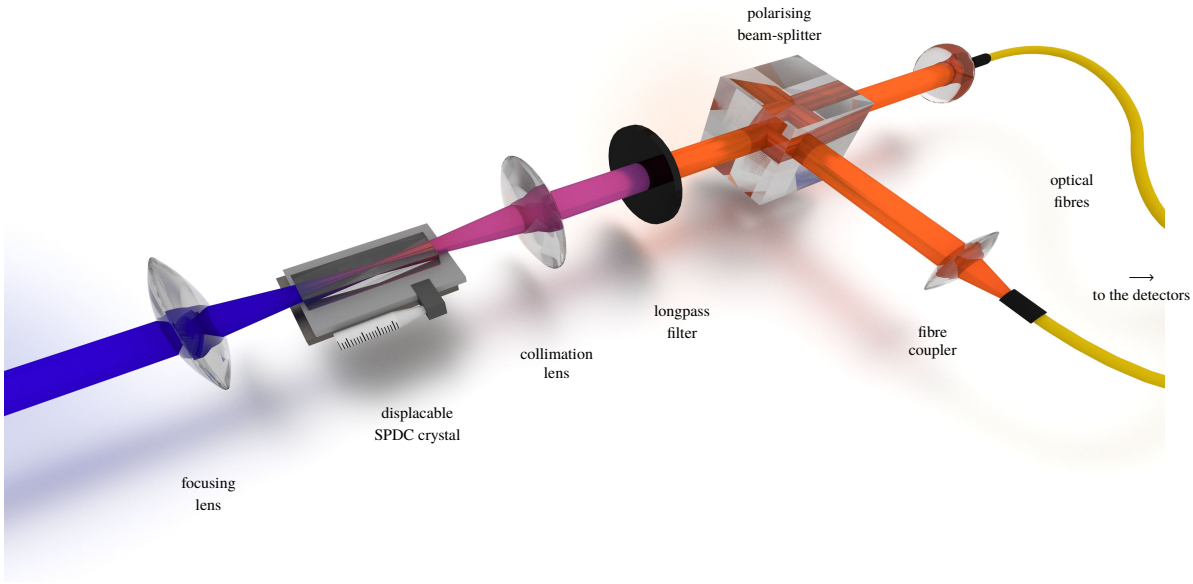

Figure 3.3: Experimental setup for time delay measurements in dependence on the longitudinal position of the down-conversion crystal with respect to the collimation lens. The pump beam is focused into the SPDC crystal and the down-converted photons are collimated by another lens. A longpass filter rejects the pump beam and then the pair of orthogonally polarised photons is split by a polarising beam-splitter and coupled into fibres. We subsequently employ two different measurement schemes that are not shown in this schematic. The photons are either directly detected by avalanche photo diodes and their arrival time difference measured, or their delay is measured via a Hong-Ou-Mandel interference on an additional fibre based beam-splitter, before the detectors. For this Hong-Ou-Mandel type measurement, one of the fibre-couplers can be displaced along the beam axis.

polarising beam splitter then sends signal and idler photons along different paths. From here on, the two measurement techniques diverge.

3.4.1 Hong-Ou-Mandel based approach

Measuring a length is much easier than measuring the corresponding time interval for photon delays on the order of a few picoseconds. Our initial measurement thus employed a standard Hong-Ou-Mandel interferometer to measure changes in the time delay distribution between signal and idler photons when displacing the down-conversion crystal. After the pair has been split, each photon is coupled to a single mode fibre and they are then overlapped again on a fibre beam splitter. One of the incouplers is mounted on a movable stage, which allows us to control the relative path length from the polarising beam splitter to the fibre beam splitter. Coincidence events between the two output ports are registered with avalanche photo diodes connected to a time to amplitude converter. If the path-length difference exactly compensates the inherent time delay of the photons, a reduction of the coincidence count rate is observed (cf. section 2.3). By recording the necessary path-length difference to compensate the time delay as a function of the SPDC crystal position, we can observe the behaviour of the temporal correlations. Additionally, the shape of the interference dip offers insight into the spectrum of the photon pair. However, this measurement scheme can only be used with single mode fibres and thus keeps us from measuring the time delay in other detection situations. We

address this shortcoming in the following with a direct time delay measurement, where we can use arbitrary detection modes.

3.4.2 Direct time delay measurement

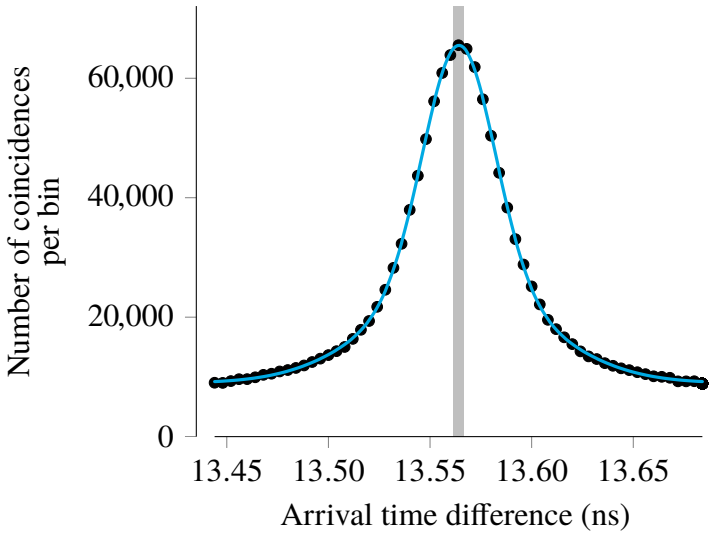

Figure 3.4: Example histogram showing the distribution of arrival time differences between signal and idler photons. Black circles indicate counted number of photons and the blue line shows the fit to the data, from which the peak position is extracted. The width of the peak is dominated by the timing jitter of the APDs. Due to slight electrical differences between the two counting channels there is always an offset in the time difference and only relative changes are important. The absolute time difference between signal and idler can be measured by exchanging them in the detection channels with a half wave-plate. The integration time for the shown histogram was 52 s. One time bin is 4 ps wide. Indicated as a grey stripe is the temporal width over which the time delay of a photon pair from our crystal could theoretically vary.

To allow for the measurement of different detection modes we also implement a direct time measurement. In this case, we remove the fibre-beam splitter. Instead, we either attach single photon counters directly to the single mode fibres or remove the fibre coupling altogether and use free space detectors to capture a much larger fraction of the photon pairs. The connected time to amplitude conversion electronics (see appendix A for details on the coincidence detection system) builds a histogram of recorded delay times. The challenge of this approach is captured in figure 3.4, where we show such a histogram. The black circles depict data points, the blue line is a fit to the histogram peak and the grey stripe indicates the maximum interval of time delays that could potentially be acquired in our length of non-linear crystal. The width of the histogram is purely due to the timing jitter of the APDs and the counting electronics. We are thus trying to measure time delay shifts that are much smaller than 5.3 ps with a distribution that itself has a full width at half maximum of 46 ps, while each bin is already 4 ps wide.

We are able to measure such small changes with an error significantly smaller than the bin width, by repeatedly integrating over several minutes, fitting a double Gaussian function to each histogram peak and extracting its peak position. This approach is only limited by the available signal to noise ratio and the stability of the coincidence counting system.

Guaranteeing this degree of stability is challenging. A typical measurement cycle consists of the acquisition of multiple histogram recordings at several different SPDC crystal positions. To counteract slow drifts of the electronics, the whole cycle is automatised and programmed to take reference measurements after each single measurement. We can thus detect and correct for potential drifts of the counting electronics. Appendix A discusses the coincidence detection system and its stability in more detail.

3.5 Results

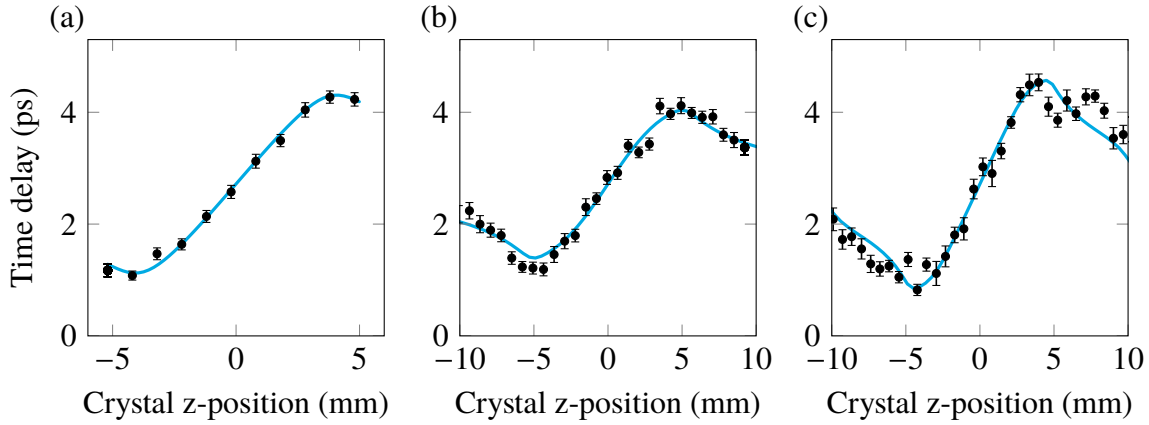

Figure 3.5: Time delay between signal and idler as a function of the down-conversion crystal position along the pump beam. (a) With detection after incoupling into single mode fibres, (b) with free-space detection after a 2.5 nm wide bandpass filter and (c) with free-space detection after a longpass filter. The blue line shows the theory prediction for the experimental parameters, which are: (a) pump beam waist $w = 12.9\,\mu\text{m}$, crystal temperature $T = 59\,^\circ\text{C}$, detection waist $w_f = 18\,\mu\text{m}$, (b) $w = 11.4\,\mu\text{m}$, $T = 58\,^\circ\text{C}$, $l = 40\,\mu\text{m}$, (c) $w = 11.4\,\mu\text{m}$, $T = 60\,^\circ\text{C}$, $l = 40\,\mu\text{m}$. l denotes the side length of the quadratic free-space detection area. The error bars span one standard deviation, assuming Poissonian photon statistics.

The findings reported in section 3.1 are confirmed by the direct time delay measurements shown in figure 3.5. Now, we are able to compare different experimental situations and detection settings. Figure 3.5 (a) shows the dependence of the average time delay on the crystal position in the case of single mode fibre coupled detection. Figure 3.5 (b) and (c) present the same for free space detection with spectral filtering and without spectral filtering respectively. The experimental results agree very well with the theoretical prediction shown as solid blue curves. These theoretical calculations are based on equation (3.3) and only include one adjustable parameter, which is the detection mode diameter, or in the case of free space detection, the detector area. All other parameters are fixed by the experimental conditions. Leaving the mode diameter free to adjust, allows us to compensate for an imperfect imaging system. The range of time delays shown, corresponds to the maximum delay a pair of orthogonally polarised photons could acquire when traveling through the whole length of crystal. The reason for the time delay not reaching these maximal positions, lies in the fact that our measurement captures the average time delay for a specific setting. The temporal wave function extends over the full range from 0 ps to 5.3 ps and we measure its average. When the whole delay distribution shifts towards the edge of possible values, naturally, the tail to the other side becomes more and more important for the average.

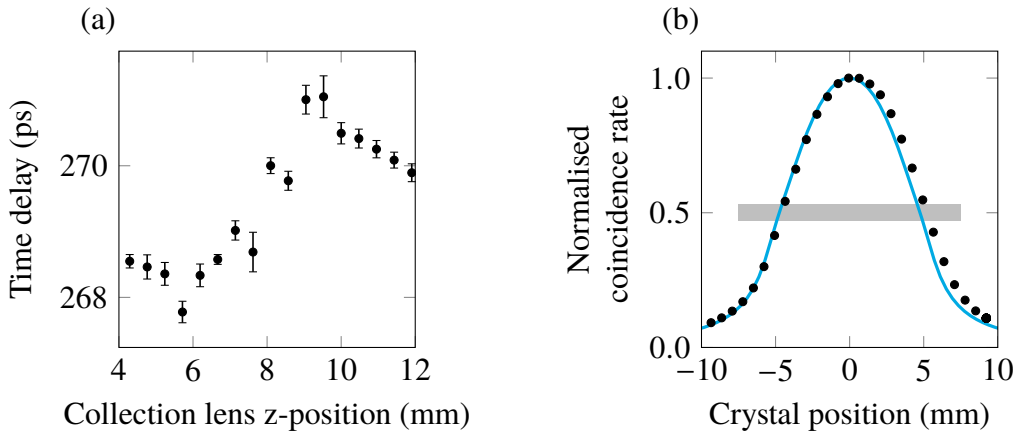

Figure 3.6: (a) Time delay between signal and idler as a function of the collection lens z-position in free space detection without a filter. The crystal is centred. The error bars span one standard deviation, assuming Poissonian photon statistics. Here, the origin of both axis is without meaning. (b) The coincidence count rate quickly diminishes, once the pump focus lies outside the non-linear crystal, even for free-space detection. The black dots show the experimental data, which was acquired alongside the data presented in figure 3.5 and the blue curve depicts the simulation results, for the same parameters as in that figure as well. The grey stripe indicates the length of the crystal of 15 mm.

Very similar curves can be obtained when scanning the collection lens position, since the effect depends on the distance between crystal and collection lens (cf. equation 3.3). See figure 3.6 (a) for an example scan with the collection lens in free-space detection. We have concentrated on the crystal displacement, since this case is more relevant in practice.

It is surprising that such unequal detection configurations result in very similar behaviour. When coupling the pairs to single mode fibres, many photons of the down-converted field are rejected and the selective nature of the detection is very clear. In the case of free space detection, on the contrary, almost all photons are collected and measured. Nevertheless, photons are lost also in this case, which leads to a comparably strong effect.

In addition to the robustness regarding the spatial detection, also spectral filtering only marginally influences the effect. Spectral filtering is a widely used technique to improve the indistinguishability of the photons for quantum interference and also to reduce spatio-temporal correlations. By comparing figures 3.5 (b) and (c) we see that in our case, a 2.5 nm wide bandpass filter is not enough to sufficiently suppress the spatio-temporal correlations and to inhibit the time delay shift.

Key to understanding the effect of time delay shifts is the observation that not all photons are collected, even for free-space detection. Together with the spatio-temporal correlations, this leads to changes in the temporal distribution. The single count rate we show in figure 3.6 (b) demonstrates the selective detection even for the free space case. The data is based on the same measurement and simulation as for figure 3.5 (b). The singles count rate depends on the crystal position and drops quickly, once the pump focus is outside of the crystal. Again, the agreement with the simulation is very good.

3.6 Discussion

We have demonstrated a surprising dependence of the average time delay between signal and idler photons (of type II SPDC) on the position of the non-linear crystal. Using different measurement techniques, we were able to accurately measure the shift. We have shown that the change in the average time delay is due to spatio-temporal correlations and their interplay with selective detection. If all photons produced through SPDC could be collected and measured, the temporal wave function would be rectangular with equal contributions of all possible delays. For realistic interference experiments based on type II SPDC, especially with long non-linear crystals, this effect is of importance. Particularly in cases where the down-converted photons are not split and arrive at the beam splitter together [40, 108]. Usually, this requires birefringent materials to compensate the time delay [34, 109]. Additionally, this effect provides a novel way to influence the temporal correlations of the wave function. It is, however, important to note, that the time delay induced by a shift of the crystal is different from the delay shift of a path length difference. The latter maintains the shape of the temporal wave function, whereas the crystal displacement deforms the wave function.

Both of our detection schemes are unable to resolve the temporal structure of the wave function and allow us to measure the average time delay only. The interference based approach can inherently return only one quantity, namely the dip minimum position and the direct measurement approach is already at the very limit of its resolution with only the average delay. It would, however, be very interesting to learn more about the actual structure of the temporal correlations. This becomes possible with the method described in the following chapter, where we use a generalised Hong-Ou-Mandel interference to reconstruct the complex spectral wave function of the photon pair, which includes the full knowledge of the temporal part of the wave function.

4

Measuring the SPDC Wave Function

Photon pairs from SPDC are a widely used resource for photonic quantum technologies. They are relatively easy to create in large numbers and can be modified to suit different purposes. Correlations can be engineered in and between different degrees of freedom. However, measuring their wave function and directly checking their state is technically challenging. As we have seen in the last chapter, the temporal characteristics of SPDC photon pairs can not be measured directly. We present a novel technique to reconstruct the complex spectral wave function of a two photon state produced by type II SPDC. This enables us to reconstruct the spectrum and the delay time distribution to a precision not achievable with current direct methods. Furthermore, the measurements show that we can control the temporal wave function, even beyond the capabilities presented in the previous chapter.

The first section 4.1 introduces the general idea and compares it to related schemes. The next section 4.2 briefly discusses the formulas and links between the data to be measured and the reconstructed wave function. How this data is acquired experimentally from an SPDC source is detailed in section 4.3. Following that, we present in section 4.4 three examples of reconstructed wave functions with very different properties. The chapter concludes with a discussion of this reconstruction technique and its potential applications (section 4.5).

4.1 Wave function reconstruction

In section 2.1 of the introduction, we have discussed wave functions as a means to fully describe pure quantum states. In the following, we demonstrate a novel reconstruction method of the complex spectral wave function for photon pairs created in type II spontaneous parametric down-conversion, making use of generalised Hong-Ou-Mandel interference. Due to their versatility and high production rates, SPDC pairs are widely used for quantum information experiments and beyond. To gain insights into the wave function and possibly use this knowledge to further adapt the SPDC pairs to the task at hand, considerable efforts have been undertaken to measure or reconstruct their wave function.

An early experiment aimed at measuring the two-photon temporal shape via the Hong-Ou-Mandel interference was performed by Sergienko and coworkers [110]. Other partial measurements of the wavefunction have been explored for the joint temporal density by femtosecond up-conversion [57] or for the spectral density with monochromators [35, 111, 112]. Full information about the spectral temporal wavefunction can be acquired by reversing the SPDC process via sum frequency generation [113–115]. This, however, requires very high non-linearities for the inversion and high count rates from the SPDC source. Other schemes are based on interference with short reference pulses to map the temporal density matrix of the two-photon states [116] or also the full wave function [117, 118]. These methods require a significant experimental effort and high stability.

If the spectrum of the biphoton is sufficiently narrow-band, much more narrow than in our case, direct time delay measurements are feasible with the nanosecond resolution of nowadays APDs. This has been demonstrated by Chen and coworkers [119]. They were able to add phase information from a tomography style measurement. One approach to reconstruct the spatial Wigner function was proposed by Douce and coworkers [120] using Hong-Ou-Mandel interference.

An advantage of our setup is the ability to not only measure the wave function, but to also influence it. We show that it is possible to shape the wave function, by a suitable selection of the detection mode. Other groups have demonstrated shaping of the temporal wave function via the modulation of the pump beam in four-wave mixing in cold atoms [113, 121].

4.2 Theory of the reconstruction scheme

At the centre of our reconstruction scheme lies the Hong-Ou-Mandel interference. In an intuitive picture, the strength of the interference is an indicator for the overlap of the temporal and the spectral shapes of the two photons. By shifting the wave function not only in time but also in frequency, while observing the strength of the interference, we can extract enough information to reconstruct the complex spectral wave function. The shift in time can be introduced with a path length difference and allows us to gain information about the Fourier transform of the modulus of the spectrum. Changing the temperature of the SPDC crystal leads to a shift in frequency, giving us direct insight into the spectral part of the wave function. Shifting the relative time delay between the two photons was central to our experiment in the previous chapter and has already been used in the original experiment of Hong, Ou and Mandel [41]. Analogously, it is possible to displace the spectra of both photons with respect to each other by changing the temperature of the non-linear crystal. We now present a brief introduction to the relevant quantities and formulas of our reconstruction method. Details of the derivation can be found in reference [122].

The full wave function of the photon pair after its creation is a function of several variables and parameters:

$$\Phi^{\text{full}}_{T,\omega_p}\left(\mathbf{q}_s, \mathbf{q}_i, \omega_s, \omega_i\right) \quad . \tag{4.1}$$

It depends on the transverse momenta $\mathbf{q}_s$ and $\mathbf{q}_i$ of signal and idler and their frequencies ω_s and ω_i. Furthermore, it is determined by specifics of the phase matching in the crystal, of which the crystal temperature T and the pump frequency ω_p are of interest to us. The method presented here reconstructs the complex spectral part of the wave function after arbitrary detection modes $G_s(\mathbf{q}_s)$ and $G_i(\mathbf{q}_i)$ have been chosen:

$$\Phi^{\text{spectral}}_{T,\omega_p}(\omega_s, \omega_i) = \int\int \mathrm{d}\mathbf{q}_s\, \mathrm{d}\mathbf{q}_i \;\; \Phi^{\text{full}}_{T,\omega_p}\left(\mathbf{q}_s, \mathbf{q}_i, \omega_s, \omega_i\right) G^*_{\mathrm{s}}(\mathbf{q}_s) G^*_{\mathrm{i}}(\mathbf{q}_i) \quad . \tag{4.2}$$

The situation is simplified by the fact, that we can safely assume a monochromatic pump, which fixes the relationship $\omega_p = \omega_s + \omega_i$ and allows us to write $\omega_s = \omega_p/2 - \Omega$ and $\omega_i = \omega_p/2 + \Omega$. We are thus left with a complex function of one variable that we would like to reconstruct. The approximation of monochromaticity is of course only useful for continuous wave pumping, which is the case in our experiment. However, an extension of this scheme could also be applied to pulsed pump operation.

To gain information about $\Phi^{\text{spectral}}_{T,\omega_p}$, we send signal and idler photons on a beam splitter and observe the coincidence rate. This Hong-Ou-Mandel interference provides information about the overlap of both photons in time and in wavelength, which we use to reconstruct the full spectral wave function. The normalised coincidence rate

$$R_{\text{coinc}}(\Delta S, T, \omega_p) \propto t^4 + r^4 - 2r^2t^2 \mathrm{Re}\left[f\left(\Delta S, T, \omega_p\right)\right] \quad , \tag{4.3}$$

depends on the length difference between signal and idler paths ΔS, the temperature of the down-conversion crystal T and the pump frequency ω_p. Furthermore, t and r are the transmission and reflection coefficients of the beam splitter and $f\left(\Delta S, T, \omega_p\right)$ is the overlap function:

$$f\left(\Delta S, T, \omega_p\right) \equiv \int \mathrm{d}\Omega \;\; \Phi\left(\Omega, T, \omega_p\right) \Phi^*\left(-\Omega, T, \omega_p\right) e^{2i\Delta S\Omega/\mathrm{c}} \quad . \tag{4.4}$$

The fact that the wavefunction only appears in symmetric form complicates its reconstruction. We call

$$F\left(\Omega, T, \omega_p\right) := \Phi\left(\Omega, T, \omega_p\right) \Phi^*\left(-\Omega, T, \omega_p\right) \tag{4.5}$$

the symmetrised wavefunction. It is related to the overlap function by a Fourier transform, as can be seen from equation 4.4:

$$F\left(\Omega, T, \omega_p\right) = \frac{1}{c\pi} \int \mathrm{d}\Delta S \;\; f\left(\Delta S, T, \omega_p\right) e^{-2i\Delta S\Omega/\mathrm{c}} \quad . \tag{4.6}$$

We obtain the overlap function $f\left(\Delta S, T, \omega_p\right)$ from the measured coincidence rate R_{coinc} by inverting equation 4.3 and using the fact that $f\left(\Delta S, T, \omega_p\right)$ is real:

$$f\left(\Delta S, T, \omega_p\right) = \left(\frac{1}{2r^2t^2}\left(t^4 + r^4 - R_{\text{coinc}}(\Delta S, T, \omega_p)\right)\right) \quad . \tag{4.7}$$

A Taylor series expansion of the wavefunction now reveals how the wavefunction can be constructed from knowledge of $F\left(\Omega, T, \omega_p\right)$ [122].

To summarise, the overlap function $f\left(\Delta S, T, \omega_p\right)$ can be obtained from the coincidence

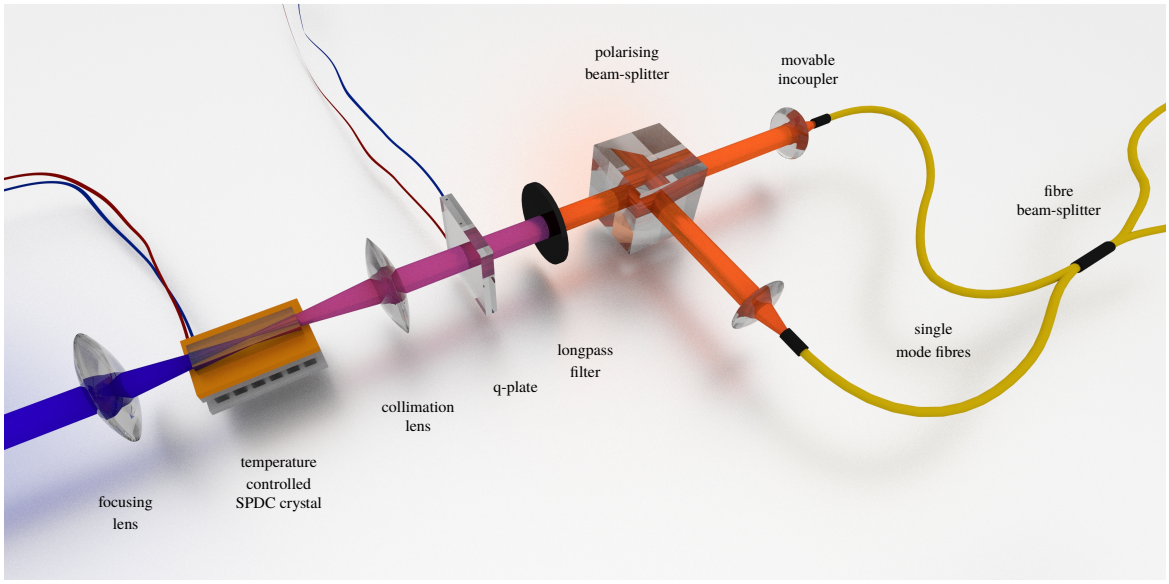

Figure 4.1: Experimental setup for the measurement of two-dimensional Hong-Ou-Mandel dips in the coincidence count rate. The two variables are the down-conversion crystal temperature, which controls the spectral shift and the position of one of the fibre in-couplers. The pump beam is focused into the SPDC crystal and the down-converted photons are collimated by another lens. For some of the measurements, a q-plate is employed to select higher order spatial modes for the in-coupling into the single mode fibres later on. A longpass filter rejects the pump beam and after that the orthogonally polarised photons of a pair are split by a polarising beam-splitter and coupled into fibres. They re-combine on a fibre-beam splitter, where the Hong-Ou-Mandel interference takes place. Coincidences are counted with fibre-coupled single photon detectors and a subsequent time to amplitude converter.

rate via elementary transformations. Then, a Fourier transform with respect to the path length difference yields the complex function $F(\Omega, T, \omega_p)$. And finally, the wave function is obtained as a slice of this complex function.

Knowledge of the full complex spectral wave function allows us to calculate the spectrum of the down-converted photons and the time delay distribution between signal and idler photons. The first is just the absolute square of the complex spectral wave function and the latter is the absolute square value of its Fourier transform.

4.3 Experimental realisation of two-dimensional Hong-Ou-Mandel measurements

The measurement data to perform an actual reconstruction of the wave function is rather straight forward to obtain. A scan in two dimensions, the path length difference and the temperature of the non-linear crystal is required, while recording the resulting coincidence rate. Figure 4.1 shows the setup used for our type II, collinear SPDC source (see section 2.2 for details on the source). After the down-converted photons have been collimated and the pump removed, signal and idler photons are separated by a polarising beam-splitter, coupled into single mode fibres and then overlapped again on a fibre beam splitter, where the Hong-Ou-Mandel interference takes place. Single photon detectors connected to a time to

amplitude converter record the number of coincidences. The temperature of the non-linear crystal is kept constant with a proportional-integral-derivative controller and the set-point can be changed by the measurement software. Fluctuations of the temperature remain within ±20 mK. The pathlength difference is changed via the distance of one of the fibre-couplers from the beam splitter. The incoupler is fixed on a motorised stage, with a precision much higher than the step width and is controlled by the measurement software as well. Because the coincidence counting system is also integrated into the software, we can perform a full two-dimensional surface scan automatically.

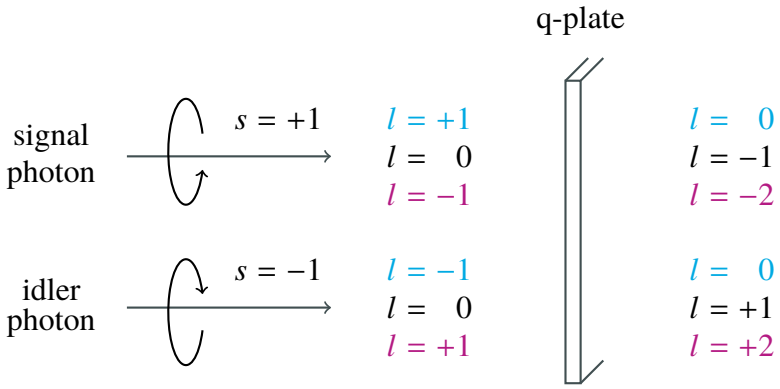

Figure 4.2: Overview of possible orbital angular momentum combinations of the SPDC pair and how they are transformed by a q-plate ($q = 0.5$). Signal and idler photons are left and right circularly polarised after a quarter wave plate. The conservation of orbital angular momentum in the down-conversion process requires the sum of signal and idler azimuthal index to be zero. The lowest three possible combinations are shown, colours indicate the affiliation with a specific pair. The q-plate adds or subtracts, depending on the polarisation, one quantum of orbital angular momentum. After the transformation only one pair is in a Gaussian state and can be coupled to a single mode fibre. All other pairs are rejected.

One experimental challenge is to change the detection mode. We use two different settings, to demonstrate the dependence of the spectral wavefunction on the detection mode. The first one is simply the Gaussian mode defined by the coupling to the single mode fibres and the second one is a mode carrying orbital angular momentum. The down-converted field usually contains contributions of higher order Laguerre-Gaussian modes [59, 123], unless the pump beam waist is specifically chosen. The wave function is in a superposition of modes

$$|\Psi\rangle = \sum_{l=-\infty}^{l=\infty} c_l \, |l\rangle_s \, |-l\rangle_i \quad , \tag{4.8}$$

where signal and idler always carry the opposite orbital angular momentum. This is due to the conservation of orbital angular momentum in SPDC [68] and the pump beam, in our case, not carrying any. Towards higher azimuthal indices the coefficients c_l vanish, due to the decreasing overlap with the pump mode [124]. We select $l = \pm 1$ Laguerre-Gaussian modes for detection, by transforming them into Gaussian states with a q-plate (see section 2.5 for an introduction) and the originally Gaussian to Laguerre-Gaussian states. See figure 4.2 for a schematic depiction. This scheme allows us to selectively detect only the part of the down-converted field carrying one quantum of orbital angular momentum with high efficiency and to keep every other aspect of the experiment the same.

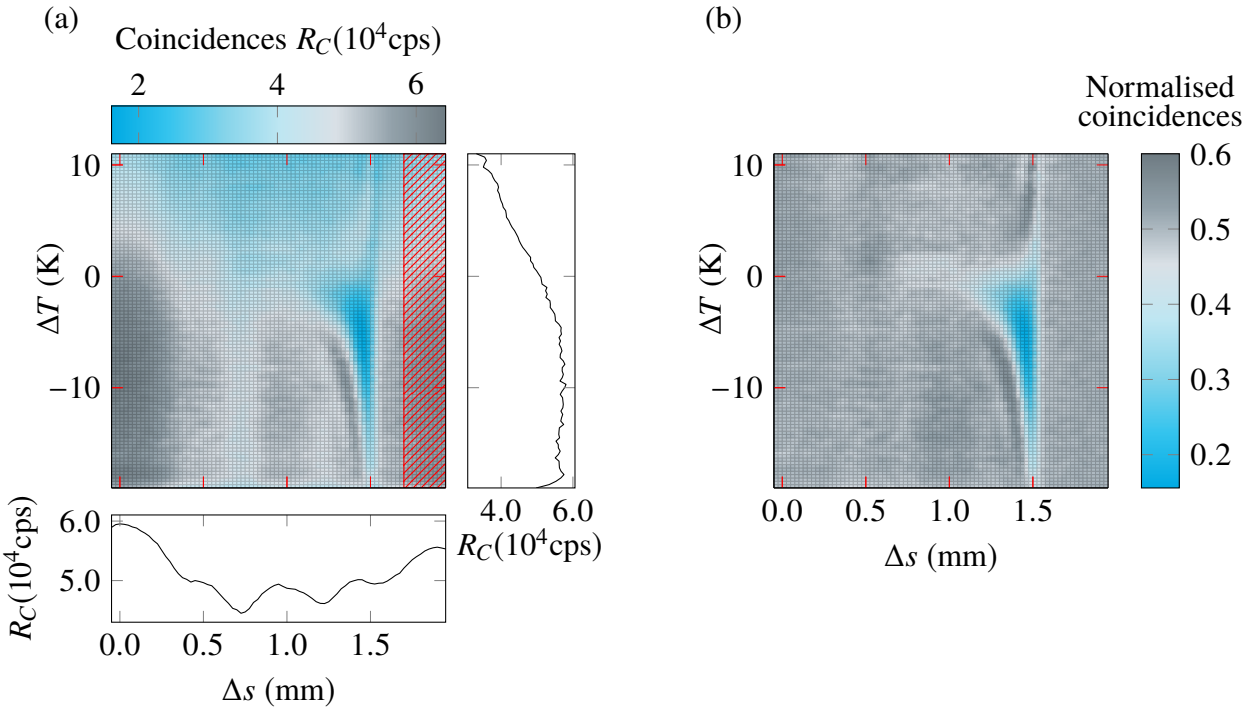

Figure 4.3: Example of a coincidence surface before (a) and after (b) correction and normalisation. The small graph below (a) shows the correction scan in the path length difference dimension, where the time delay is far offset by moving the usually fixed incoupler far enough to be outside of the interference region. The coincidence rate variation due to changes in the fibre coupling due to the movement of the incoupler can be compensated for with this scan. The graph to the right shows the average coincidence rate in the red hatched stripe, as a function of the crystal temperature. Each point in this region is also outside of the interference region and should thus – under ideal conditions – result in the same coincidence rate. Deviations must then be due to noise or drifts. Every scan at fixed temperature is normalised by the corresponding value from this graph.

Another experimental challenge is the overall stability of the measurement. The scans we present in the next section (4.4) consist of approximately 80×100 single measurement points in the pathlength and temperature directions. The measurement time for such a scan can be quite long, in our experiments, on the order of a few hours. We have identified two main instabilities that threaten the reconstruction. In figure 4.3 we use an example surface scan to illustrate the stability issues and our counter-measures. The first issue is a fluctuation of the measured coincidence rate with the displacement of the incoupler due to varying coupling efficiency. This can easily be seen in figure 4.3 (a) as a structure in the time delay direction (for example at $\Delta s \approx 0.7\,\text{mm}$) and running through the whole surface, independent of temperature. The effect is fortunately very reproducible and we correct for it with an additional scan of the incoupler at fixed temperature, but with the other incoupler displaced far enough to be outside of the dip region. This scan is shown in the lower graph of figure 4.3 (a). It reproduces the fluctuations in a regime where there is no influence on the coincidence count rate other than the varying incoupling efficiency. We use this reference to correct every path-length scan of the original data. The other contribution to instability is a slow

drift of the overall count rate with time. This is also easily discernible in figure 4.3 (a) as a continuous decrease of the coincidence count rate from the start of the measurement at low temperature to the end at high temperature. By scanning first in the pathlength dimension and then changing the crystal temperature step by step, we can correct for such a slow drift after the measurement. Again, data points outside the dip region serve as a reference, since they should all be equal. In contrast to the fluctuation in path length difference, this data is produced as part of the scan, if the scan region is wide enough. By averaging over a few of those data points, we can normalise lines of constant temperature. In the graph to the right side of figure 4.3 (a) we show these average values as a function of the temperature. Figure 4.3 (b) then shows the resulting surface after these two corrections. The Hong-Ou-Mandel dip is very well visible and nearly all structure of the surface is due to the interference.

In addition to the surface measurement as an input to the reconstruction algorithm, we also measure the spectrum directly. This allows us to compare measured and reconstructed spectra. We remove the fibre beam splitter (cf. schema 4.1) and insert a monochromator into one of the two detection arms. Counting coincidences at different wavelengths, a spectrum is acquired. To avoid drifts, we perform the spectral measurement directly after the surface scan. Even though the temporal distribution can not be accessed directly, our method provides an equivalent measurement, which we subsequently compare with theoretical predictions in the next chapter.

4.4 Measurements and reconstructions

To test our reconstruction scheme and to demonstrate the influence of outside parameters, we present three different cases that lead to distinctly different wave functions of the photon pairs. The first case is based on a standard type II down-conversion setup and Gaussian detection modes. For the second case, we choose a displaced non-linear crystal situation. This connects to the investigation of the previous chapter and allows us to study the shift of the time delay distribution directly and not only via the average time delay. As a third case, we change the detection modes from Gaussian to Laguerre-Gaussian, with a centred crystal. This drastically changes the wave function and exemplifies the possibility to shape the temporal wave function.

4.4.1 Standard conditions wavefunction

In figure 4.4 (a) we present the first two-dimensional Hong-Ou-Mandel surface measurement as a function of the path length difference and the non-linear crystal temperature. Both axes have a physically meaningful origin. The temperature is given relative to the temperature where the down-converted photons are collinear and degenerate. This is also the temperature at which the reconstructed wave function is valid. The pathlength zero corresponds to equally long interferometer arms (from the polarising beam splitter to the fibre beam splitter) for both signal and idler photons. We can determine this specific position by measuring a path-length dip as usual and one with exchanged signal and idler photons. The absolute zero position is exactly in the middle between the two resulting Hong-Ou-Mandel dips.

In the previous chapter 3 we established that the time delay distribution of the photon pair lies strictly within the interval $[0\,\mathrm{ps}, 5.3\,\mathrm{ps}]$, which corresponds to a path length difference between 0 mm and 1.6 mm. Outside of this interval, there should be no overlap between

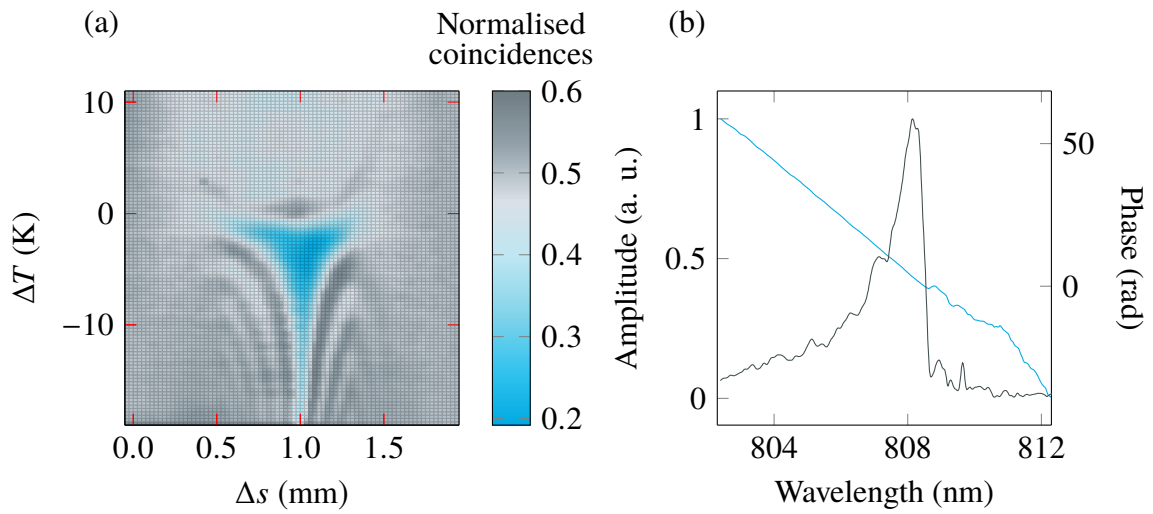

Figure 4.4: (a) Surface of the coincidence rate as a function of crystal temperature and path-length difference between the two interferometer arms. (b) Complex spectral wavefunction reconstructed from the experimental data shown in (a). The collinear degenerate temperature is 59 °C.

signal and idler whatsoever and the surface is thus completely flat. Indeed, this is what we observe in figure 4.4 (a).

Applying the reconstruction to the surface data yields the complex spectral wave function shown in figure 4.4 (b). We can use the information contained in the wave function to calculate two interesting functions: the spectrum and the time-delay distribution. We present them in figure 4.5 (a) and (b) respectively. The blue solid curves indicate the function reconstructed from the interference measurement. In figure 4.5 (a), the grey dots show a direct measurement of the spectrum using a monochromator. The resolution of the monochromator is not high enough to resolve all features and to reproduce the very steep flank, however, the agreement is very good. We compare the time delay distribution to the simulated result (grey dashed line), which is based on the experimental parameters. Examining the delay distribution very closely, we see that indeed the distribution is confined to the interval [0 ps, 5.3 ps] and zero outside of it. We also notice that the distribution is not perfectly centred within this interval, which leads us to suspect, that the crystal was actually not perfectly centred with respect to the pump focus.

4.4.2 Time delay test

For the next test of our reconstruction method, we displace the crystal away from the pump focus position. We show the resulting coincidence count surface in figure 4.6 (a). The initially symmetric dip, is now squished to one side of the interval of possible delay times, yet the overall visibility is unchanged from the symmetric case (cf. figure 4.4 (a)). The reconstructed spectrum (figure 4.6 (b)) is slightly broader, which is also found in the directly measured spectrum. The most striking difference to the previous test case is the shift of the delay time distribution to large values close to the edge of 5.3 ps (shown as vertical red line). This confirms our findings of the previous chapter. Again the agreement between the reconstructed distribution and the simulated result is excellent, underscoring the robustness of our scheme.

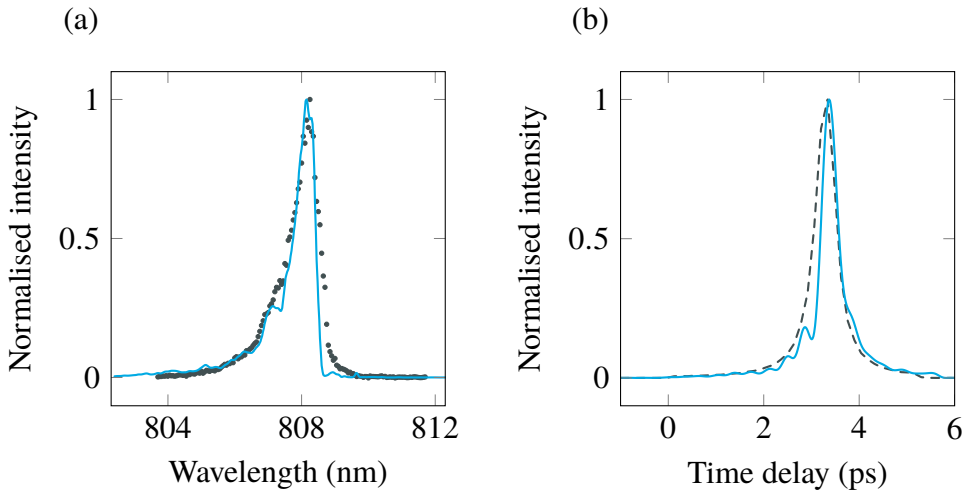

Figure 4.5: The solid blue lines show the spectrum (a) and the time delay distribution (b) calculated from the spectral wavefunction presented in figure 4.4 (b). The grey datapoints of (a) are a direct measurement of the spectrum. The grey dashed line of (b) is the simulated delay curve. The simulation results shown here and in the next two figures have been created by Nora Tischler.

Obviously, the two-dimensional scan result is not free from noise and some artifacts of varying incoupler efficiency remain. Nevertheless, the reconstructed wave function is very close to the simulated results.

4.4.3 Higher order modes

As a last test of the reconstruction scheme, but also to demonstrate the influence of the detection mode on the wave function, we present a measurement based on a Laguerre-Gaussian detection mode carrying one quantum of orbital angular momentum. See figure 4.7 (a) for the surprisingly different coincidence surface. Instead of a dip in the centre of the structure, we find a peak well above the average normalised coincidence rate of 0.5. The fact that the structure is now found at negative path length difference is due to the helicity flip imposed by the q-plate, that exchanges signal and idler. Again, we observe a very clear boundary between inside the dip region and outside (below $-1.6\,\mathrm{mm}$), where there is no overlap between signal and idler photons anymore at all.

Figure 4.7 (b) shows the reconstructed spectrum together with the directly measured one. Due to the finite resolution of the monochromator of about 1 nm we are unable to fully reproduce the intricate fine structure of the spectrum. It is however, confirmed by the simulations and a convolution of a Gaussian response function with the reconstructed spectrum (cf. figure 4.8) shows that these features are indeed not resolvable for our monochromator. The reconstructed time delay distribution shown in figure 4.7 (c) exhibits an exciting feature. Delay times corresponding to half the crystal length seem to be suppressed, in stark contrast to the distributions observed for Gaussian detection modes. The agreement between the reconstructed and the simulated distribution is less good than it was in the previous test cases, possibly due to additional noise introduced by the q-plate. However, its surprising feature is well reproduced nonetheless.

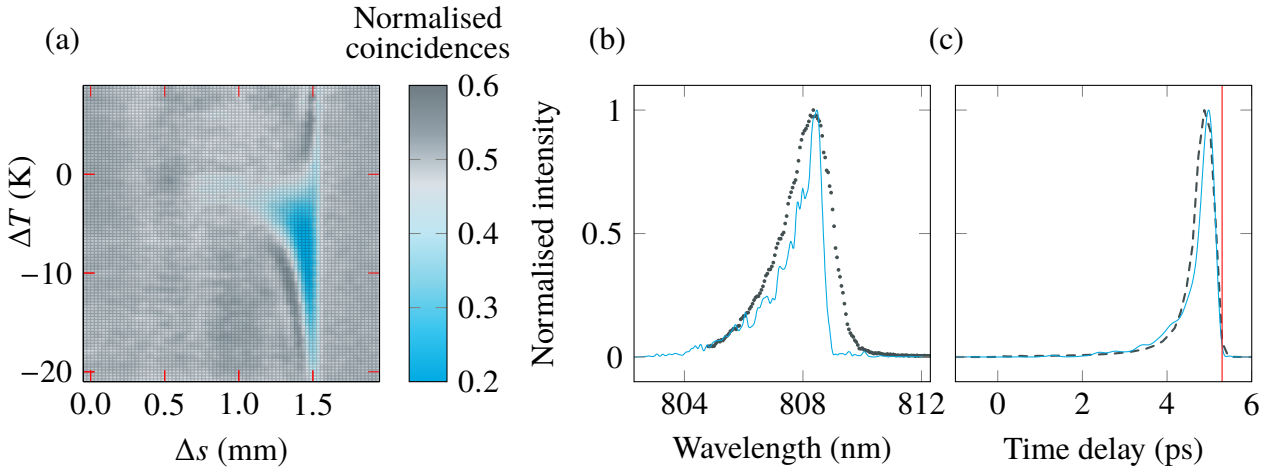

Figure 4.6: (a) Surface of the coincidence rate as a function of crystal temperature and pathlength difference between the two interferometer arms. Here the SPDC crystal is shifted by 3 mm relative to the central position shown in figure 4.4 and away from the incident pump beam. The degenerate collinear temperature is 61 °C. (b) Reconstructed spectrum (solid blue line) together with the directly measured spectrum (grey dots). (c) Reconstructed time delay distribution (solid blue line) together with the simulated distribution (grey dashed line). The vertical red line indicates the end of the delay time interval, as defined by the length of the non-linear crystal and the group velocity difference between signal and idler photons.

4.5 Discussion

We have seen in the preceding section that our reconstruction method is relatively simple, yet effective and robust. It provides a valuable access path to quantities that would be very difficult, if not impossible, to measure directly. In this last section, we discuss its limitations and possible applications.

Our method is applicable to collinear and non-collinear type II down-conversion, but not to type I SPDC since the group velocities of both photons are the same in that case. It is also important to note, that any changes made to the wave function after its creation, will not be captured correctly by the reconstruction. This again, is because the wavelength shift is crucial and it happens during the SPDC process. However, tuning the temperature of the non-linear crystal is not the only way to displace the spectra of signal and idler photons. The same scheme can also be based on scanning the pump frequency instead of the crystal temperature, which has exactly the same effect.

We have seen in the results that the reconstruction reveals features otherwise unobservable. And that is true both for the spectrum, where a direct measurement is limited by a finite resolution of any spectrometer, as well as for the time delay distribution, which would entirely be unobservable with the time resolution of current single photon detectors. But, not only does our method allow insights into the wave function, we can also use it to manipulate aspects of the wave function in a targeted fashion. This becomes most apparent with the Laguerre-Gaussian detection mode and its impact on the time delay distribution. The specific shape of the distribution could for example be used to create time bin entangled photon pairs [125], by shifting the middle dip to zero delay. This would lead to a state of

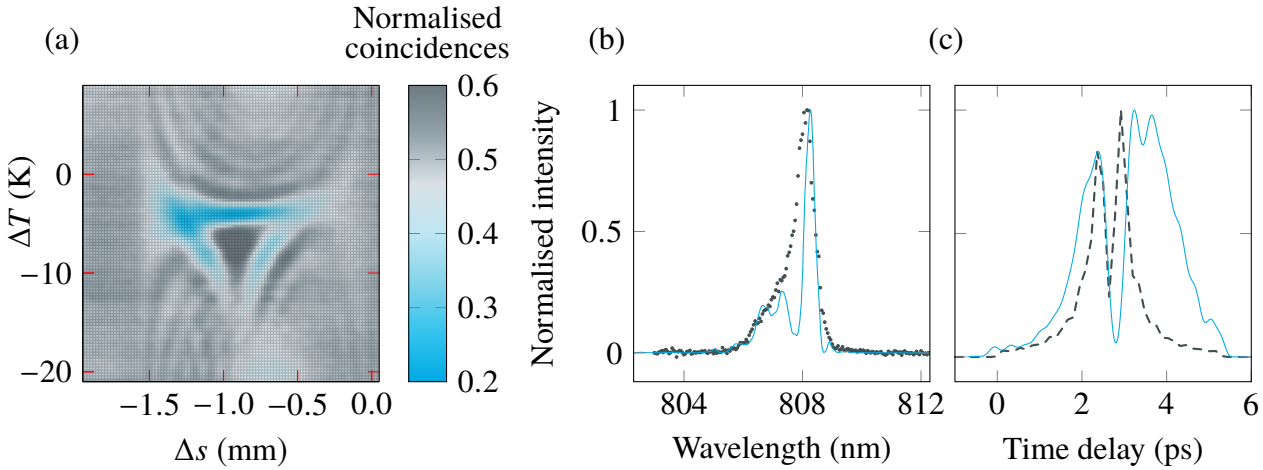

Figure 4.7: (a) Surface of the coincidence rate as a function of crystal temperature and pathlength difference between the two interferometer arms. Here, with a centred SPDC crystal again, but selecting photons carrying one quantum of orbital angular momentum. The degenerate collinear temperature is 58.7 °C. (b) Reconstructed spectrum (solid blue line) together with the directly measured spectrum (grey dots). (c) Reconstructed time delay distribution (solid blue line) together with the simulated distribution (grey dashed line).

the form $|\phi\rangle = \frac{1}{\sqrt{2}}\left(|\tau\rangle_1 |-\tau\rangle_2 + e^{i\phi} |-\tau\rangle_1 |\tau\rangle_2\right)$ with a negligible contribution of time shift τ terms close to zero. Such states are an active area of research [126] and can be used to efficiently distribute entanglement through photonic fibre networks [127].

It would be very interesting – as an extension of our work – to study other exotic detection modes, but also to investigate the influence of different spatial pump modes on the spectral wave function and especially the time delay distribution.

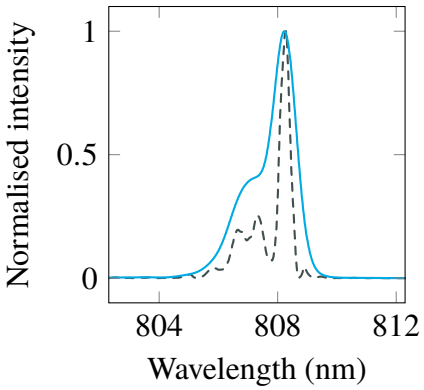

Figure 4.8: Convolution (solid blue curve) of an estimated response function of the monochromator with the reconstructed spectrum (grey dashed curve). We assume a Gaussian response function with a full width at half maximum of 1 nm.

5

Two-Photon Interactions with Nanoapertures

In the previous chapters, we have presented tools and techniques to control two-photon quantum states in many of their degrees of freedom. We now want to put these to use, in an attempt to create a tailored state that interacts in a surprising and non-trivial way with a plasmonic nano-structure. The structure is a sub-wavelength aperture in a thin gold film, which is known to lead to a helicity flip for some of the transmitted photons (see section 2.6). This helicity flip alters the state of transmitted photons or photon pairs. However, we show that by using a two-photon state, specifically engineered for this interaction, the state can be protected. The reason for this can be understood from the perspective of quantum interference which leads to destructive interference of the changed amplitudes. It can also be understood from a symmetry argument that takes into account the rotational and mirror symmetries of the nanoaperture and the two-photon state.

The impact of this demonstration we believe, is two-fold. First, the control over the quantum photonic state and its interaction with a structure smaller than the wavelength of light, is a big step in bringing quantum information technologies and nano-photonics together. Secondly, we believe that our scheme shows that entanglement can be protected from decoherence by taking into account the underlying symmetries and peculiarities of the environment.

We start this chapter with an overview over other entanglement protection approaches and possible connections to nano-photonics in section 5.1. In the next section 5.2 we introduce the theoretical framework behind the idea for the entanglement protection. Interestingly, the same principle can be deduced from a symmetry argument, which we explain in section 5.3. We then turn our focus to the experimental realisation of the system and the resulting measurements in section 5.4. This section is split into several parts that discuss two different detection schemes and the corresponding measurements, showing quantum interference and entanglement protection. We conclude the chapter with a summary and outlook in section 5.5.

5.1 Entanglement protection and nano-photonics

In section 1.1.2 of the introduction, we have discussed a number of quantum technologies, like quantum computing, communication or metrology. All of them rely on quantum states – in whatever physical system they may exist – and on the ability to maintain these states for some time. Unfortunately, everything tends to interact with its surrounding environment and so do quantum states. This interaction with the environment usually destroys coherence and entanglement, which are essential for the correct functioning of many quantum protocols. Tremendous efforts have been made to find ways to stabilise and protect these states or to detect and correct errors at a later time.

The loss of coherence is directly tackled with approaches like weak measurement reversal [128], decoherence free sub-spaces [129–131], dynamical decoupling [132, 133] or using the quantum Zeno effect to suppress unwanted evolution [134]. Other schemes try to undo damage afterwards, like error correction codes [15, 135–137] or entanglement distillation [138–141]. We wish to extend this work on the protection of quantum entanglement and coherence towards the nano-photonic regime, where light interacts with plasmonic structures at length scales smaller than the wavelength of light. Using photonic qubits in conjunction with plasmonic devices promises hybrid systems [142, 143].

It has been shown that plasmons retain many quantum mechanical properties of photons like single photon statistics [144, 145], wave-particle duality [146] and the ability of two-particle interference [47, 147]. Furthermore, it is possible to use plasmons as an intermediary mode between two photon states, without losing indistinguishability [148] or entanglement [149, 150].

In the following sections we introduce a novel scheme to protect the entanglement of a specifically engineered two-photon state from degradation due to interaction with a plasmonic nanoaperture. Any light sent through this sub-wavelength aperture, strongly interacts with it. Yet, one specific state is protected, even though it is only distinguished by a phase from a state which completely degrades. Previous work by Altewischer and coworkers [149] has shown that photons undergoing a transformation into plasmons and back can remain entangled with their partner. They created pairs of entangled photons, inserted arrays of sub-wavelength apertures into one or both paths and observed good interference visibilities in all cases, except when focusing the beam. In contrast to their work, we subject the whole entangled two-photon state to one interaction, that leads to strong decoherence on any arbitrary state, except the one specifically engineered. We have thus created an entangled state that remains unperturbed by a strong light-matter interaction and protected its entanglement. We believe this to be a first step towards quantum technologies in the nano-photonic regime.

5.2 Quantum interference argument, explaining the entanglement protection

Before introducing our nano structure and the special photonic state, we will look into a well known system that exhibits state protection of spatial modes. A standard non-polarising beam splitter, as shown in figure 5.1 (a) with its in- and output modes, serves as the centre for this model. Instead of sending one photon into each input of the beam splitter, as for the Hong-Ou-Mandel effect (see section 2.3 for a detailed introduction), one can think about an

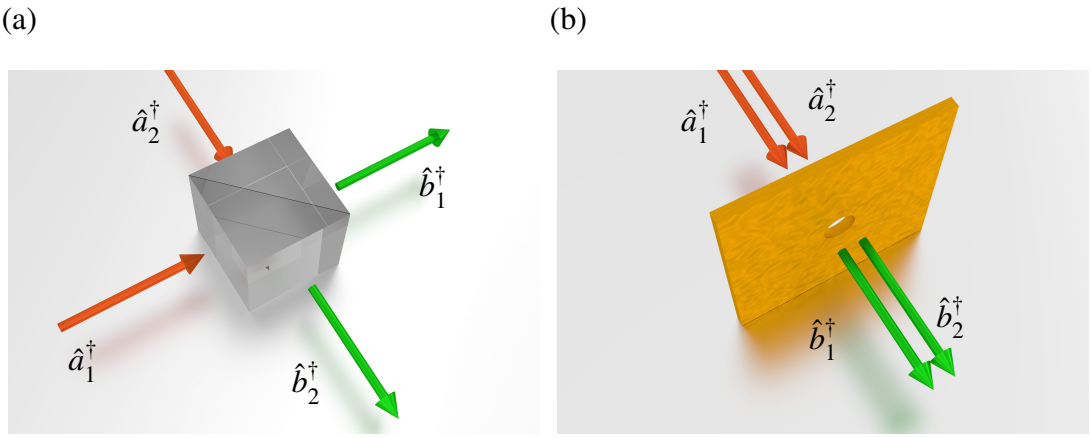

Figure 5.1: (a) Schematic of the input and output modes of a standard beam splitter, used for a Hong-Ou-Mandel type interference experiment. (b) In comparison a nanoaperture with two input and two output helicity modes. Although creation operators in the sub-figures bear the same symbol, they refer to different states. The photons in (a) are indistinguishable in all degrees of freedom except space and in subfigure (b) the photons are indistinguishable in all degrees of freedom except helicity.

input state that is already path entangled. Exploiting the single photon transformations:

$$\hat{a}_1^\dagger \longrightarrow \frac{1}{\sqrt{2}}\left(\hat{b}_1^\dagger + \hat{b}_2^\dagger\right) \tag{5.1}$$

$$\hat{a}_2^\dagger \longrightarrow \frac{1}{\sqrt{2}}\left(\hat{b}_1^\dagger - \hat{b}_2^\dagger\right) \tag{5.2}$$

we see that the specific input state

$$\frac{1}{2}\left(\hat{a}_1^\dagger\hat{a}_1^\dagger + \hat{a}_2^\dagger\hat{a}_2^\dagger\right) \longrightarrow \frac{1}{2}\left(\hat{b}_1^\dagger\hat{b}_1^\dagger + \hat{b}_2^\dagger\hat{b}_2^\dagger\right) \quad , \tag{5.3}$$

is protected by the interaction with the beam splitter. We thus have a model system where a specific path entangled state is preserved under the interaction with a system that usually alters the state of arbitrary two-photon inputs. For example the input state $\hat{a}_1^\dagger\hat{a}_1^\dagger - \hat{a}_2^\dagger\hat{a}_2^\dagger$ leads to the output $\left(\hat{b}_1^\dagger\hat{b}_2^\dagger\right)$.

In a similar manner that a beam-splitter creates a superposition between the two output modes, a plasmonic nanoaperture acts on the helicity of a transmitted photon. We schematically show the configuration in figure 5.1 (b). Section 2.6 gives a detailed introduction to plasmonic nanoapertures and their helicity flip behaviour. For a single photon $\hat{a}_{m,\Lambda}^\dagger$ with total angular momentum m and helicity Λ, the nanoaperture transforms the state in the following way:

$$\hat{a}_{m,\Lambda}^\dagger \longrightarrow \alpha\hat{b}_{m,\Lambda}^\dagger + \beta\hat{b}_{m,-\Lambda}^\dagger \quad . \tag{5.4}$$

The probability for a flip of the helicity when passing through the nanoaperture depends on the relative strengths of the coefficients α and β, which are constrained by generalised

beam splitter relations [151] and can only be obtained from simulation or experiment for our nanoaperture. Note that the total angular momentum is conserved, since the whole system is cylindrically symmetric. This conservation requires a change in the orbital angular momentum, if the helicity is flipped. The nanoaperture thus mixes two output channels, similarly to the beam splitter with the distinction that the channels are in polarisation and not spatial.

The fundamental idea now is to coherently add the amplitudes of the helicity output modes from both photons. This of course is only possible, if the two output modes are the same for both input photons. If working with Gaussian input states (no orbital angular momentum), the output modes differ because the two input photons and with them necessarily (due to the conservation of total angular momentum) also their output modes live in separate total angular momentum sub-spaces:

$$\hat{a}^\dagger_{-1,-} \longrightarrow \alpha \hat{b}^\dagger_{-1,-} + \beta \hat{b}^\dagger_{-1,+} \tag{5.5}$$

$$\hat{a}^\dagger_{1,+} \longrightarrow \alpha \hat{b}^\dagger_{1,+} + \beta \hat{b}^\dagger_{1,-} \quad . \tag{5.6}$$

This can only be overcome by using input photons with the same total angular momentum. One trivial possibility is to make the two input photons exactly equal, but this does not lead to interesting results. We thus combine two photons with total angular momentum zero, but opposing helicity. The transformations then read:

$$\hat{a}^\dagger_{0,+} \longrightarrow \alpha \hat{b}^\dagger_{0,+} + \beta \hat{b}^\dagger_{0,-} \tag{5.7}$$

$$\hat{a}^\dagger_{0,-} \longrightarrow \alpha \hat{b}^\dagger_{0,-} + \beta \hat{b}^\dagger_{0,+} \quad , \tag{5.8}$$

or in matrix form:

$$\begin{pmatrix} \hat{a}^\dagger_{0,+} \\ \hat{a}^\dagger_{0,-} \end{pmatrix} \longrightarrow \begin{pmatrix} \alpha & \beta \\ \beta & \alpha \end{pmatrix} \begin{pmatrix} \hat{b}^\dagger_{0,+} \\ \hat{b}^\dagger_{0,-} \end{pmatrix} \quad . \tag{5.9}$$

Now, all possible output modes lie within the same sub-space of total angular momentum zero and will thus add coherently.

Under these constraints, there is exactly one specific state which is protected from degradation in the interaction with the nanoaperture:

$$|\Psi_-\rangle = \frac{1}{2}\left(\hat{a}^{\dagger 2}_{0,+} - \hat{a}^{\dagger 2}_{0,-}\right)|0\rangle \quad . \tag{5.10}$$

Subjecting this state to the transformations due to the aperture, we find the following output state:

$$|\Psi_-\rangle \longrightarrow \frac{1}{2}\left(\alpha^2 - \beta^2\right)\left(\hat{b}^{\dagger 2}_{0,+} - \hat{b}^{\dagger 2}_{0,-}\right)|0\rangle \quad , \tag{5.11}$$

which, apart from the normalisation, is nothing else than the input state itself. The case $\alpha^2 = \beta^2$ is impossible here, because of requirements of the generalised beam splitter relations [151]. If, however, we change the phase between the two contributions of the state (equation (5.10)) from a minus to a plus sign $|\Psi_+\rangle = \hat{a}^\dagger_{0,+}\hat{a}^\dagger_{0,+} + \hat{a}^\dagger_{0,-}\hat{a}^\dagger_{0,-}$, we are left with the following output:

$$|\Psi_+\rangle \longrightarrow \frac{1}{2}\left(\alpha^2 + \beta^2\right)\left(\hat{b}^{\dagger 2}_{0,+} + \hat{b}^{\dagger 2}_{0,-}\right)|0\rangle + 2\alpha\beta\hat{b}^\dagger_{0,+}\hat{b}^\dagger_{0,-}|0\rangle \quad , \tag{5.12}$$

where due to the helicity flip probability we find an additional term that was not part of the initial state. In the following we will call the first state, the *minus state* and the second

one the *plus state*. Of course the transformation due to the nanoaperture is non-unitary, because of losses by reflection or absorption. This means that additional to the two photon output states considered here, there will be cases where only one photon or maybe even no photon of a pair is transmitted through the aperture. We are, however, only interested in the behaviour of the two-photon states and thus post-select on photon pairs in the detection.

We have now gathered all ingredients to let two photons interfere, with the help of a plasmonic nanoaperture in a way very similar to the famous Hong, Ou and Mandel interference experiment on a beam-splitter. This quantum interference provides the protection of the specific input state from the interaction with the nano-structure.

5.3 Symmetry argument explaining the entanglement protection

Instead of thinking about quantum interference as the reason for the state protection, we can also make a symmetry argument that leads to the same prediction. The nanoaperture is rotationally symmetric and will thus preserve (among other quantities) any mirror symmetry of the centred and also rotationally symmetric incident beam. Within the sub-space of two-photon states, where both photons carry no total angular momentum, there are three states possible with well defined spin and orbital angular momentum and all other degrees of freedom assumed to be identical for both photons. These three states are:

$$|\Psi_0\rangle = \hat{a}^\dagger_{0,+}\hat{a}^\dagger_{0,-}|0\rangle \tag{5.13}$$

$$|\Psi_+\rangle = \frac{1}{\sqrt{2}}\left(\hat{a}^\dagger_{0,+}\hat{a}^\dagger_{0,+} + \hat{a}^\dagger_{0,-}\hat{a}^\dagger_{0,-}\right)|0\rangle \tag{5.14}$$

$$|\Psi_-\rangle = \frac{1}{\sqrt{2}}\left(\hat{a}^\dagger_{0,+}\hat{a}^\dagger_{0,+} - \hat{a}^\dagger_{0,-}\hat{a}^\dagger_{0,-}\right)|0\rangle \quad . \tag{5.15}$$

States $|\Psi_0\rangle$ and $|\Psi_+\rangle$ are mirror symmetric relative to any mirror plane containing the beam axis, because a mirror operation only inverts the helicity and thus leaves the first two states untouched. The third state $|\Psi_-\rangle$ on the contrary acquires a minus sign under mirror inversion and is thus mirror anti-symmetric. Coming back to the observation that the aperture must preserve mirror symmetry, it becomes clear that it can only transform $|\Psi_0\rangle$ into $|\Psi_+\rangle$ and vice versa, but the $|\Psi_-\rangle$ is protected. Looking again at the transformation of these three states obtained from the single photon transformations, we see:

$$|\Psi_0\rangle = \hat{a}^\dagger_{0,+}\hat{a}^\dagger_{0,-}|0\rangle \longrightarrow \left(\alpha^2+\beta^2\right)\hat{b}^\dagger_{0,+}\hat{b}^\dagger_{0,-}|0\rangle + \alpha\beta\left(\hat{b}^{\dagger 2}_{0,+} + \hat{b}^{\dagger 2}_{0,-}\right)|0\rangle \tag{5.16}$$

$$|\Psi_+\rangle = \frac{1}{\sqrt{2}}\left(\hat{a}^{\dagger 2}_{0,+} + \hat{a}^{\dagger 2}_{0,-}\right)|0\rangle \longrightarrow \left(\alpha^2+\beta^2\right)\left(\hat{b}^{\dagger 2}_{0,+} + \hat{b}^{\dagger 2}_{0,-}\right)|0\rangle + 4\alpha\beta\hat{b}^\dagger_{0,+}\hat{b}^\dagger_{0,-}|0\rangle \tag{5.17}$$

$$|\Psi_-\rangle = \frac{1}{\sqrt{2}}\left(\hat{a}^{\dagger 2}_{0,+} - \hat{a}^{\dagger 2}_{0,-}\right)|0\rangle \longrightarrow \left(\alpha^2-\beta^2\right)\left(\hat{b}^{\dagger 2}_{0,+} - \hat{b}^{\dagger 2}_{0,-}\right)|0\rangle \quad . \tag{5.18}$$

Both initially pure mirror symmetric states evolve into superpositions of themselves, while the mirror anti-symmetric state is preserved. Only the minus state is protected from degradation. Every other two-photon state in the total angular momentum zero sub-space conceivable from these three basis states will undergo a transformation due the interaction with the

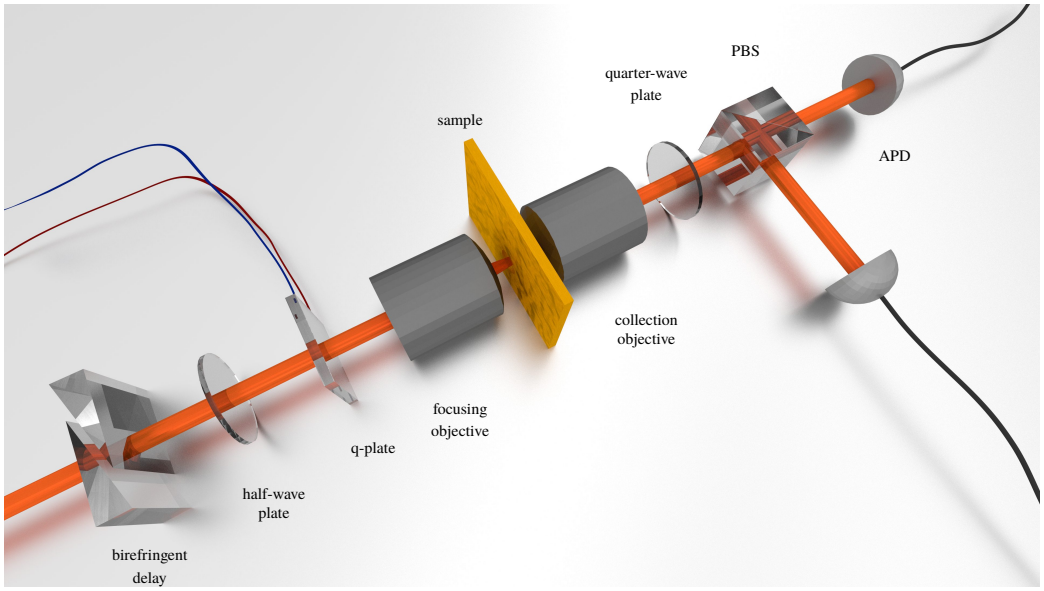

Figure 5.2: Schematic of the experimental setup for transmission of protected quantum states through the nanoaperture. Starting from the left, the beam of orthogonally polarised photons passes through a birefringent delay line, a half-wave plate and a q-plate, which finishes the state preparation. The beam is then focused onto the aperture and re-collimated afterwards. A quarter-wave plate and a polarising beam-splitter project the output state onto the circularly polarised basis, in which coincidences are detected with single photon detectors.

nanoaperture. An arbitrary two-photon state can be expressed as a linear combination of the three basis states. The interaction with the nanoaperture leads to the transformations of all terms of the state by equations 5.16 to 5.18 and any contribution of $|\Psi_0\rangle$ or $|\Psi_+\rangle$ in the initial state will lead to a modified output state.

5.4 Experimental realisation and measurement results

We will now describe the experiment realising the scheme described in the preceding sections. After discussing the details of the state preparation in section 5.4.1, we first focus on the confirmation of quantum interference. We introduce a measurement scheme based on direct correlation measurements in the helicity channels in section 5.4.2 . In section 5.4.3 we present and discuss the measurement results of this setup. We argue that these measurements and the detection setup in this form are not sufficient to prove that entanglement is protected through the interaction. We tackle that in the following section 5.4.4, where we introduce a tomography based measurement scheme, which is more difficult to implement, but allows to reconstruct the full two-photon polarisation state. In section 5.4.5 we present and discuss the results of these measurements, showing entanglement protection.

5.4.1 State preparation

Starting from the same collinear, type II, spontaneous parametric down-conversion source used throughout this thesis, we have two photons with orthogonal linear polarisations available. Since we are interested in a certain spatial mode, we couple both photons into the

same single mode fibre. After the fibre we are then left with pure Gaussian states and to counter any perturbation of the polarisation state due to the fibre, we employ a set of wave plates. Figure 5.2 gives an overview over the experimental apparatus following after the fibre out-coupling. The polarisation part of the minus state appears naturally, when changing the basis to circular polarisation (R for right and L for left circularly polarised), using the identities $|H\rangle = \frac{1}{\sqrt{2}}\left(|R\rangle + |L\rangle\right)$ and $|V\rangle = \frac{1}{i\sqrt{2}}\left(|R\rangle - |L\rangle\right)$

$$|\psi_-\rangle = |H\rangle\,|V\rangle = \frac{1}{2i}\left(|R\rangle\,|R\rangle - |L\rangle\,|L\rangle\right) \quad . \tag{5.19}$$

Very important here is the fact that this equality is only correct, if both photons are indistinguishable in all other degrees of freedom. This is why we use a delay line on the linearly polarised photons to adjust the time delay between the two photons. Control over the spectral overlap is achieved, as in the previous chapters, by temperature tuning the down-conversion crystal. If for any reason the photons are not indistinguishable, the state will have the following form

$$|\psi_{dist}\rangle = |H\rangle\,|V'\rangle = \frac{1}{2i}\left(|R\rangle\,|R'\rangle - |R\rangle\,|L'\rangle + |L\rangle\,|R'\rangle - |L\rangle\,|L'\rangle\right) \quad . \tag{5.20}$$

where we have indicated distinguishable states by a dash. Also for the plus state both photons need to be indistinguishable. It can then be created by simply rotating the initial linear polarisation by 45° with a half-wave plate into the diagonal(D)/anti-diagonal(A) basis.

$$|\psi_+\rangle = |A\rangle\,|D\rangle = \frac{1}{2}\left(|R\rangle\,|R\rangle + |L\rangle\,|L\rangle\right) \quad . \tag{5.21}$$

The second step in the state preparation is the change to zero total angular momentum. Up to now both photons are in a Gaussian spatial mode with total angular momentum 1 or −1. As detailed in section 2.5, a variety of tools exist to change the orbital angular momentum of light. Best suited for our case is again the q-plate, because it can transfer both photons into total angular momentum zero at the same time. Depending on the incident circular polarisation, one quantum of orbital angular momentum is either added or subtracted.

The state is now ready to be focused tightly onto the nanoaperture. See appendix C for details on the sample and its positioning. After the aperture a second objective collects and collimates the transmitted light, which is then analysed.

5.4.2 Quantum interference detection scheme

This first detection scheme, is based on counting coincidences between the two circular polarisation channels. The combination of quarter-wave plate and polarising beam splitter after the collection objective (see figure 5.2) splits the beam into right and left circularly polarised contributions. Both input states feature a perfect correlation in the helicity channels. Meaning, that without the interaction with an aperture, both states - if prepared optimally - will lead to perfect bunching. Both photons of a pair will either be transmitted or reflected by the polarising beam splitter. By counting coincidence events with single photon detectors in each arm, we detect this bunching as the absence of events. As a reference, we use the coincidence rate when the two photons are delayed with respect to each other and thus the plus or minus states (equations (5.19) and (5.21)) are not created. The state actually created when the two photons are distinguishable (see equation (5.20)) results in a random distribution

of photons in both detection channels and thus gives a reference coincidence count rate. Technical details on the coincidence counting can be found in appendix A.

From our calculations in the previous section, we know that the minus state should be able to maintain its correlation even through the interaction with the nanoaperture, whereas the plus state should be degraded. We can thus, detect the quantum interference and the state protection by observing how the correlations between the two helicity channels behave when the aperture is present.

5.4.3 Measurements demonstrating quantum interference

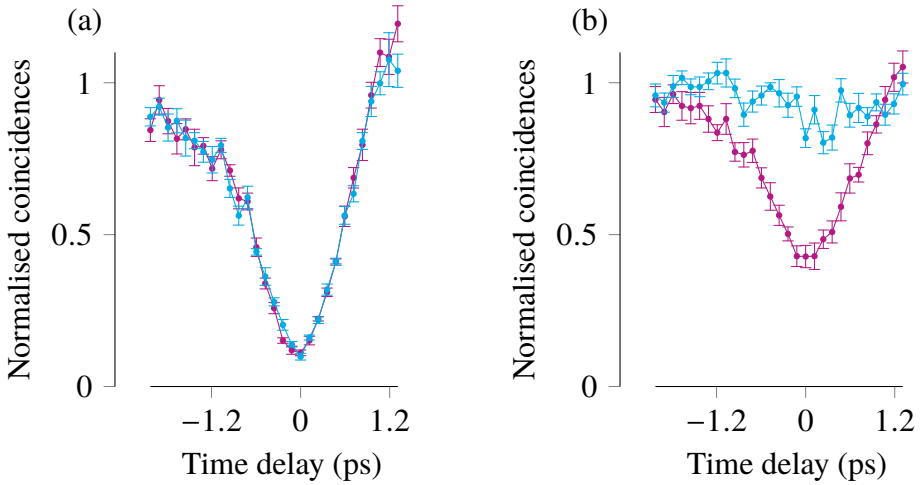

Figure 5.3: Normalised coincidence count rates for plus (blue) and minus (purple) states as a function of the time delay between the two photons. (a) Without going through the nanoaperture and (b) after transmission through the nanoaperture. At every time delay the coincidence rate has been measured ten times and the error bars show one standard deviation of the resulting distribution.

The observation of coincidence rate differences between plus and minus states is a straight forward way of demonstrating the behaviour of the state under the interaction with the nanoaperture. As discussed in the previous section 5.4.2, in the absence of the nanoaperture, both the plus and the minus state are expected to show perfect bunching in the helicity detection channels. In figure 5.3 (a) we show the behaviour of the coincidence rate of both states as a function of the time delay between the two photons when no aperture is present. To be precise, the input states are actually only equal (modulo experimental imperfections) to plus and minus states for non-zero time delays (c.f. section 5.4.1). For increasing time delays the input states become more and more mixed, until – far outside of the dip – bunching and anti-bunching in the detection channels are equally likely. As expected, figure 5.3 (a) shows strong bunching at zero time delay, indicating a high state fidelity and excellent agreement between plus and minus states.

Sending the two-photon states now through the nanoaperture, dramatically changes the picture, see figure 5.3 (b). Because of the strong interaction with the aperture, the plus state has degraded completely into a mixed state not showing any appreciable bunching anymore. The minus state, however, has largely been protected from this degradation as predicted (cf.

section 5.2). We attribute, the reduction of the bunching as compared to the case without the sample, to an imperfect initialisation of the phase, which mixes plus and minus states slightly.

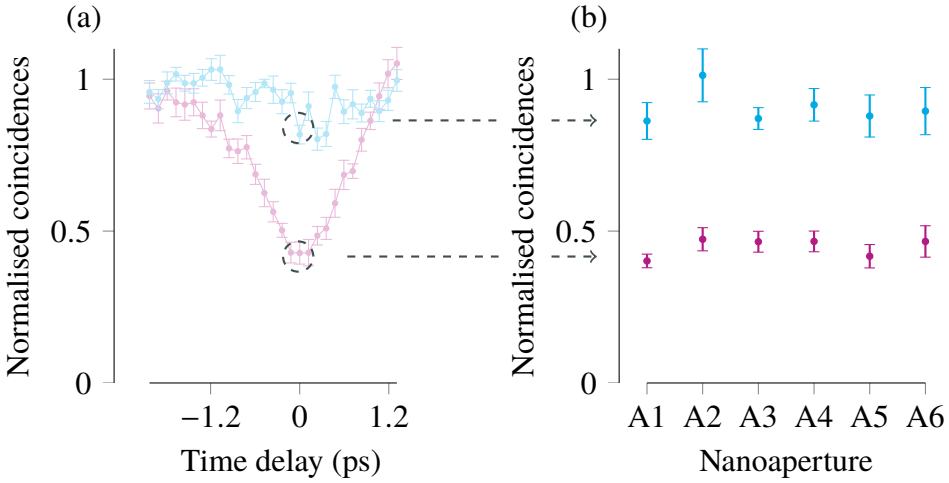

Figure 5.4: (a) Coincidence rates for plus (blue) and minus (purple) states as a function of the time delay between the two photons after transmission through a nanoaperture. (b) Coincidence rates for a number of different apertures with nominally the same diameter. The coincidence rates have been measured at zero time delay. Every single coincidence rate has been measured ten times and the error bars show one standard deviation of the resulting distribution.

We now want to demonstrate that the observed behaviour is not unique to a specific nanoaperture and robust against fabrication imperfections. In figure 5.4 (b) we show the difference between plus and minus states for a number of individual nanoapertures. It is sufficient to compare the coincidence rates for zero time delay, as only there the photons are as indistinguishable as possible and thus the states optimally prepared. We observe a very consistent spread between the degraded plus state and the protected minus state over all six individual nanoapertures, which have been fabricated with nominally the same diameter. For details on the sample fabrication, see appendix C.

In section 5.2, we have discussed, why the quantum interference and thus the state protection is only possible for states with zero total angular momentum. In figure 5.5 (a) we show that the degradation of Gaussian states (with total angular momentum 1 and -1) through increasingly smaller nanoapertures is directly correlated to the single photon helicity flip ratio (figure 5.5 (b)). This helicity flip ratio for single photons quantifies the ratio of photons with an inverted helicity after the aperture to photons with unchanged helicity. It is much larger for photons carrying orbital angular momentum than for Gaussian states [95]. This is why we need much smaller holes for the Gaussian input state to observe a degradation of the state. All previous measurements with total angular momentum zero states used a 750 nm aperture, which resulted in a flip ratio of about 0.80 ± 0.03.

Even though the flip ratio for the Gaussian states reaches only 0.06 for the smallest aperture, we observe a steady degradation of the transmitted state towards smaller apertures. As expected, plus and minus states behave identically, with both of them being degraded equally for increasing flip ratio.

The offset in the coincidence rates (cf. figure 5.5 (a)) is due to imperfect indistinguishability, as already seen in figure 5.3 for the states carrying orbital angular momentum. Two main

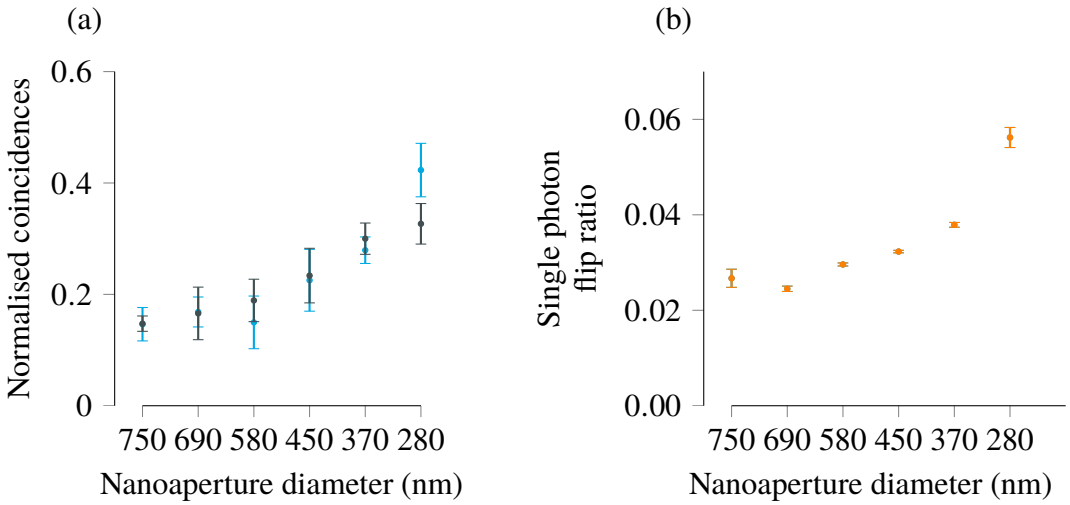

Figure 5.5: Decrease of the visibility of Gaussian plus and minus states with increasingly smaller nanoapertures. The coincidence rates (a) are correlated to the increase of the single photon flip ratios (b). In contrast to the states with zero total angular momentum, here, both states experience the same degradation.

factors contribute to a remaining distinguishability even at well compensated time delay. The first is non-ideal polarisation, both of the input state and of the detection beam-splitter. This leads to cross-talk between the two detection channels and eventually to a finite coincidence rate, where ideally there should be none. The second factor is an imperfect frequency overlap of signal and idler photons.

The offset of the single photon flip ratio (cf. figure 5.5 (b)) as well is an artefact and not expected in an ideal system, since the flip ratio must vanish in the limit of holes much larger than the wavelength. It can also be attributed to non-ideal preparation and separation of the polarisation.

5.4.4 Entanglement detection scheme

So far, we have shown that minus and plus states behave very differently when interacting with the nanoaperture. However, we have only looked at their correlations in the helicity channel. A definite statement about the protection of the state and the contained entanglement is not yet possible. The correlations that were preserved for the minus state may be purely classical. We will now look at tomography measurements that complement the picture gained from the coincidence rate measurements, to show that the entanglement is indeed protected.

To achieve this, we use quantum state tomography [152] of the polarisation state. The idea being that once we know the full polarisation state, we can calculate the entanglement inherent in it. However, this is complicated by the fact, that the two photons become entangled in polarisation and orbital angular momentum after passing through the q-plate. As long as the polarisation plus or minus states (see equations 5.19 and 5.21) have not undergone the q-plate transformation, they are entangled only in polarisation. Once the q-plate adds one quantum of orbital angular momentum to the left circularly polarised parts and subtracts one from the right circularly polarised ones, the state is entangled simultaneously in polarisation and orbital angular momentum. This is an issue for the detection of entanglement, since we are only efficiently capable of measuring the polarisation state, but not the orbital angular

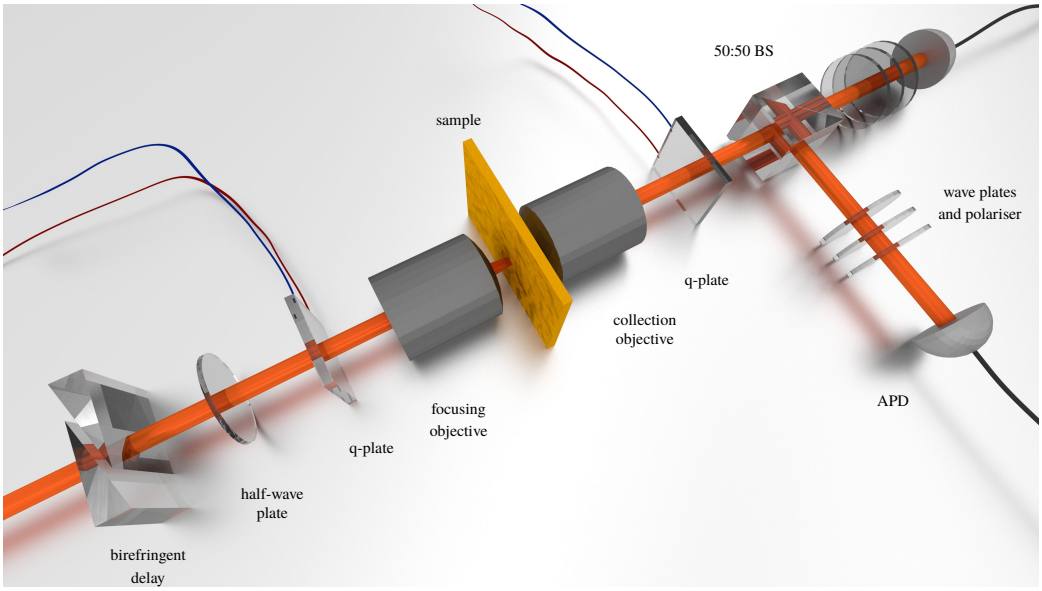

Figure 5.6: Variation of the initial experimental setup (cf. figure 5.2) for quantum state tomography measurements. After the transmission through the nanoaperture, a second q-plate reverses the transformation of the first one, removing the additional entanglement in orbital angular momentum. After that a 50:50 beam-splitter separates the two photons and a set of waveplates and linear polarisers allows correlation measurements in arbitrary polarisation bases.

momentum part. So measuring the state in the polarisation bases only, traces out the orbital angular momentum degree of freedom, which prevents the polarisation entanglement to manifest itself in the reconstructed density matrix. We have to reverse the transformation of the q-plate first, before we can perform the state tomography. We achieve this by using a second identical q-plate after the photon pair has interacted with the nanoaperture. See figure 5.6 for a schematic of the modified setup. Now after the second q-plate, the state is again only entangled in polarisation and we can perform the state tomography by splitting the two photons stochastically. We measure all 36 combinations of the six basis states, horizontal, vertical, diagonal and anti-diagonal linear polarisation as well as, right and left circular polarisation with a set of wave-plates and a polariser in each detection arm. 16 single measurements would be enough, but more measurements make the scheme more robust. Employing a maximum likelihood algorithm for the density matrix reconstruction [152], we gain knowledge of the full polarisation state and are able to subsequently calculate different entanglement measures.

5.4.5 Measurements demonstrating entanglement protection

In section 5.4.3 we have shown that the minus state experiences quantum interference and shown indications that this protects the incident state from degradation that any other two photon state is subject to. We now present polarisation state tomographies proving that the state and its entanglement are indeed preserved through the interaction with the aperture. The measurement is difficult due to the simultaneous use of two q-plates as described in the previous section. Ideally, the second q-plate would fully reverse the transformation of the first

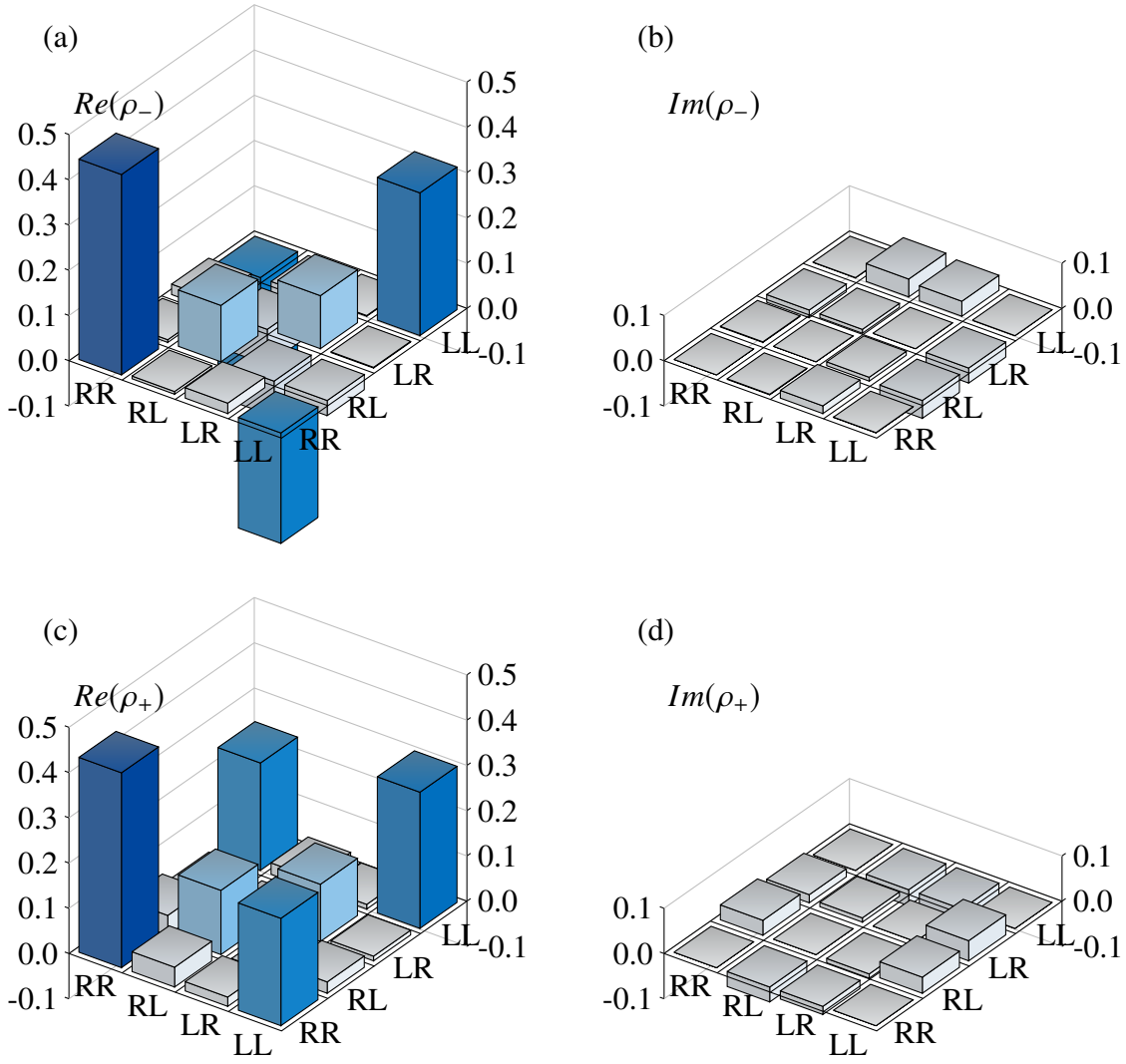

Figure 5.7: Reconstructed density matrices ((a,c) real parts and (b,d) imaginary parts) of the incident Laguerre-Gaussian minus (a,b) and plus (c,d) states. The element $|LL\rangle$-$|RR\rangle$ in (a) has a height of -0.24.

one. This is not the case in our experiment, due to slight misalignments and imperfections of the q-plates, which result in the creation of higher order transverse modes. In figure 5.7 we show the reconstructed density matrix for both states (minus and plus) when not passing through the aperture, but using both q-plates to create the desired plus and minus states in between. On the matrix diagonal we see predominantly the two contributions from $|RR\rangle$ and $|LL\rangle$ polarisations and off diagonal the corresponding coherence, showing that indeed this are entangled states and not only mixed states. The small contributions from $|RL\rangle$ and $|LR\rangle$ are due imperfect transformations of the q-plates, but we see that there is no coherence between those. The only difference between minus and plus state is the phase between the two terms, represented by the sign of the off-diagonal elements.

The measurement becomes even more challenging when transmitting the states through the nanoaperture, since the available coincidence count rate drops significantly (see appendix C for details on the positioning of the nanoaperture). In figure 5.8 we present the reconstructed polarisation states after the interaction with the nanoaperture. The different behaviour of

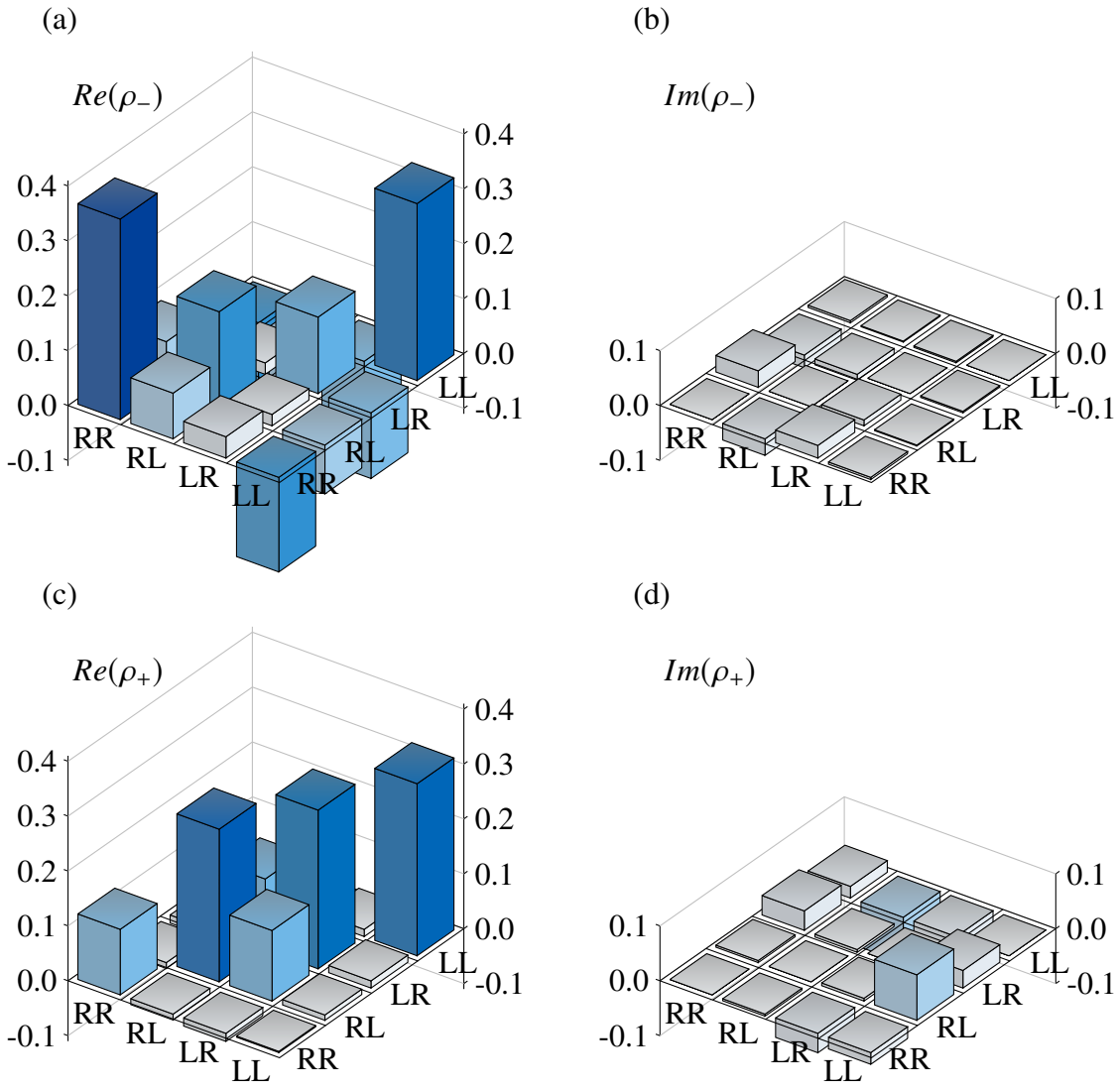

Figure 5.8: Reconstructed density matrices ((a,c) real parts and (b,d) imaginary parts) of the Laguerre-Gaussian minus (a,b) and plus (c,d) states after interaction with the nanoaperture. The element $|LL\rangle$-$|RR\rangle$ in (a) has a height of -0.19.

minus and plus states is obvious. Where the minus state remains very similar to the state before the interaction (cf. figure 5.7 (a,b)), with only slightly increased contributions from mixed polarisation channels, the plus state has changed dramatically. Its coherence between the $|RR\rangle$ and $|LL\rangle$ contributions has completely vanished, while mixed terms are as strong as the pure $|RR\rangle$ and $|LL\rangle$ contributions. Interestingly, some coherence between the $|RL\rangle$ and $|LR\rangle$ terms has emerged, as can be seen by the significant contribution of the $|RL\rangle$ - $|LR\rangle$ term in the real part of the minus state density matrix (cf. figure 5.8 (c)).

	no interaction		interaction with aperture	
	$\|\Psi_-\rangle$	$\|\Psi_+\rangle$	$\|\Psi_-\rangle$	$\|\Psi_+\rangle$
concurrence	0.253 ± 0.009	0.233 ± 0.009	0.220 ± 0.048	0.020 ± 0.019
negativity	0.253 ± 0.009	0.230 ± 0.009	0.201 ± 0.044	0.017 ± 0.016
fidelity to $\|RR\rangle + e^{i\phi}\|LL\rangle$	0.624 ± 0.004	0.603 ± 0.005	0.515 ± 0.024	0.270 ± 0.020

Table 5.1: Comparison of entanglement related quantities between minus and plus states before and after the interaction with the nanoaperture. The concurrence is a monotone measure of entanglement, where a completely mixed state has a concurrence of 0. The fidelity gives the overlap to the ideal polarisation state.

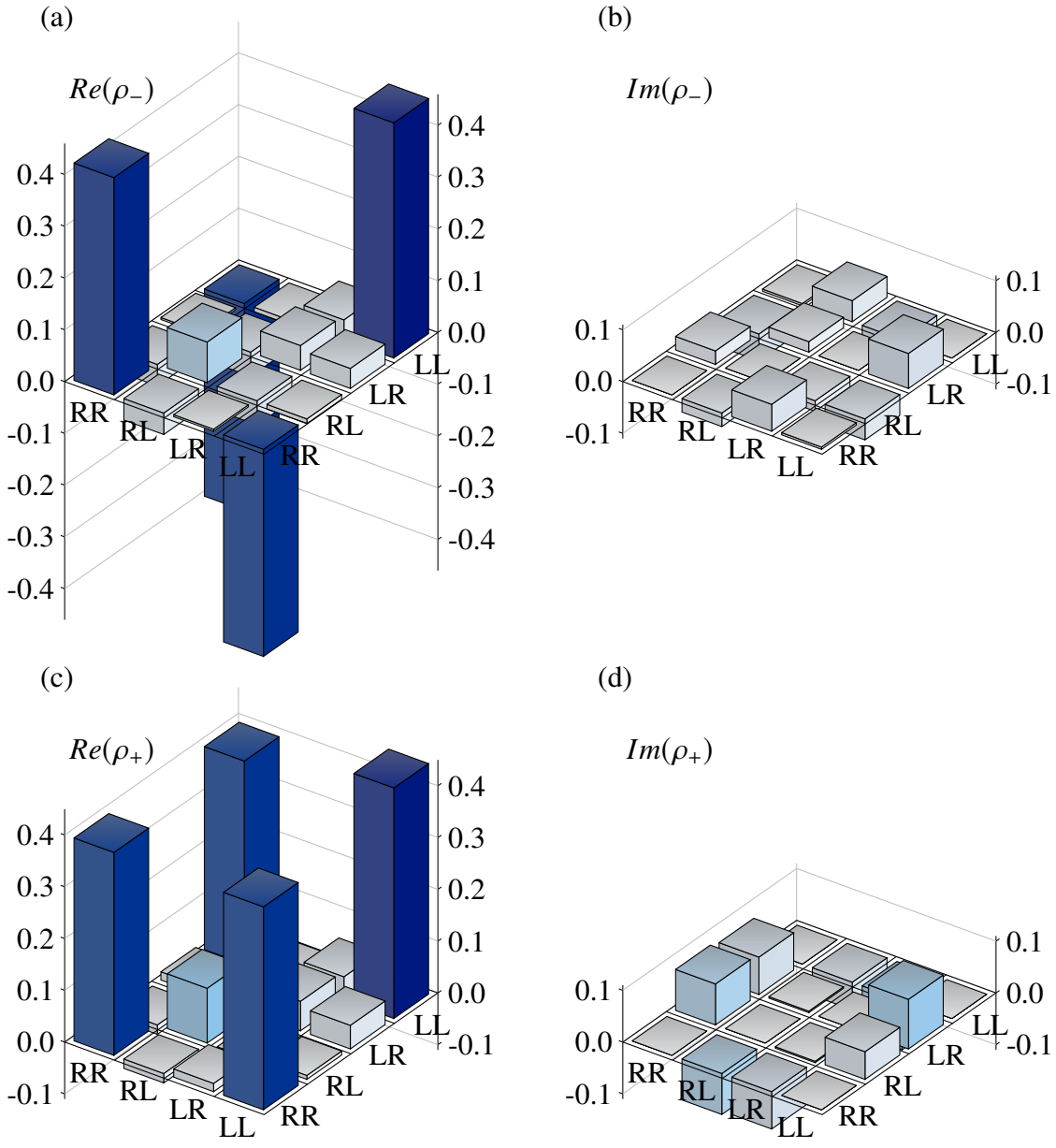

Figure 5.9: Reconstructed density matrices ((a,c) real parts and (b,d) imaginary parts) of the Gaussian minus (a,b) and plus (c,d) states without interaction with the nanoaperture.

We now want to quantify the changes from the initial states to the state after the interaction with the nanoaperture. See table 5.1 for a summary of relevant quantities. The concurrence is an entanglement measure [28, 30] related to the entanglement of formation, where a value of zero indicates a completely mixed state and a value of one is given for a maximally entangled state. The same is true for the negativity, which is a measure for the entanglement that can be distilled from a given state [30]. We find that both concurrence and negativity are small but consistent for both minus and plus state when no interaction takes place. In comparison, we do reach a concurrence of 0.7 ± 0.02 if not transitioning to the total angular momentum zero space. See figure 5.9 for the density matrices in that case. The loss of entanglement if transitioning to the total angular momentum zero space is purely due to the imperfect reversion of orbital angular momentum transfer by the second q-plate. However, both states show initially the same degree of entanglement and most importantly, this entanglement is fully preserved in the case of the minus state when interacting with the nanoaperture. The entanglement of the plus state after the interaction in contrast, is reduced to virtually nothing. A very similar picture is given by the fidelity, which measures the state overlap with an ideal bell state. The fidelity is mostly preserved by the minus state through the interaction, whereas the fidelity of the plus state is greatly reduced, as is also obvious from directly comparing density matrices in figures 5.7 (c) and 5.8 (c).

5.5 Discussion

Every quantum technology relies on stable and controllable quantum states. One of the most prominent examples is surely the quantum computer, but with smaller resource requirements also quantum metrology or quantum cryptography need excellent control over the employed states. Protecting these states or qubits from unwanted interactions with the environment is a major field of research for all platforms of quantum technologies. We believe that through smart engineering, interactions with the environment can be reduced or even inhibited. In this chapter, we have demonstrated that entanglement carried by photonic qubits can be protected from complete degradation by exploiting the characteristics of this interaction. The transmission through an aperture smaller than the wavelength of light is an example for a very strong environment interaction. With the miniaturisation of quantum technologies from laboratories into real world devices such a scenario will become increasingly relevant.

The results so far represent a significant step towards protecting quantum resources from degradation. We believe it possible to identify structures that protect more than one quantum state at a time. For now, even in the system presented, many interesting questions remain. One of them is to understand the exact behaviour of the plus state and its deterioration through the interaction. Looking at the density matrix of figure 5.8 (c), we observe that coherence emerges for the $|RL\rangle$ term but not between the original state and the $|RL\rangle$ terms, nor does any coherence remain for the initial state, which is not directly obvious from equation (5.17). Furthermore, the small $|RR\rangle$ term seems to be reproducible which we do not have an explanation for at this stage. We would expect $|RR\rangle$ and $|LL\rangle$ terms to behave in exactly the same way, considering the symmetries of the system.

6 Conclusion

In the last chapter of this thesis we summarise our findings (section 6.1) and present an outlook (section 6.2) on how our work may be continued in the future. We discuss open questions and potential extensions.

6.1 Summary

The overarching theme of this thesis is the improvement of control over quantum states of light in order to interact with nano structures. In chapter 3, we started with a detailed look at two-photon correlations from SPDC in their temporal degree of freedom. We found that the time delay between signal and idler photons can be tuned via the relative position of the non-linear crystal to the collection lens. That this effect had not been reported before, was very surprising to us, considering that SPDC has been the workhorse of photonic quantum information experiments for decades. To unambiguously prove the existence of the time delay shift also for other experimental situations we developed – in addition to the Hong-Ou-Mandel interference based measurement – a direct time delay measurement. We achieved a precision far below the timing resolution of the avalanche photo detectors and even the bin width of the coincidence counting electronics. The measured delay is relevant for all collinear type II SPDC experiments and has significant consequences, if the photons are not split before being overlapped, in an interference experiment.

With the motivation to gain more insights into the wave function of the SPDC pair, especially the structure of the temporal correlations, we developed a novel reconstruction method in chapter 4. It allows us to measure the complex spectral wave function via a generalised Hong-Ou-Mandel interference in two dimensions. Apart from the obvious advantage of having direct measurement access to the complex spectral wave function, we have also demonstrated the ability to shape the wave function by selection of the detection mode. In order to maintain the necessary stability to perform a two-dimensional Hong-Ou-Mandel scan, we developed and implemented specific correction and normalisation techniques. We believe our reconstruction scheme to become a valuable tool to study the two-photon wave function of type II SPDC. Furthermore, the demonstrated ability to shape the wave function by simply changing the collection mode, could open exciting possibilities towards engineered quantum states.

We then, in chapter 5, used the tools developed in the preceding chapters to create a tailored two-photon state, engineered for the interaction with a plasmonic nanoaperture. For the first time, we have sent an entangled photon pair through a single aperture smaller than the wavelength. We have shown that the interaction between aperture and two-photon state usually destroys entanglement, except for one special state, for which the entanglement is protected from degradation because of quantum interference. The measurement was very challenging, due to significant losses of the Laguerre-Gaussian mode and the long integration times necessary. With a sophisticated stabilisation and positioning protocol we were able to show quantum interference between the photons in two helicity channels and – through state tomography – to demonstrate that the entanglement is preserved. We believe this work to be an important step towards combining quantum optics and nano-photonics. The idea of quantum states engineered with a particular interaction in mind could also prove valuable for other systems.

6.2 Outlook

The wave function reconstruction scheme could provide insight into a variety of different down-conversion situations and we have only started to explore some of them in chapter 4. We believe it would be worthwhile to study other detection modes, as well as spatial pump modes. The case of the Laguerre-Gaussian detection mode already showed a surprising

feature and we believe that other spatial modes could give rise to even more unusual temporal and spectral features.

Following up on the split structure of the time delay distribution (cf. figure 4.7 (c)), we have speculated (see section 4.5) that it could be possible to generate time bin entangled photons from this correlation. The suppression of the central delay could possibly be further enhanced with higher order Laguerre-Gaussian detection modes. This would be a very simple implementation of a source for time bin entangled photons. The only requirement being the collection of a specific mode, exactly as we have demonstrated in the setup of the wave function reconstruction scheme. Once coupled to the single mode fibre, the time bin entangled pair could be used for arbitrary experiments.

One open question that waits to be answered is the exact transformation of the plus state in the interaction with the nanoaperture. We have seen that it loses its entanglement, but the density matrix (cf. figure 5.8) shows a peculiarity after passing through the aperture. The coherence of the initial state disappears completely and instead some coherence between the terms of flipped helicity arises. We believe an investigation of this behaviour could lead to further insights into the complex interplay between entangled photons states and localised plasmons.

For future experiments on the interaction of quantum states carrying orbital angular momentum with nano-structures, the reversal of the orbital angular momentum transfer should be optimised to improve the quality of tomographic measurements. One possible extension that obviates the need for the back transformation would be a full state tomography, sorting the state not only into individual helicity, but also orbital angular momentum channels. Such a measurement would allow us to study the transformation of the whole state, entangled in spin and orbital angular momentum.

In this thesis we have demonstrated that the wave function of the two-photon state can be controlled in polarisation, spatial and temporal degrees of freedom to an exquisite precision. We can measure it and perform very delicate controlled interactions with nano structures. Reaching a bit farther beyond our work, we envision pump probe experiments with plasmonic nanostructures at the single photon limit. By utilising the techniques we have demonstrated in this work for control over temporal correlations, the arrival of signal and idler photons could be scanned or engineered to measure or fit some specific response of the plasmonic nano-structure. The crystal position or a birefringent delay line could be used to tune the time delay between the SPDC photons. Even more interesting would be to shape the temporal correlation function with a suitable spatial collection mode. Such pump probe measurements could give insights into decay time scales of localised plasmons or possibly open the way to photon-photon interactions through the interaction with plasmonic structures.

A

Appendix – Coincidence detection system

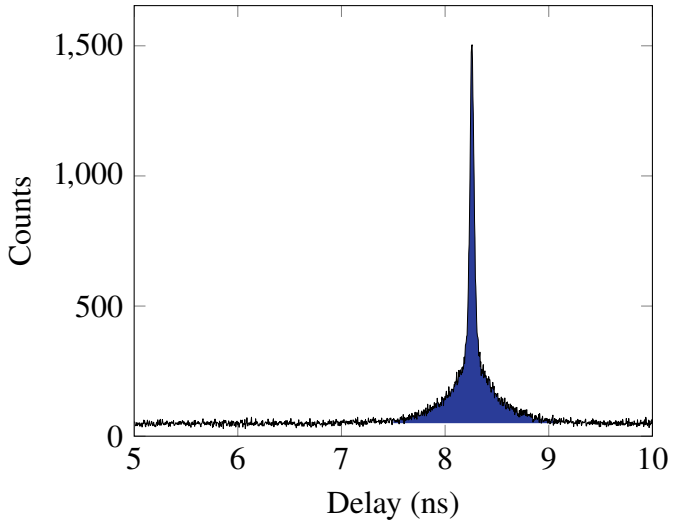

Figure A.1: Delay time histogram between signal and idler photons using APDs with a timing resolution of about 60 ps. The coloured area corresponds to the counts used for any subsequent calculation. It is defined by the area under the curve within a suitably chosen coincidence window minus the accidental coincidences.

A fundamental quantity for many of the experiments and measurements described throughout this thesis is the number of coincidences between two detection channels in a certain time interval. The simultaneous arrival of two photons in separate channels is usually detected with single photon detectors and a time to amplitude conversion electronic that allows for the discrimination between correlated and uncorrelated events. We have used different types of silicon avalanche photo diodes (APDs) for the three main projects described in this thesis. For the wavefunction reconstruction measurements of chapter 4 we used fibre-coupled APDs (Perkin Elmer). The direct time delay measurements of the SPDC pairs in chapter 3 required detectors with a very high time resolution (SPD-020-CTF from Micro Photon Devices). The experiment on the entanglement protection relied on APDs

optimised for use around 800 nm (Count50-N by LaserComponents). Every single photon detector generates an electrical signal, which in our case is routed to a time correlated single photon counting module (PicoHarp 300 by PicoQuant). This records the difference in arrival time for two subsequent events and builds up a histogram of those arrival time differences. Figure A.1 shows an example of such a delay time histogram. From this histogram a suitable coincidence window can be chosen, all counts within that window summed and accidental counts subtracted. Accidental counts are those that do not belong to a pair but to two single photons that have arrived by pure chance at the detectors in this time window. Their number can be reliably estimated evaluating the coincidence count rate outside of the coincidence window.

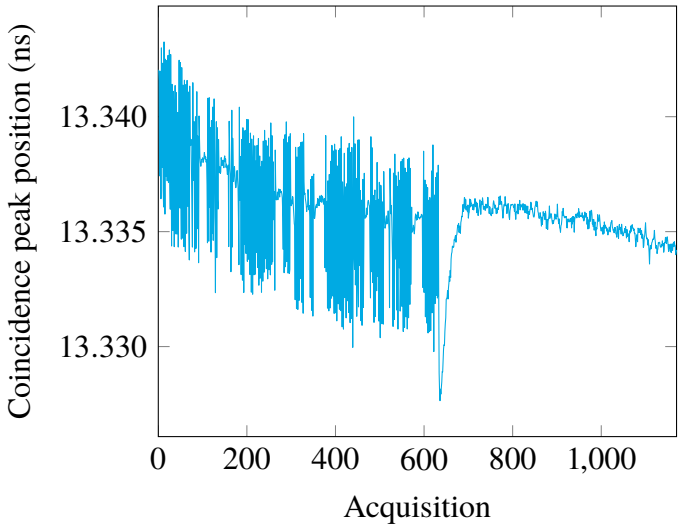

Figure A.2: Stability of the coincidence detection system after start-up. The curve shows the position of the coincidence peak for every measurement of approximately 2 minutes. The complete plot shows approximately 40 hours. Some sort of event after about 20 hours leads to a much more stable peak.

For very precise measurements of the average arrival time difference of a large number of photons the stability of the coincidence counting electronics plays a significant role. With the PicoHarp system we have observed a peculiar behaviour after start-up, which we show in figure A.2. The curve depicts the repeatedly measured arrival time difference between signal and idler photons of our SPDC source under unchanged experimental conditions. Each single measurement acquired data for 2 minutes and the whole curve shows the first 40 hours after switching on the PicoHarp. Surprising to us was the observation that it takes many hours for the coincidence detection system to reach a stable state. This general behaviour – strong fluctuations in the beginning and then stabilisation after a sudden jump – was reproduced several times.

For a short time during the entanglement protection experiment, we have actually used four APDs instead of only two as described in chapter 5. This would have allowed us to simultaneously measure correlations in and between the channels of opposite and equal polarisation. Unfortunately, we had to give up this approach, because the APDs broke down too fast. However, we would like to briefly comment on the possibility to operate four independent APDs with the PicoHarp system in time tagged and time resolved (TTTR) mode. This mode does not build a histogram as discussed in the previous paragraph, but instead records the arrival time of each electrical pulse in any one of the two input channels.

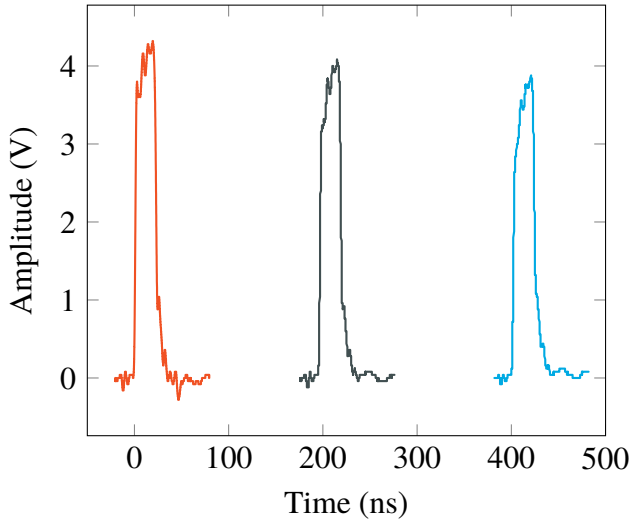

Figure A.3: Pulse shape of an avalanche photo diode TTL signal after no delay (red) and after passing through 50 m (black) or 100 m (blue) of coaxial cable.

An additional device, the router (PHR 800 by PicoQuant) extends the number of available input channels to five. However, the router does not measure time delays but only merges and forwards signals to the PicoHarp while supplying information from which channel the signal originated. In our case, one APD was wired directly to the PicoHarp, while the other three signals were sent through the router. Since coincidences are expected to happen between any two of the channels, this would usually lead to problems because two events could be merged together and then not be detected by the PicoHarp, because of its dead time. After a detection event in the PicoHarp, the system is not available to detect any other signal in that channel for about 100 ns. Also the router comes with such a dead time of about 50 ns. Our solution to this problem is to delay the signals that are to be merged by the router by this cumulative dead time from each other. The first signal can be fed to the router without a delay, the second one with a delay of at least 150 ns and the third one with a delay of more than 300 ns.

Delaying an electrical signal with a sharp edge, which is necessary for the accurate detection of the signal, by such a long time is not a simple task. Solutions based on integrated electronics bear the risk of introducing additional timing jitter and to distort the signal. We have opted for a pure cable based approach, using high quality coaxial cables (Ecoflex 15) to delay the signals with respect to each other. See figure A.3 for a comparison of the signal shapes after 0 m, 50 m and 100 m of coaxial cable. The high quality of the cable is very important, since the steep rise of the signal translates to a high frequency, which is damped strongly in thin and long cables. The cables we are using have a specified damping of 9.8 dB/100m at 1 GHz. This approach allowed us to reliably record coincidences between any two of the four single channels without any restrictions. It is also possible to detect three or four-fold coincidences with exactly the same technique.

B

Appendix – Time delay adjustment system

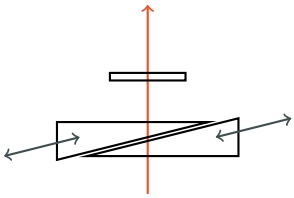

Figure B.1: Schematic of the two calcite wedges and the fixed length offset calcite crystal. The beam of orthogonally polarised photon pairs is shown in red. The arrows indicate the movement of the wedges to change the path length of the beam inside the calcite and with it the time delay between the two photons.

Modifying the time delay between signal and idler photon of a collinear, type II down-conversion source is an important capability for many measurements described in this thesis. If the photons are available in separate spatial channels, changing the time delay is simply achieved by changing the path-length difference. However, if the time delay should be adjusted without the photons being separated, a different solutions is necessary. In the case of photon pairs with orthogonal linear polarisation, a suitably oriented birefringent medium can delay one photon with respect to the other due to the different group velocities each photon experiences within the medium. The length of the path inside the medium then determines the amount of relative shift. To be able to continuously tune the time delay over an interval, we employ two calcite wedges on motorised stages (see drawing B.1). Using two instead of only one wedge and moving the wedges in parallel to their sloped edge, allows us to maintain the beam direction and avoid a beam displacement. Since the path length inside the crystal can not be reduced to zero with two wedges and a finite beam diameter, we use an additional fixed length crystal to reverse some of the delay change due to the wedges. With a usable thickness of the wedges between 2 mm and 14 mm and the additional slab of 2 mm, we achieve a time delay tuning range of 0 ps to 7.14 ps. This is about twice the amount that could be picked up by a pair traveling through the whole length of down-conversion crystal (see chapter 3 for details).

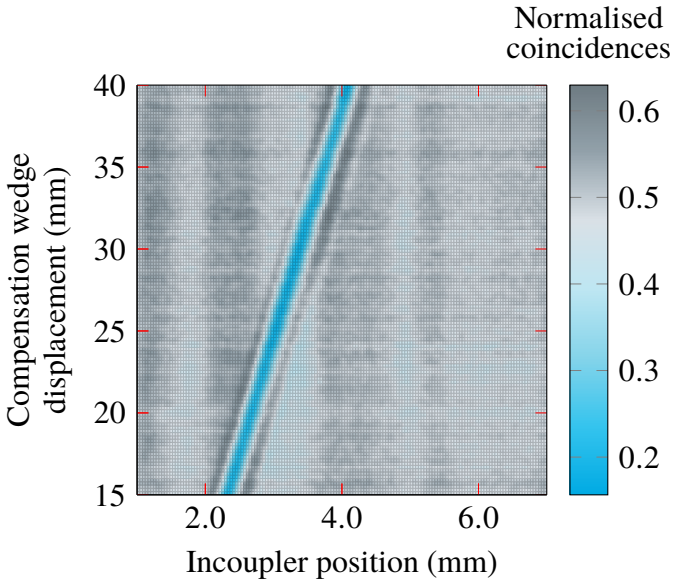

Figure B.2: Surface of the normalised coincidence rate as a function of the free space path-length difference and the displacement of the calcite compensation crystals. The pairs are delayed in the calcite wedges while still collinear, then split by a polarising beam-splitter, coupled to single mode fibres with a variable distance and then overlapped on a fibre beam-splitter. Only if the delay shifts of both direct path length and calcite compensator cancel the initial delay of the pair, will the photons interfere on the beam-splitter and create the Hong-Ou-Mandel dip. We can check the correct operation of the compensation crystals with this setup and calibrate the compensation wedge positions. The stripes along lines of constant incoupler position are due to slight fluctuations of the incoupling efficiency, that are necessarily independent of temperature.

To check the correct operation of the compensation wedges and to calibrate the calcite wedge positioning, we measure a standard Hong-Ou-Mandel interference with respect to both free space path-length difference and calcite wedge position. Figure B.2 shows the resulting coincidence count rate surface. The displacement of the wedges happens simultaneously for both wedges and is parallel to their hypotenuse, as seen in drawing B.1. We find that over 25 mm of wedge displacement, the incoupler has to be moved by 1.76 mm, which translates via the speed of light in vacuum to a delay of 5.87 ps.

An additional advantage of the fixed length slab of calcite, that is used to compensate some of the changes by the wedges, is the fact that it can be rotated by 90° and thus shift the time delay far off. This can be very useful if scans in time delay are performed, while the photons are coupled to fibres later on. Tiny variations in the beam orientation (due to the wedge position) can lead to fluctuations of the incoupled intensity. However, these fluctuations can be discriminated from the actual physical changes due to the changed time delay, by scanning also with the fixed length calcite slab turned. This creates a reference scan where only the incoupling can be responsible for intensity changes, because the photon pairs are well distinguishable for the whole range of scanning positions.

C

Appendix – Nanoaperture sample and positioning

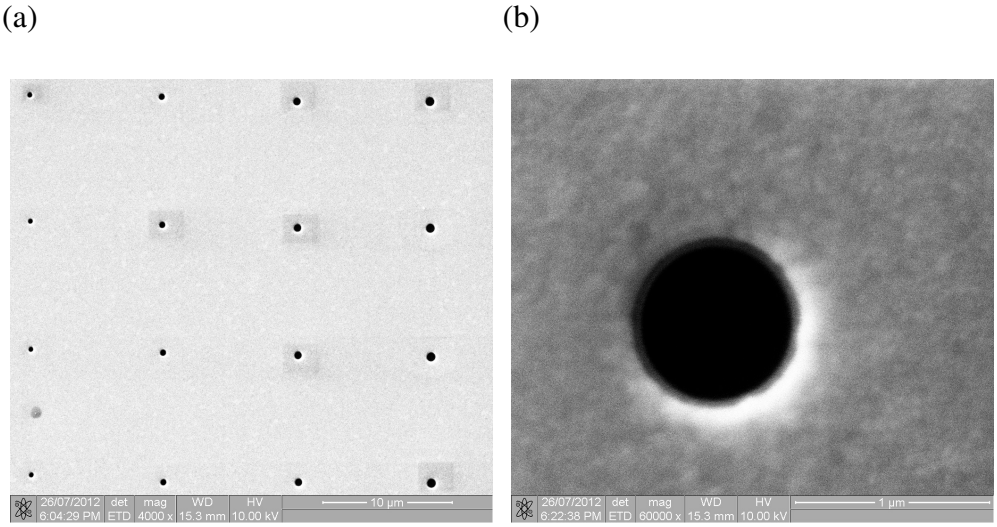

Figure C.1: Scanning electron microscope images of (a) an array of circular nanoapertures milled into a gold layer with a focused ion beam and (b) the details of a single aperture.

The plasmonic nano-structures used for the entanglement protection experiments in chapter 5, are isolated, sub-wavelength apertures in a gold film of 150 nm thickness. Figure C.1 shows two scanning electron microscopy images of the sample used. The holes have a diameter between 750 nm and 280 nm, which is well below the wavelength of the down-converted light of 808 nm. We focus the photon pairs onto the nanoaperture with a 0.85 NA objective optimised for the near infrared and collect the transmitted light with a 1.4 NA, oil immersion objective. Positioning the sample between the two objectives is achieved by a pair of

manually controlled micrometer stages and a stack of three, electronically controlled nano-positioners. Transmitting SPDC pairs not carrying orbital angular momentum through the aperture is relatively straight forward due to only moderate losses of around 50 % of single counts. The smallest possible $1/e^2$ beam diameter at the focus of the 0.85 NA objective is $d \approx \lambda/(2\pi\mathrm{NA}) \approx 600\,\mathrm{nm}$ for such a Gaussian beam. With the actual engineered state of the experiment, which is carrying one quantum of orbital angular momentum, the situation is significantly different due to the much wider beam diameter. The losses are about 90 % of the initial singles counts when using a vortex beam carrying one quantum of orbital angular momentum through the 750 nm aperture. To compensate for the small count rates we need to integrate for several tens of seconds. Furthermore, some of the measurements are based on a large number of individual measurements. This requires the whole setup and especially the sample position within the beam to be extremely stable. We experience slow drifts on the time scale of an hour, even though we operate the nano-positioners in a closed loop mode. Such an excursion of the centre of the incident beam from the centre of the aperture must of course be prevented to maintain the symmetry of the whole system.

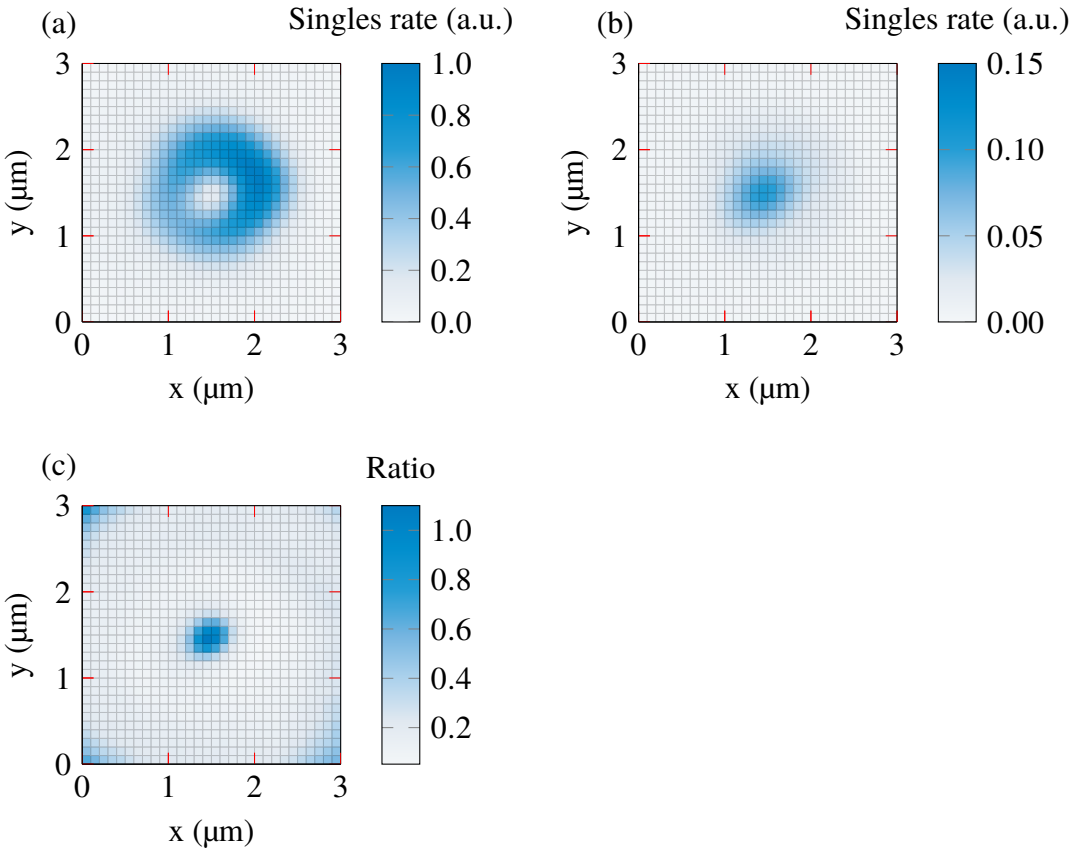

Figure C.2: Spatial scans with the nanoaperture, showing the single count rates in the unchanged helicity channel (a), the flipped helicity channel (b) and the ratio of the two (c) with single incident photons carrying orbital angular momentum. We use the ratio of counts between changed and unchanged helicity to centre the aperture with respect to the incident beam. The singles count rates shown are normalised to the same value.

We employ two different automatic position optimisation schemes depending on whether the beam carries orbital angular momentum or not. Due to the higher count rates of the Gaussian beam, it is sufficient to optimise the total count rate measured after the aperture,

by adjusting the sample position subsequently and repeatedly in all three axis. If the beam carries orbital angular momentum, we make use of the helicity flip probability, which is highest, if beam and aperture are concentric. A spatial scan of the aperture in the two directions transverse to the incident beam is shown in figure C.2. Using only one of the two down-converted photons, we can selectively measure the count rates in the unchanged and changed helicity channels with the setup shown in figure 5.2. The spatial map of the unchanged helicity channel (figure C.2 (a)) produces – as expected – the doughnut beam profile. If the aperture is well centred with respect to this doughnut, the unchanged helicity is minimal and the changed helicity is at its maximum. This gives rise to a sharp peak in the ratio between these two count rates, which we use to find the optimal position of the aperture. Since this is only possible with a defined input polarisation, we use a linear polariser after the SPDC source to select only one of the two photons. All measurements are fully automatised, so that this re-positioning algorithm can be performed regularly, countering any slow drift.

D

Appendix – Re-emission of photons from avalanche photo diodes

For the entanglement protection experiment (see chapter 5), we rely on free space avalanche photo diode (APDs) to detect and measure photon pairs transmitted through the nanoaperture. We found an initially puzzling behaviour in the arrival time histograms. See figure D.1 for an example. At this point in time we were still working with four APDs and were thus able to look at correlations between opposite and equal polarisation channels. Since the input pairs for this measurement are right and left circularly polarised, we expect to see one coincidence peak in the opposite polarisations channel (a) and nothing in the same polarisations channel. The surprising finding are the two side-peaks centred at ± 10 ns, which only occur when the pairs are transmitted through the nanoaperture. We attribute this to the possibility that APDs can re-emit photons after a detection event. In our experiment, this re-emitted photon can then travel backwards until it is reflected by the gold surface of the sample. Any single photon not belonging to a pair and triggering a detection event could be identified as part of a coincidence with a re-emitted photon from that detection event. This is only happening in the coincidence channel of opposite polarisations, because of the phase flip the re-emitted photon is experiencing when being reflected from the gold surface.

We confirmed this by coincidence measurements with single photons, where only one of the side-peaks remains in the histogram. The actual SPDC photon will always exclusively be detected in the detection arm with the right polarisation and the re-emitted photon then be detected in the other polarisation arm. Also, we found three photon coincidences (see figure D.2) in the time tagged and time resolved data that was used for the coincidence histograms of figure D.1. An accumulation of three photon coincidence at any specific time delay combination above the background of random events is naturally impossible with photon pairs. However, if a large number of photons is re-emitted after a detection event, two of these could be detected in the two detectors of the opposite polarisation arm, or a chain of two re-emissions could also create a three photon coincidence. Both of these possibilities show up in figure D.2. The peak at positive and equal time delays to the start event (upper right) corresponds to the three fold coincidence with two simultaneous detections of re-emitted photons and the other two peaks correspond to chains with two subsequent re-emissions.

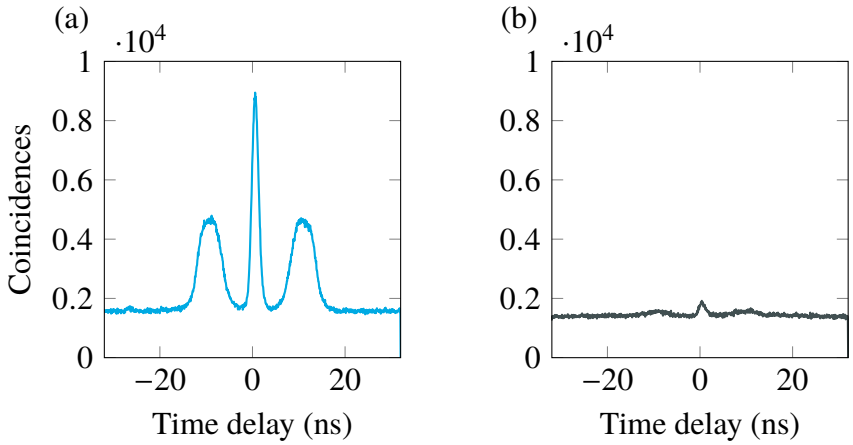

Figure D.1: Time delay histograms between channels of opposite polarisation (a) and equal polarisation (b) after transmission through a nanoaperture. The input is a left and right circularly polarised Gaussian photon pair.

This effect should be taken into account and it increases the noise in our measurements. Luckily, due to the sufficient delay in the re-emission, counts in the actual SPDC photon coincidence peak can reliably distinguished from coincidence events due to re-emitted photons.

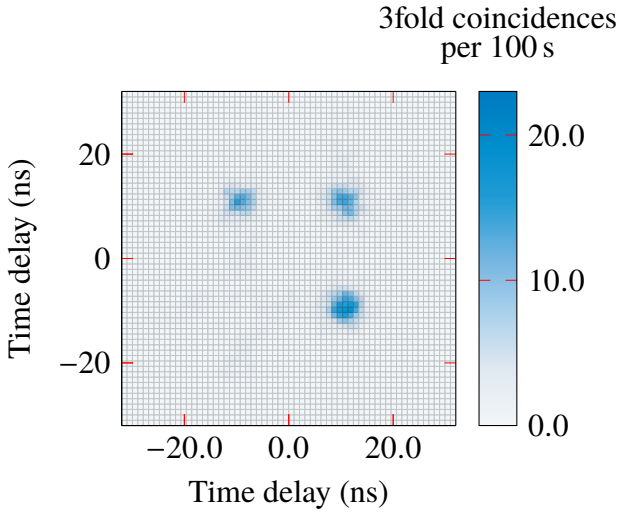

Figure D.2: Delay time histogram of three-fold coincidences between three of the four single photon detectors. The underlying time tagged and time resolved arrival time data is the same as for figure D.1.

References

[1] R. P. Feynman, R. B. Leighton, and M. L. Sands. *The Feynman lectures on physics* (Addison-Wesley, Redwood City, Calif., 1989).

[2] A. Einstein and L. Infeld. *The evolution of physics: The growth of ideas from early concepts to relativity and quanta*. New York, Simon and Schuster **1** (1938).

[3] A. Einstein, B. Podolsky, and N. Rosen. *Can quantum-mechanical description of physical reality be considered complete?* Phys. Rev. **47**(10), 777 (1935). URL http://link.aps.org/doi/10.1103/PhysRev.47.777.

[4] E. Schrödinger. *Discussion of probability relations between separated systems*. Mathematical Proceedings of the Cambridge Philosophical Society **31**(04), 555 (1935). URL http://journals.cambridge.org/article_S0305004100013554.

[5] N. Gisin. *Quantum Chance: Nonlocality, Teleportation and Other Quantum Marvels* (Springer International Publishing, Cham, 2014).

[6] A. Aspect. *Quantum mechanics: To be or not to be local*. Nature **446**(7138), 866 (2007). URL http://dx.doi.org/10.1038/446866a.

[7] D. Salart, A. Baas, C. Branciard, N. Gisin, and H. Zbinden. *Testing the speed of spooky action at a distance*. Nature **454**(7206), 861 (2008). URL http://dx.doi.org/10.1038/nature07121.

[8] A. Einstein, M. Born, and H. Born. *The Born-Einstein Letters: Correspondence between Albert Einstein and Max and Hedwig Born from 1916 to 1955 with commentaries by Max Born* (The Macmillan Press Ltd, 1971).

[9] J. S. Bell. *On the einstein podolsky rosen paradox*. Physics **1**(3), 195 (1964).

[10] S. J. Freedman and J. F. Clauser. *Experimental test of local hidden-variable theories*. Phys. Rev. Lett. **28**(14), 938 (1972). URL http://link.aps.org/doi/10.1103/PhysRevLett.28.938.

[11] A. Aspect, P. Grangier, and G. Roger. *Experimental tests of realistic local theories via bell's theorem*. Phys. Rev. Lett. **47**(7), 460 (1981). URL http://link.aps.org/doi/10.1103/PhysRevLett.47.460.

[12] G. Weihs, T. Jennewein, C. Simon, H. Weinfurter, and A. Zeilinger. *Violation of bell's inequality under strict einstein locality conditions*. Phys. Rev. Lett. **81**(23), 5039 (1998). URL http://link.aps.org/doi/10.1103/PhysRevLett.81.5039.

[13] L. K. Shalm, E. Meyer-Scott, B. G. Christensen, P. Bierhorst, M. A. Wayne, M. J. Stevens, T. Gerrits, S. Glancy, D. R. Hamel, M. S. Allman, K. J. Coakley, S. D. Dyer, C. Hodge, A. E. Lita, V. B. Verma, C. Lambrocco, E. Tortorici, A. L. Migdall, Y. Zhang, D. R. Kumor, W. H. Farr, F. Marsili, M. D. Shaw, J. A. Stern, C. Abellán, W. Amaya, V. Pruneri, T. Jennewein, M. W. Mitchell, P. G. Kwiat, J. C. Bienfang, R. P. Mirin, E. Knill, and S. W. Nam. *Strong loophole-free test of local realism*. Phys. Rev. Lett. **115**(25), 250402 (2015). URL http://link.aps.org/doi/10.1103/PhysRevLett.115.250402.

[14] M. Giustina, Versteegh, Marijn A. M., S. Wengerowsky, J. Handsteiner, A. Hochrainer, K. Phelan, F. Steinlechner, J. Kofler, J.-Å. Larsson, C. Abellán, W. Amaya, V. Pruneri, M. W. Mitchell, J. Beyer, T. Gerrits, A. E. Lita, L. K. Shalm, S. W. Nam, T. Scheidl, R. Ursin, B. Wittmann, and A. Zeilinger. *Significant-loophole-free test of bell's theorem with entangled photons*. Phys. Rev. Lett. **115**(25), 250401 (2015). URL http://link.aps.org/doi/10.1103/PhysRevLett.115.250401.

[15] P. W. Shor. *Scheme for reducing decoherence in quantum computer memory*. Phys. Rev. A **52**(4), R2493 (1995). URL http://link.aps.org/doi/10.1103/PhysRevA.52.R2493.

[16] D. Beckman, A. N. Chari, S. Devabhaktuni, and J. Preskill. *Efficient networks for quantum factoring*. Phys. Rev. A **54**(2), 1034 (1996). URL http://link.aps.org/doi/10.1103/PhysRevA.54.1034.

[17] D. Kielpinski, C. Monroe, and Wineland, D. J. *Architecture for a large-scale ion-trap quantum computer*. Nature **417**(6890), 709 (2002). URL http://dx.doi.org/10.1038/nature00784.

[18] A. Trifonov and A. Zavriyev. *Secure communication with a heralded single-photon source*. Journal of Optics B: Quantum and Semiclassical Optics **7**(12), S772 (2005).

[19] R. Ursin, F. Tiefenbacher, T. Schmitt-Manderbach, H. Weier, T. Scheidl, M. Lindenthal, B. Blauensteiner, T. Jennewein, J. Perdigues, P. Trojek, B. Ömer, M. Fürst, M. Meyenburg, J. Rarity, Z. Sodnik, C. Barbieri, H. Weinfurter, and A. Zeilinger. *Entanglement-based quantum communication over 144 km*. Nature Physics **3**(7), 481 (2007).

[20] A. Sergienko and G. Jaeger. *Quantum information processing and precise optical measurement with entangled-photon pairs*. Contemporary Physics **44**(4), 341 (2003).

[21] I. Afek, O. Ambar, and Y. Silberberg. *High-noon states by mixing quantum and classical light*. Science **328**(5980), 879 (2010).

[22] A. I. Lvovsky. *Squeezed light*. ArXiv e-prints (2014). URL http://arxiv.org/abs/1401.4118.

[23] The LIGO Scientific Collaboration. *Observation of gravitational waves from a binary black hole merger*. Phys. Rev. Lett. **116**(6), 061102 (2016). URL http://link.aps.org/doi/10.1103/PhysRevLett.116.061102.

[24] The LIGO Scientific Collaboration. *A gravitational wave observatory operating beyond the quantum shot-noise limit*. Nat Phys **7**(12), 962 (2011). URL http://dx.doi.org/10.1038/nphys2083.

[25] U. Fano. *Description of states in quantum mechanics by density matrix and operator techniques*. Rev. Mod. Phys. **29**(1), 74 (1957). URL http://link.aps.org/doi/10.1103/RevModPhys.29.74.

[26] H. Barnum, E. Knill, G. Ortiz, R. Somma, and L. Viola. *A subsystem-independent generalization of entanglement*. Phys. Rev. Lett. **92**(10), 107902 (2004). URL http://link.aps.org/doi/10.1103/PhysRevLett.92.107902.

[27] L. Gurvits. *Classical deterministic complexity of edmonds' problem and quantum entanglement*. In *Proceedings of the Thirty-fifth Annual ACM Symposium on Theory of Computing*, STOC '03, pp. 10–19 (ACM, New York, NY, USA, 2003). URL http://doi.acm.org/10.1145/780542.780545.

[28] M. B. Plenio and S. Virmani. *An introduction to entanglement measures*. Quantum Info. Comput. **7**(1), 1 (2007). URL http://dl.acm.org/citation.cfm?id=2011706.2011707.

[29] W. K. Wootters. *Entanglement of formation of an arbitrary state of two qubits*. Phys. Rev. Lett. **80**(10), 2245 (1998). URL http://link.aps.org/doi/10.1103/PhysRevLett.80.2245.

[30] F. Verstraete, K. Audenaert, J. Dehaene, and B. De Moor. *A comparison of the entanglement measures negativity and concurrence*. Journal of Physics A: Mathematical and General **34**(47), 10327 (2001). URL http://stacks.iop.org/0305-4470/34/i=47/a=329.

[31] R. W. Boyd. *Nonlinear optics* (Academic Press, 2003).

[32] D. A. Kleinman. *Theory of optical parametric noise*. Physical Review **174**(3), 1027 (1968).

[33] D. C. Burnham and D. L. Weinberg. *Observation of simultaneity in parametric production of optical photon pairs*. Phys. Rev. Lett. **25**(2), 84 (1970). URL http://link.aps.org/doi/10.1103/PhysRevLett.25.84.

[34] Y. Shih. *Entangled biphoton source - property and preparation*. Reports on Progress in Physics **66**(6), 1009 (2003).

[35] P. Mosley, J. Lundeen, B. Smith, P. Wasylczyk, A. U'Ren, C. Silberhorn, and I. Walmsley. *Heralded generation of ultrafast single photons in pure quantum states*. Physical Review Letters **100**(13) (2008).

[36] C. K. Hong and L. Mandel. *Theory of parametric frequency down conversion of light*. Phys. Rev. A **31**(4), 2409 (1985). URL http://link.aps.org/doi/10.1103/PhysRevA.31.2409.

[37] S. Tanzilli, H. d. Riedmatten, H. Zbinden, P. Baldi, M. d. Micheli, D. B. Ostrowsky, N. Gisin, *et al. Highly efficient photon-pair source using periodically poled lithium niobate waveguide*. Electronics Letters **37**(1), 26 (2001).

[38] J. A. Armstrong, N. Bloembergen, J. Ducuing, and P. S. Pershan. *Interactions between light waves in a nonlinear dielectric*. Phys. Rev. **127**(6), 1918 (1962). URL http://link.aps.org/doi/10.1103/PhysRev.127.1918.

[39] Jin, Alexander Ling Euk. *Entangled State Preparation For Optical Quantum Communication: Creating and characterizing photon pairs from Spontaneous Parametric Down Conversion inside bulk uniaxial crystals*. Ph.D. thesis, National University of Singapore, Singapore (2008). URL https://www.quantumlah.org/media/thesis/thesis-alex.pdf.

[40] C. Kuklewicz, M. Fiorentino, G. Messin, F. Wong, and J. Shapiro. *High-flux source of polarization-entangled photons from a periodically poled ktiopo_4 parametric down-converter*. Physical Review A **69**(1) (2004).

[41] C. Hong, Z. Ou, and L. Mandel. *Measurement of subpicosecond time intervals between two photons by interference*. Phys. Rev. Lett. **59**(18), 2044 (1987). URL http://link.aps.org/doi/10.1103/PhysRevLett.59.2044.

[42] P. Kok, H. Lee, and J. P. Dowling. *Creation of large-photon-number path entanglement conditioned on photodetection*. Phys. Rev. A **65**(5), 052104 (2002). URL http://link.aps.org/doi/10.1103/PhysRevA.65.052104.

[43] P. Walther, J.-W. Pan, M. Aspelmeyer, R. Ursin, S. Gasparoni, and A. Zeilinger. *De broglie wavelength of a non-local four-photon state*. Nature **429**(6988), 158 (2004).

[44] D. Bouwmeester, J.-W. Pan, K. Mattle, M. Eibl, H. Weinfurter, and A. Zeilinger. *Experimental quantum teleportation*. Nature **390**(6660), 575 (1997). URL http://dx.doi.org/10.1038/37539.

[45] E. Knill, R. Laflamme, and Milburn, G. J. *A scheme for efficient quantum computation with linear optics*. Nature **409**(6816), 46 (2001). URL http://dx.doi.org/10.1038/35051009.

[46] R. Lopes, A. Imanaliev, A. Aspect, M. Cheneau, D. Boiron, and Westbrook, C. I. *Atomic hong-ou-mandel experiment*. Nature **520**(7545), 66 (2015). URL http://dx.doi.org/10.1038/nature14331.

[47] J. S. Fakonas, H. Lee, Y. A. Kelaita, and H. A. Atwater. *Two-plasmon quantum interference*. Nat Photon **8**(4), 317 (2014). URL http://dx.doi.org/10.1038/nphoton.2014.40.

[48] K. Toyoda, R. Hiji, A. Noguchi, and S. Urabe. *Hong–ou–mandel interference of two phonons in trapped ions*. Nature **527**(7576), 74 (2015). URL http://dx.doi.org/10.1038/nature15735.

[49] J. Beugnon, Jones, M. P. A., J. Dingjan, B. Darquié, G. Messin, A. Browaeys, and P. Grangier. *Quantum interference between two single photons emitted by independently trapped atoms*. Nature **440**(7085), 779 (2006). URL http://dx.doi.org/10.1038/nature04628.

[50] A. Sipahigil, M. L. Goldman, E. Togan, Y. Chu, M. Markham, D. J. Twitchen, A. S. Zibrov, A. Kubanek, and M. D. Lukin. *Quantum interference of single photons from remote nitrogen-vacancy centers in diamond*. Phys. Rev. Lett. **108**(14), 143601 (2012). URL http://link.aps.org/doi/10.1103/PhysRevLett.108.143601.

[51] E. Bocquillon, V. Freulon, J.-M. Berroir, P. Degiovanni, B. Plaçais, A. Cavanna, Y. Jin, and G. Feve. *Coherence and indistinguishability of single electrons emitted by independent sources*. Science **339**(6123), 1054 (2013).

[52] D. Strekalov, A. B. Matsko, A. Savchenkov, and L. Maleki. *Quantum-correlation metrology with biphotons: where is the limit?* Journal of Modern Optics **52**(16), 2233 (2005).

[53] C. Santori, D. Fattal, J. Vuckovic, G. S. Solomon, and Y. Yamamoto. *Indistinguishable photons from a single-photon device*. Nature **419**(6907), 594 (2002). URL http://dx.doi.org/10.1038/nature01086.

[54] Y.-M. He, Y. He, Y.-J. Wei, D. Wu, M. Atature, C. Schneider, S. Hofling, M. Kamp, C.-Y. Lu, and J.-W. Pan. *On-demand semiconductor single-photon source with near-unity indistinguishability*. Nat Nano **8**(3), 213 (2013). URL http://dx.doi.org/10.1038/nnano.2012.262.

[55] V. Giovannetti, L. Maccone, J. H. Shapiro, and F. N. C. Wong. *Extended phase-matching conditions for improved entanglement generation*. Phys. Rev. A **66**(4), 043813 (2002). URL http://link.aps.org/doi/10.1103/PhysRevA.66.043813.

[56] V. Giovannetti, L. Maccone, J. H. Shapiro, and F. N. C. Wong. *Generating entangled two-photon states with coincident frequencies*. Phys. Rev. Lett. **88**(18), 183602 (2002). URL http://link.aps.org/doi/10.1103/PhysRevLett.88.183602.

[57] O. Kuzucu, M. Fiorentino, M. Albota, F. Wong, and F. Kärtner. *Two-photon coincident-frequency entanglement via extended phase matching*. Physical Review Letters **94**(8) (2005).

[58] M. Rubin. *Transverse correlation in optical spontaneous parametric down-conversion*. Physical Review A **54**(6), 5349 (1996).

[59] C. Law and J. Eberly. *Analysis and interpretation of high transverse entanglement in optical parametric down conversion*. Physical Review Letters **92**(12) (2004).

[60] S. Walborn, C. Monken, S. Pádua, and P. Souto Ribeiro. *Spatial correlations in parametric down-conversion*. Physics Reports **495**(4-5), 87 (2010).

[61] F. M. Miatto, A. M. Yao, and S. M. Barnett. *Full characterization of the quantum spiral bandwidth of entangled biphotons*. Physical Review A **83**(3) (2011).

[62] V. D. Salakhutdinov, E. R. Eliel, and W. Löffler. *Full-field quantum correlations of spatially entangled photons*. Physical Review Letters **108**(17) (2012).

[63] J. Leach, R. E. Warburton, D. G. Ireland, F. Izdebski, S. M. Barnett, A. M. Yao, G. S. Buller, and M. J. Padgett. *Quantum correlations in position, momentum, and intermediate bases for a full optical field of view*. Physical Review A **85**(1) (2012).

[64] J. Torres, Y. Deyanova, L. Torner, and G. Molina-Terriza. *Preparation of engineered two-photon entangled states for multidimensional quantum information*. Physical Review A **67**(5) (2003).

[65] G. Molina-Terriza, J. P. Torres, and L. Torner. *Twisted photons*. Nature Physics **3**(5), 305 (2007).

[66] C. I. Osorio, G. Molina-Terriza, and J. P. Torres. *Orbital angular momentum correlations of entangled paired photons*. Journal of Optics A: Pure and Applied Optics **11**(9), 094013 (2009).

[67] A. Mair, A. Vaziri, G. Weihs, and A. Zeilinger. *Entanglement of the orbital angular momentum states of photons*. Nature **412**(6844), 313 (2001).

[68] C. I. Osorio, G. Molina-Terriza, and J. P. Torres. *Correlations in orbital angular momentum of spatially entangled paired photons generated in parametric down-conversion*. Phys. Rev. A **77**(1), 015810 (2008). URL http://link.aps.org/doi/10.1103/PhysRevA.77.015810.

[69] L. Allen, M. W. Beijersbergen, Spreeuw, R. J. C., and J. P. Woerdman. *Orbital angular momentum of light and the transformation of laguerre-gaussian laser modes*. Phys. Rev. A **45**(11), 8185 (1992). URL http://link.aps.org/doi/10.1103/PhysRevA.45.8185.

[70] I. Fernandez-Corbaton, X. Zambrana-Puyalto, and G. Molina-Terriza. *Helicity and angular momentum: A symmetry-based framework for the study of light-matter interactions*. Physical Review A **86**(4) (2012).

[71] L. Marrucci, E. Karimi, S. Slussarenko, B. Piccirillo, E. Santamato, E. Nagali, and F. Sciarrino. *Spin-to-orbital conversion of the angular momentum of light and its classical and quantum applications*. Journal of Optics **13**(6), 064001 (2011). URL http://stacks.iop.org/2040-8986/13/i=6/a=064001.

[72] Hell, Stefan W. l and J. Wichmann. *Breaking the diffraction resolution limit by stimulated emission: stimulated-emission-depletion fluorescence microscopy*. Opt. Lett. **19**(11), 780 (1994).

[73] J. Wang, J.-Y. Yang, I. M. Fazal, N. Ahmed, Y. Yan, H. Huang, Y. Ren, Y. Yue, S. Dolinar, M. Tur, and A. E. Willner. *Terabit free-space data transmission employing orbital angular momentum multiplexing*. Nat Photon **6**(7), 488 (2012). URL http://dx.doi.org/10.1038/nphoton.2012.138.

[74] M. Gecevičius, R. Drevinskas, M. Beresna, and P. G. Kazansky. *Single beam optical vortex tweezers with tunable orbital angular momentum*. Applied Physics Letters **104**(23) (2014). URL http://scitation.aip.org/content/aip/journal/apl/104/23/10.1063/1.4882418.

[75] M. P. J. Lavery, F. C. Speirits, S. M. Barnett, and M. J. Padgett. *Detection of a spinning object using light's orbital angular momentum*. Science **341**(6145), 537 (2013).

[76] N. M. Elias. *Photon orbital angular momentum in astronomy*. A&A **492**(3), 883 (2008). URL http://dx.doi.org/10.1051/0004-6361:200809791.

[77] F. Tamburini, B. Thide, G. Molina-Terriza, and G. Anzolin. *Twisting of light around rotating black holes*. Nat Phys **7**(3), 195 (2011). URL http://dx.doi.org/10.1038/nphys1907.

[78] E. Nagali, L. Sansoni, F. Sciarrino, F. d. Martini, L. Marrucci, B. Piccirillo, E. Karimi, and E. Santamato. *Optimal quantum cloning of orbital angular momentum photon qubits through hong–ou–mandel coalescence*. Nature Photonics **3**(12), 720 (2009).

[79] A. Nicolas, L. Veissier, L. Giner, E. Giacobino, D. Maxein, and J. Laurat. *A quantum memory for orbital angular momentum photonic qubits*. Nat Photon **8**(3), 234 (2014). URL http://dx.doi.org/10.1038/nphoton.2013.355.

[80] J. Leach, M. Padgett, S. Barnett, S. Franke-Arnold, and J. Courtial. *Measuring the orbital angular momentum of a single photon*. Physical Review Letters **88**(25) (2002).

[81] M. Mirhosseini, M. Malik, Z. Shi, and R. W. Boyd. *Efficient separation of the orbital angular momentum eigenstates of light*. Nat Commun **4** (2013). URL http://dx.doi.org/10.1038/ncomms3781.

[82] M. W. Beijersbergen, R. P. Coerwinkel, M. Kristensen, and J. P. Woerdman. *Helical-wavefront laser beams produced with a spiral phaseplate*. Optics Communications **112**(5), 321 (1994).

[83] V. Bazhenov, M. S. Soskin, and M. V. Vasnetsov. *Screw dislocations in light wavefronts*. Journal of Modern Optics **39**(5), 985 (1992). URL http://dx.doi.org/10.1080/09500349214551011.

[84] L. Marrucci, C. Manzo, and D. Paparo. *Optical spin-to-orbital angular momentum conversion in inhomogeneous anisotropic media*. Phys. Rev. Lett. **96**(16), 163905 (2006). URL http://link.aps.org/doi/10.1103/PhysRevLett.96.163905.

[85] E. Nagali, F. Sciarrino, F. d. Martini, L. Marrucci, B. Piccirillo, E. Karimi, and E. Santamato. *Quantum information transfer from spin to orbital angular momentum of photons*. Phys. Rev. Lett. **103**(1), 013601 (2009). URL http://link.aps.org/doi/10.1103/PhysRevLett.103.013601.

[86] E. Karimi, B. Piccirillo, L. Marrucci, and E. Santamato. *Light propagation in a birefringent plate with topological charge*. Opt. Lett. **34**(8), 1225 (2009).

[87] B. Piccirillo, V. D'Ambrosio, S. Slussarenko, L. Marrucci, and E. Santamato. *Photon spin-to-orbital angular momentum conversion via an electrically tunable q-plate*. Applied Physics Letters **97**(24) (2010). URL http://scitation.aip.org/content/aip/journal/apl/97/24/10.1063/1.3527083.

[88] S. Slussarenko, A. Murauski, T. Du, V. Chigrinov, L. Marrucci, and E. Santamato. *Tunable liquid crystal q-plates with arbitrary topological charge*. Opt. Express **19**(5), 4085 (2011).

[89] H. A. Bethe. *Theory of diffraction by small holes*. Phys. Rev. **66**(7-8), 163 (1944). URL http://link.aps.org/doi/10.1103/PhysRev.66.163.

[90] T. W. Ebbesen, H. J. Lezec, H. F. Ghaemi, T. Thio, and P. A. Wolff. *Extraordinary optical transmission through sub-wavelength hole arrays*. Nature **391**(6668), 667 (1998).

[91] C. Genet and T. W. Ebbesen. *Light in tiny holes*. Nature **445**(7123), 39 (2007).

[92] N. Tischler, I. Fernandez-Corbaton, X. Zambrana-Puyalto, A. Minovich, X. Vidal, M. L. Juan, and G. Molina-Terriza. *Experimental control of optical helicity in nanophotonics*. Light: Science & Applications **3**(6), e183 (2014).

[93] B. Richards and E. Wolf. *Electromagnetic diffraction in optical systems. ii. structure of the image field in an aplanatic system*. Proceedings of the Royal Society A: Mathematical, Physical and Engineering Sciences **253**(1274), 358 (1959).

[94] K. Y. Bliokh, E. A. Ostrovskaya, M. A. Alonso, O. G. Rodríguez-Herrera, D. Lara, and C. Dainty. *Spin-to-orbital angular momentum conversion in focusing, scattering, and imaging systems*. Opt. Express **19**(27), 26132 (2011).

[95] X. Zambrana-Puyalto, X. Vidal, I. Fernandez-Corbaton, and G. Molina-Terriza. *Far-field measurements of vortex beams interacting with nanoholes*. Scientific Reports **6**, 22185 EP (2016). URL http://dx.doi.org/10.1038/srep22185.

[96] I. Fernandez-Corbaton, N. Tischler, and G. Molina-Terriza. *Scattering in multilayered structures: Diffraction from a nanohole*. Physical Review A **84**(5) (2011).

[97] H. Di Lorenzo Pires, F. M. G. J. Coppens, and M. P. van Exter. *Type-i spontaneous parametric down-conversion with a strongly focused pump*. Physical Review A **83**(3) (2011).

[98] R. Bennink, Y. Liu, D. D. Earl, and W. Grice. *Spatial distinguishability of photons produced by spontaneous parametric down-conversion with a focused pump*. Physical Review A **74**(2) (2006).

[99] C. I. Osorio, A. Valencia, and J. P. Torres. *Spatiotemporal correlations in entangled photons generated by spontaneous parametric down conversion*. New Journal of Physics **10**(11), 113012 (2008).

[100] P. G. Evans, R. S. Bennink, W. P. Grice, T. S. Humble, and J. Schaake. *Bright source of spectrally uncorrelated polarization-entangled photons with nearly single-mode emission*. Physical Review Letters **105**(25) (2010).

[101] C.-Y. Lu, X.-Q. Zhou, O. Gühne, W.-B. Gao, J. Zhang, Z.-S. Yuan, A. Goebel, T. Yang, and J.-W. Pan. *Experimental entanglement of six photons in graph states*. Nature Physics **3**(2), 91 (2007).

[102] A. Gatti, E. Brambilla, L. Caspani, O. Jedrkiewicz, and L. Lugiato. *X entanglement: The nonfactorable spatiotemporal structure of biphoton correlation*. Physical Review Letters **102**(22) (2009).

[103] E. Brambilla, L. Caspani, L. A. Lugiato, and A. Gatti. *Spatiotemporal structure of biphoton entanglement in type-ii parametric down-conversion*. Phys. Rev. A **82**(1), 013835 (2010). URL http://link.aps.org/doi/10.1103/PhysRevA.82.013835.

[104] A. Gatti, T. Corti, E. Brambilla, and D. B. Horoshko. *Dimensionality of the spatiotemporal entanglement of parametric down-conversion photon pairs*. Physical Review A **86**(5) (2012).

[105] A. Gatti, L. Caspani, T. Corti, E. Brambilla, and O. Jedrkiewicz. *Spatio–temporal entanglement of twin photons: An intuitive picture*. International Journal of Quantum Information **12**(02), 1461016 (2014).

[106] A. Büse, N. Tischler, M. L. Juan, and G. Molina-Terriza. *Where are photons created in parametric down-conversion? on the control of the spatio–temporal properties of biphoton states*. Journal of Optics **17**(6), 065201 (2015). URL http://stacks.iop.org/2040-8986/17/i=6/a=065201.

[107] N. Tischler. *Towards Quantum Metrology for Nanoscatterers*. Ph.D. thesis, Macquarie University (2016).

[108] K. Resch, J. Lundeen, and A. Steinberg. *Experimental observation of nonclassical effects on single-photon detection rates*. Physical Review A **63**(2) (2001).

[109] W. Tittel and G. Weihs. *Photonic entanglement for fundamental tests and quantum communication*. Quantum Information and Computation **1**(2), 3 (2001).

[110] A. V. Sergienko, Y. H. Shih, and M. H. Rubin. *Experimental evaluation of a two-photon wave packet in type-ii parametric downconversion*. Journal of the Optical Society of America B **12**(5), 859 (1995).

[111] Y.-H. Kim and W. P. Grice. *Measurement of the spectral properties of the two-photon state generated via type ii spontaneous parametric downconversion*. Opt. Lett. **30**(8), 908 (2005).

[112] A. Valencia, A. Ceré, X. Shi, G. Molina-Terriza, and J. Torres. *Shaping the waveform of entangled photons*. Physical Review Letters **99**(24) (2007).

[113] A. Pe'er, B. Dayan, A. A. Friesem, and Y. Silberberg. *Temporal shaping of entangled photons*. Phys. Rev. Lett. **94**(7), 073601 (2005). URL http://link.aps.org/doi/10.1103/PhysRevLett.94.073601.

[114] K. A. O'Donnell and A. B. U'Ren. *Time-resolved up-conversion of entangled photon pairs*. Phys. Rev. Lett. **103**(12), 123602 (2009). URL http://link.aps.org/doi/10.1103/PhysRevLett.103.123602.

[115] O. Jedrkiewicz, J.-L. Blanchet, E. Brambilla, P. Di Trapani, and A. Gatti. *Detection of the ultranarrow temporal correlation of twin beams via sum-frequency generation*. Phys. Rev. Lett. **108**(25), 253904 (2012). URL http://link.aps.org/doi/10.1103/PhysRevLett.108.253904.

[116] C. Ren and H. F. Hofmann. *Time-resolved measurement of the quantum states of photons using two-photon interference with short-time reference pulses*. Phys. Rev. A **84**(3), 032108 (2011). URL http://link.aps.org/doi/10.1103/PhysRevA.84.032108.

[117] C. Ren and H. F. Hofmann. *Analysis of the time-energy entanglement of down-converted photon pairs by correlated single-photon interference*. Phys. Rev. A **86**(4), 043823 (2012). URL http://link.aps.org/doi/10.1103/PhysRevA.86.043823.

[118] F. A. Beduini, J. A. Zielinska, V. G. Lucivero, de Icaza Astiz, Yannick A., and M. W. Mitchell. *Interferometric measurement of the biphoton wave function*. Phys. Rev. Lett. **113**(18), 183602 (2014). URL http://link.aps.org/doi/10.1103/PhysRevLett.113.183602.

[119] P. Chen, C. Shu, X. Guo, M. M. T. Loy, and S. Du. *Measuring the biphoton temporal wave function with polarization-dependent and time-resolved two-photon interference*. Phys. Rev. Lett. **114**(1), 010401 (2015). URL http://link.aps.org/doi/10.1103/PhysRevLett.114.010401.

[120] T. Douce, A. Eckstein, Walborn, S. P., Khoury, A. Z., S. Ducci, A. Keller, T. Coudreau, and P. Milman. *Direct measurement of the biphoton wigner function through two-photon interference*. Sci. Rep. **3** (2013). URL http://dx.doi.org/10.1038/srep03530.

[121] L. Zhao, X. Guo, Y. Sun, Y. Su, M. M. T. Loy, and S. Du. *Shaping the biphoton temporal waveform with spatial light modulation*. Phys. Rev. Lett. **115**(19), 193601 (2015). URL http://link.aps.org/doi/10.1103/PhysRevLett.115.193601.

[122] N. Tischler, A. Büse, L. G. Helt, M. L. Juan, N. Piro, J. Ghosh, M. J. Steel, and G. Molina-Terriza. *Measurement and shaping of biphoton spectral wave functions*. Phys. Rev. Lett. **115**(19), 193602 (2015). URL http://link.aps.org/doi/10.1103/PhysRevLett.115.193602.

[123] B. Jack, J. Leach, H. Ritsch, S. M. Barnett, M. J. Padgett, and S. Franke-Arnold. *Precise quantum tomography of photon pairs with entangled orbital angular momentum*. New Journal of Physics **11**(10), 103024 (2009). URL http://stacks.iop.org/1367-2630/11/i=10/a=103024.

[124] H. Di Lorenzo Pires, Florijn, H. C. B., and M. P. van Exter. *Measurement of the spiral spectrum of entangled two-photon states*. Phys. Rev. Lett. **104**(2), 020505 (2010). URL http://link.aps.org/doi/10.1103/PhysRevLett.104.020505.

[125] J. Brendel, N. Gisin, W. Tittel, and H. Zbinden. *Pulsed energy-time entangled twin-photon source for quantum communication*. Phys. Rev. Lett. **82**(12), 2594 (1999). URL http://link.aps.org/doi/10.1103/PhysRevLett.82.2594.

[126] H. Jayakumar, A. Predojević, T. Kauten, T. Huber, G. S. Solomon, and G. Weihs. *Time-bin entangled photons from a quantum dot*. Nat Commun **5** (2014). URL http://dx.doi.org/10.1038/ncomms5251.

[127] J. F. Dynes, H. Takesue, Z. L. Yuan, A. W. Sharpe, K. Harada, T. Honjo, H. Kamada, O. Tadanaga, Y. Nishida, M. Asobe, and A. J. Shields. *Efficient entanglement distribution over 200 kilometers*. Opt. Express **17**(14), 11440 (2009).

[128] Y.-S. Kim, J.-C. Lee, O. Kwon, and Y.-H. Kim. *Protecting entanglement from decoherence using weak measurement and quantum measurement reversal*. Nat Phys **8**(2), 117 (2012). URL http://dx.doi.org/10.1038/nphys2178.

[129] D. A. Lidar, I. L. Chuang, and K. B. Whaley. *Decoherence-free subspaces for quantum computation*. Phys. Rev. Lett. **81**(12), 2594 (1998). URL http://link.aps.org/doi/10.1103/PhysRevLett.81.2594.

[130] P. G. Kwiat, A. J. Berglund, J. B. Altepeter, and A. G. White. *Experimental verification of decoherence-free subspaces*. Science **290**(5491), 498 (2000).

[131] D. A. Lidar and K. B. Whaley. *Decoherence-free subspaces and subsystems*. In *Irreversible Quantum Dynamics*, pp. 83–120 (Springer, 2003).

[132] L. Viola, E. Knill, and S. Lloyd. *Dynamical decoupling of open quantum systems*. Phys. Rev. Lett. **82**(12), 2417 (1999). URL http://link.aps.org/doi/10.1103/PhysRevLett.82.2417.

[133] G.-Q. Liu, H. C. Po, J. Du, R.-B. Liu, and X.-Y. Pan. *Noise-resilient quantum evolution steered by dynamical decoupling*. Nat Commun **4** (2013). URL http://dx.doi.org/10.1038/ncomms3254.

[134] P. Facchi, D. A. Lidar, and S. Pascazio. *Unification of dynamical decoupling and the quantum zeno effect*. Phys. Rev. A **69**(3), 032314 (2004). URL http://link.aps.org/doi/10.1103/PhysRevA.69.032314.

[135] A. M. Steane. *Error correcting codes in quantum theory*. Phys. Rev. Lett. **77**(5), 793 (1996). URL http://link.aps.org/doi/10.1103/PhysRevLett.77.793.

[136] X.-C. Yao, T.-X. Wang, H.-Z. Chen, W.-B. Gao, A. G. Fowler, R. Raussendorf, Z.-B. Chen, N.-L. Liu, C.-Y. Lu, Y.-J. Deng, Y.-A. Chen, and J.-W. Pan. *Experimental demonstration of topological error correction*. Nature **482**(7386), 489 (2012). URL http://dx.doi.org/10.1038/nature10770.

[137] J. Kelly, R. Barends, Fowler, A. G., A. Megrant, E. Jeffrey, White, T. C., D. Sank, Mutus, J. Y., B. Campbell, Y. Chen, Z. Chen, B. Chiaro, A. Dunsworth, I.-C. Hoi, C. Neill, O/'Malley, P. J. J., C. Quintana, P. Roushan, A. Vainsencher, J. Wenner, Cleland, A. N., and J. M. Martinis. *State preservation by repetitive error detection in a superconducting quantum circuit*. Nature **519**(7541), 66 (2015). URL http://dx.doi.org/10.1038/nature14270.

[138] C. H. Bennett, H. J. Bernstein, S. Popescu, and B. Schumacher. *Concentrating partial entanglement by local operations*. Phys. Rev. A **53**(4), 2046 (1996). URL http://link.aps.org/doi/10.1103/PhysRevA.53.2046.

[139] C. H. Bennett, G. Brassard, S. Popescu, B. Schumacher, J. A. Smolin, and W. K. Wootters. *Purification of noisy entanglement and faithful teleportation via noisy channels*. Phys. Rev. Lett. **76**(5), 722 (1996). URL http://link.aps.org/doi/10.1103/PhysRevLett.76.722.

[140] P. G. Kwiat, S. Barraza-Lopez, A. Stefanov, and N. Gisin. *Experimental entanglement distillation and /'hidden/' non-locality*. Nature **409**(6823), 1014 (2001). URL http://dx.doi.org/10.1038/35059017.

[141] J.-W. Pan, S. Gasparoni, R. Ursin, G. Weihs, and A. Zeilinger. *Experimental entanglement purification of arbitrary unknown states*. Nature **423**(6938), 417 (2003). URL http://dx.doi.org/10.1038/nature01623.

[142] D. E. Chang, A. S. Sorensen, E. A. Demler, and M. D. Lukin. *A single-photon transistor using nanoscale surface plasmons*. Nat Phys **3**(11), 807 (2007). URL http://dx.doi.org/10.1038/nphys708.

[143] G. Di Martino, Y. Sonnefraud, S. Kéna-Cohen, M. Tame, Ş. K. Özdemir, M. S. Kim, and S. A. Maier. *Quantum statistics of surface plasmon polaritons in metallic stripe waveguides*. Nano Lett **12**(5), 2504 (2012). URL http://dx.doi.org/10.1021/nl300671w.

[144] A. V. Akimov, A. Mukherjee, C. L. Yu, D. E. Chang, A. S. Zibrov, P. R. Hemmer, H. Park, and M. D. Lukin. *Generation of single optical plasmons in metallic nanowires coupled to quantum dots*. Nature **450**(7168), 402 (2007).

[145] C. Lee, M. Tame, J. Lim, and J. Lee. *Quantum plasmonics with a metal nanoparticle array*. Physical Review A **85**(6) (2012).

[146] R. Kolesov, B. Grotz, G. Balasubramanian, R. J. Stöhr, A. A. L. Nicolet, P. R. Hemmer, F. Jelezko, and J. Wrachtrup. *Wave–particle duality of single surface plasmon polaritons*. Nature Physics **5**(7), 470 (2009).

[147] R. W. Heeres, L. P. Kouwenhoven, and V. Zwiller. *Quantum interference in plasmonic circuits*. Nat Nano **8**(10), 719 (2013). URL http://dx.doi.org/10.1038/nnano.2013.150.

[148] G. Fujii, T. Segawa, S. Mori, N. Namekata, D. Fukuda, and S. Inoue. *Preservation of photon indistinguishability after transmission through surface-plasmon-polariton waveguide*. Optics Letters **37**(9), 1535 (2012).

[149] E. Altewischer, M. P. van Exter, and J. P. Woerdman. *Plasmon-assisted transmission of entangled photons*. Nature **418**(6895), 304 (2002).

[150] E. Moreno, F. García-Vidal, D. Erni, J. Cirac, and L. Martín-Moreno. *Theory of plasmon-assisted transmission of entangled photons*. Physical Review Letters **92**(23) (2004).

[151] S. M. Barnett, J. Jeffers, A. Gatti, and R. Loudon. *Quantum optics of lossy beam splitters*. Phys. Rev. A **57**(3), 2134 (1998). URL http://link.aps.org/doi/10.1103/PhysRevA.57.2134.

[152] J. B. Altepeter, E. R. Jeffrey, and P. G. Kwiat. *Photonic state tomography*. In P. R. Berman and C. C. Lin, eds., *Advances In Atomic, Molecular, and Optical Physics*, vol. 52 of *Advances In Atomic, Molecular, and Optical Physics*, pp. 105–159 (Academic Press, 2005). URL http://www.sciencedirect.com/science/article/pii/S1049250X05520032.